

**Mechanisms Underlying Myeloperoxidase Inhibition: Evaluating the Efficacy and Safety of  
Anti-inflammatory MPO Inhibitors Designed to Limit the Generation of  
Reactive Oxygen and Nitrogen Species**

by

Jiansheng Huang

A dissertation submitted to the Graduate Faculty of  
Auburn University  
in partial fulfillment of the  
requirements for the Degree of  
Doctor of Philosophy

Auburn, Alabama  
August 1, 2015

Keywords: Myeloperoxidase, Inflammation, Reactive Oxygen Species, Benzoic Acid Hydrazide,  
Bioluminescence

Copyright 2015 by Jiansheng Huang

Approved by

Peter Panizzi, Chair, Assistant Professor of Drug Discovery and Development  
Forrest Smith, Associate Professor of Drug Discovery and Development  
Vishnu Suppiramaniam, Professor of Drug Discovery and Development  
Douglas Goodwin, Associate Professor of Biochemistry

## Abstract

Myeloperoxidase (MPO), a heme-containing peroxidase, plays a critical role in the innate immune response by producing hypochlorous acid. MPO-mediated oxidation is also associated with chronic obstructive pulmonary disease (COPD), rheumatoid arthritis (RA), atherosclerosis, and other inflammation associated diseases. Therefore, identification of potent and selective MPO inhibitors can diminish the excessive formation of MPO-derived oxidants and ameliorate oxidative stress during inflammation.

We applied the fluorogenic peroxidase substrate 10-acetyl-3,7-dihydroxyphenoxazine (ADHP) in steady-state and transient kinetic studies of MPO function. Using initial kinetic parameters for the MPO system, we characterized under the same conditions a number of gold standards for MPO inhibition, namely 4-amino benzoic acid hydrazide (4-ABAH), isoniazid and  $\text{NaN}_3$  before expanding our focus to isomers of 4-ABAH and benzoic acid hydrazide analogs. We determined that in the presence of hydrogen peroxide that 4-ABAH and its isomer 2-ABAH are both slow-tight binding inhibitors of MPO requiring at least two steps, whereas  $\text{NaN}_3$  and isoniazid-based inhibition has a single observable step. We also determined that MPO inhibition by benzoic acid hydrazide and 4-(trifluoromethyl) benzoic acid hydrazide was due to hydrolysis of the ester bond between MPO heavy chain Glu 242 residue and the heme pyrrole A ring, freeing the light chain and heme b fragment from the larger remaining MPO heavy chain. In addition, we probed the structure and function relationship behind this ester bond cleavage using a panel of BAH analogs to gain insight into the constraints

imposed by the MPO active site and channel leading to the buried protoporphyrin IX ring. We showed the evidence that Cy5-hydrazide, a fluorescent analog of BAH, cleaved MPO into the complex of LC with heme and the MPO HC, and the HC was labeled with Cy5-hydrazide. This new mechanism would essentially indicate that the benzoic acid hydrazide analogs impart inhibition through initial ejection of the heme catalytic moiety without prior loss of the active site iron.

We found an oral Janus kinase (JAK) inhibitor tofacitinib reversibly inhibited MPO peroxidase activity and was docked into the active site moiety of MPO. A stopped-flow rapid kinetic study and an MPO fluorescence endpoint assay were used to determine the  $K_i$  and  $K_d$  of tofacitinib on MPO inhibition, respectively. Analysis of tofacitinib/BAH-treated MPO by SDS-PAGE and in-gel luminescence imaging revealed that tofacitinib prevented the cleavage of MPO by BAH in the presence of  $H_2O_2$ , which indicates that it may compete for the active site of MPO with BAH. In addition, we also found that tofacitinib could prevent the Soret peak blue shift of MPO heme signature caused by BAH using spectral analysis of MPO with tofacitinib/BAH. These results collectively demonstrate that tofacitinib is a reversible inhibitor of MPO, which further provides new avenues for future drug development efforts that aim to diminish the formation of peroxidase-derived oxidants in chronic inflammatory diseases.

## Acknowledgments

First and foremost, I am deeply grateful to my mentor Dr. Peter Panizzi for his endless help in my graduate study and continual support of my academic career. I really appreciate that it is Dr. Panizzi that brought me into the research field of enzyme kinetics and *in vivo* imaging. Without his strong support, and constant encouragements, we cannot make such a progress on MPO project and this dissertation would not be done. I also express my sincere appreciation to all my committee members, Drs. Forrest Smith, Vishnu Suppiramaniam, Douglas Goodwin for sharing their wisdom and experience and devoting their valuable time to mentoring my graduate study. I also would like to thank my university reader, Dr. Jennifer Panizzi, for her precious suggestions and careful review of my dissertation.

My sincere thanks go to my lab colleagues and alumni, Richard Davis, Andrew Brannen, Heather Eggleston, and Amber Milton for their valuable contributions, inspiring discussions, and helpful support. They helped me a lot when I was working on my preliminary examination. They shared useful advice and precious experience on writing the proposal and making the oral presentation. They were always there to help me make my presentation better. I would like to thank our lab manager Christopher Smith for his help with the experiments and many other friends for their friendship. I would like to thank other faculty members in the Harrison School of Pharmacy for their valuable teaching and advice.

I also would like to thank the funding provided by the National Heart, Lung, and Blood Institute, R00HL094533 & R01HL114477, and the National Institute of Allergy and Infectious Diseases grant 2R44AI085840-02. My appreciation also goes to the Chinese Scholarship Council (CSC) graduate fellowship and Auburn University Research Initiative Cancer (AURIC) graduate fellowship for providing me with the stipend during my graduate study.

I am whole-heartedly grateful to my parents, and my two older brothers for their endless love and encouragement. Without their unconditional support, I would not finish my graduate study and dissertation in the United States. I owe my deepest gratitude to my wife, Hui Huang, for her unconditional love and support. My family is always there to support me.

## Table of Contents

Abstract.....	ii
Acknowledgments .....	iv
List of Tables .....	x
List of Figures.....	xi
List of Abbreviations .....	xiii
Chapter 1 Literature review .....	1
1.1 Introduction .....	1
1.2 Physiological importance of MPO function .....	2
1.3 MPO complexes with substrates or inhibitors.....	3
1.4 Detection of MPO-derived ROS/RNS in isolated cells and <i>in vitro</i> assays .....	5
1.5 Strategies for imaging MPO activity and neutrophil migration <i>in vivo</i> in zebrafish.....	8
1.6 Strategies for imaging MPO activity in pre-clinically imaging in mice .....	10
1.7 Future direction for monitoring MPO activity and PMN recruitment non-invasively.....	14
1.8 Concluding remarks.....	16
Chapter 2 Ordered cleavage of myeloperoxidase ester bonds releases active site heme leading to inactivation of myeloperoxidase by benzoic acid hydrazide analogs.....	23
2.1 Introduction .....	23
2.2 Materials and methods.....	27
2.2.1 Materials .....	27
2.2.2 Steady state analysis of MPO activity kinetics.....	27

2.2.3 Transient state analysis by stopped flow kinetics.....	28
2.2.4 Fluorescence data analysis.....	29
2.2.5 Simultaneous fits of progress curves to determine the specificity constant of MPO-H <sub>2</sub> O <sub>2</sub> system for ADHP .....	29
2.2.6 Global analysis of the MPO inhibition.....	30
2.2.7 SDS-PAGE analysis .....	31
2.2.8 MALDI-TOF method .....	31
2.2.9 Liquid chromatography with tandem mass spectroscopy method.....	32
2.3 Results .....	33
2.3.1 Effect of H <sub>2</sub> O <sub>2</sub> on oxidation of ADHP by MPO .....	33
2.3.2 Michaelis-Menten analysis of the ADHP substrate by MPO-H <sub>2</sub> O <sub>2</sub> system .....	34
2.3.3 Characterization of ADHP conversion to resorufin by the MPO-H <sub>2</sub> O <sub>2</sub> system .....	35
2.3.4 Lineweaver-Burk analysis of 4-ABAH and NaN <sub>3</sub> -based inhibition of the MPO-H <sub>2</sub> O <sub>2</sub> system.....	36
2.3.5 Global analysis of 4-ABAH on oxidation of the ADHP substrate by the MPO-H <sub>2</sub> O <sub>2</sub> system by use of DynaFit modeling software .....	37
2.3.6 Effect of 4-ABAH on oxidation of the ADHP substrate by MPO-H <sub>2</sub> O <sub>2</sub> system.....	37
2.3.7 Comparison of hydrazide analogs and their effect on oxidation of ADHP by the MPO-H <sub>2</sub> O <sub>2</sub> system.....	38
2.3.8 Benzoic acid hydrazide and analog mediated cleavage of MPO.....	39
2.3.9 Analysis of hydrazide induced cleavage product by mass spectroscopy .....	39
2.3.10 Analysis of the spectral changes that occur during MPO based hydrazide inhibition.....	41
2.4 Discussion.....	41
Chapter 3 Inactivation of myeloperoxidase by benzoic acid hydrazide.....	61
3.1 Introduction .....	61

3.2 Materials and methods.....	64
3.2.1 Materials .....	64
3.2.2 SDS-PAGE analysis of (heme b)-LC generation .....	65
3.2.3 MPO fluorescence assay.....	65
3.2.4 MPO activity kinetics .....	66
3.2.5 Mass spectrometric analysis .....	66
3.3 Results .....	67
3.3.1 MPO cleavage by H <sub>2</sub> O <sub>2</sub> /BAH versus H <sub>2</sub> O <sub>2</sub> alone .....	67
3.3.2 Screening of BAH analogs for generation of the (heme b)-LC reaction product.....	68
3.3.3 The cleavage of MPO by BAH analogs is mediated by formation of Compound I .....	69
3.3.4 Inactivation of MPO by Cy5-hydrazide .....	70
3.3.5 Cleavage of MPO by Cy5-hydrazide.....	70
3.3.6 Time-dependent Labeling MPO by Cy5-hydrazide .....	71
3.3.7 Mass spectrometric analysis .....	72
3.3.8 The specificity of BAH cleavage for MPO .....	73
3.4 Discussion.....	74
Chapter 4 Inhibition of myeloperoxidase by rheumatoid arthritis drug tofacitinib.....	94
4.1 Introduction .....	94
4.2 Material and Methods.....	96
4.2.1 Materials .....	96
4.2.2 MPO fluorescence activity assay.....	97
4.2.3 Transient state analysis by stopped flow kinetics.....	97
4.2.4 Global analysis of the effect of tofacitinib on MPO Inhibition.....	98



4.2.5 SDS-PAGE analysis of effects of tofacitinib on MPO cleavage by BAH .....	99
4.2.6 Spectral analysis of MPO .....	99
4.2.7 Inhibition of MPO activity by tofacitinib using luminescence assay .....	100
4.3 Results .....	100
4.3.1 Inhibition of MPO by tofacitinib .....	100
4.3.2 Global analysis of tofacitinib on oxidation of the ADHP by the MPO-H <sub>2</sub> O <sub>2</sub> system by use of DynaFit modeling software .....	101
4.3.3 Rapid kinetic dialysis studies confirm that MPO inhibition by tofacitinib is reversible .....	102
4.3.4 Tofacitinib prevents the destruction of the MPO heme in the presence of high concentration of H <sub>2</sub> O <sub>2</sub> .....	102
4.3.5 Tofacitinib competes with the active site of MPO with BAH.....	103
4.3.6 Spectroscopic analysis of the effect of tofacitinib on the MPO heme signature .....	104
4.3.7 Inhibition of MPO luminescence production by tofacitinib .....	104
4.3.8 Bioluminescence imaging of MPO activity in Matrigel implant <i>in vivo</i> .....	105
4.4 Discussion.....	106
Conclusions .....	121
References .....	125

## List of Tables

Table 1.1 A summary of the sensors for the detection of MPO-derived oxidants and other ROS/RNS. ....	17
Table 2.1 Discrimination analysis of two models for inhibition of MPO activity by the given compounds using DynaFit 3. ....	47
Table 2.2 Inhibitory efficiencies of hydrazide analogs on MPO activity.....	48
Table 3.1 Mass spectrometry analysis of tryptic MPO peptides indicated three peptides had an increased mass corresponding to the formation of the benzoic acid adducts. ....	80
Table 3.2 Mass spectrometry analysis of tryptic MPO peptides indicated eight residues had an increased mass corresponding to oxidization of methionine (Met) residues. ....	81
Table 4.1 Inhibitory efficiencies of tofacitinib on MPO activity. ....	109
Table 4.2 Effect of pH on the $K_d$ value of tofacitinib for the MPO fluorescence reaction.....	110

## List of Figures

Figure 1.1 Biology of PMNs in response to injury and inflammation. ....	19
Figure 1.2 Fluorescence reactions for measuring MPO activity. ....	20
Figure 1.3 <i>In vivo</i> monitoring PMN recruitment in zebrafish and MPO activity in mice. ....	21
Figure 2.1 Characterization of the ADHP oxidation by MPO-H <sub>2</sub> O <sub>2</sub> complex. ....	50
Figure 2.2 NaN <sub>3</sub> inhibition of Compound I. ....	52
Figure 2.3 Comparison of Compound I inhibition by NaN <sub>3</sub> and 4-ABAH using simultaneous reaction modeling. ....	53
Figure 2.4 Reversibility of 4-ABAH-mediated MPO inhibition. ....	54
Figure 2.5 Linear free-energy relationship of substituted benzoic acid hydrazide compounds tested on inactivation of Compound I. ....	56
Figure 2.6 Benzoic acid hydrazide-mediated cleavage of MPO active site heme. ....	57
Figure 2.7 Sequential hydrolysis of ester bonds results in cleavage of the catalytic heme from MPO active site. ....	58
Figure 3.1 Effect of BAH on MPO compared to the heme destruction generated by high dose H <sub>2</sub> O <sub>2</sub> treatment. ....	82
Figure 3.2 Screening of BAH analogs for production of (heme b)-LC cleavage product. ....	83
Figure 3.3 Cleavage of MPO by BAH is dependent on H <sub>2</sub> O <sub>2</sub> . ....	85
Figure 3.4 Inactivation of MPO by Cy5-hydrazide. ....	86
Figure 3.5 Tracking Cy5 modification following cleavage of the (heme b)-LC from HC of MPO. ....	87
Figure 3.6 Identification of modified sites on myeloperoxidase after incubation with BAH and H <sub>2</sub> O <sub>2</sub> . ....	89
Figure 3.7 BAH mediated release of heme b is specific to MPO. ....	90
Figure 4.1 Inhibition of MPO by tofacitinib. ....	111

Figure 4.2 Kinetic study of MPO inhibition by tofacitinib. ....	112
Figure 4.3 Effect of tofacitinib on MPO compared to the heme destruction generated by high dose H <sub>2</sub> O <sub>2</sub> treatment. ....	113
Figure 4.4 Tofacitinib prevents the cleavage of MPO by BAH in the presence of H <sub>2</sub> O <sub>2</sub> . ....	114
Figure 4.5 The interference of tofacitinib on MPO cleavage by BAH using spectroscopic analysis of MPO heme signature. ....	115
Figure 4.6 Inhibition of MPO by tofacitinib using luminescence assay. ....	116
Figure 4.7 Luminol-BLI of MPO implants <i>in vivo</i> . ....	117

## List of Abbreviations

2-ABAH	2- aminobenzoic acid hydrazide
4-ABAH	4- aminobenzoic acid hydrazide
ABPP	Activity-based profiling probe
ADHP	10-acetyl-3, 7-dihydroxyphenoxazine
APF	2-[6-(4'-amino)phenoxy-3H-xanthen-3-on-9-yl]benzoic acid
BAH	Benzoic acid hydrazide
BLI	Bioluminescence imaging
BSA	Bovine serum albumin
CMH	1-hydroxy-3-methoxycarbonyl-2,2,5,5-tetramethylpyrrolidine
COPD	Chronic obstructive pulmonary disease
CPH	1-hydroxy-3-carboxy-2,2,5,-tetramethyl-pyrrolidine hydrochloride
CRET	Chemiluminescence resonance energy transfer
DAF-FM	4-amino-5-methylamino- 2',7'-difluorescein
DBNBS	3,5-dibromo-4-nitrosobenzenesulfonic acid
DCHF	2',7'-dichlorofluorescein
DEPMPO	5-(diethoxyphosphoryl)-5-methyl-1-pyrroline N-oxide
DHE	Dihydroethidium
DHR123	Dihydrorhodamine 123
3-DMABAH	3-(dimethylamino) benzoic acid hydrazide

DMPO	5,5-dimethyl-1-pyrroline <i>N</i> -oxide
DMSO	Dimethyl sulphoxide
DTPA	Diethylenetriaminepentaacetic acid
Duox	Dual oxidase
EPO	Eosinophil peroxidase
EPR/ESR	Electron paramagnetic or spin resonance
ESI	Electrospray ionization
4-FBAH	4-fluorobenzoic acid hydrazide
FRET	Fluorescence resonance energy transfer
Gd	Gadolinium
GFP	Green fluorescence protein
GSH	Glutathione
HC	Heavy chain of myeloperoxidase
H <sub>2</sub> DCFDA	2', 7'-dichlorodihydrofluorescein diacetate
HE	Hydroethidine
HOCl	Hypochlorous acid
H <sub>2</sub> O <sub>2</sub>	Hydrogen peroxide
HPF	2-[6-(4'-hydroxy)phenoxy-3H-xanthen-3-on-9-yl]benzoic acid
HRP	Horseradish peroxidase
5-HT	5-hydroxytryptamine
IL	Interleukins
JAK	Janus kinase
katG	Bacterial catalase-peroxidase

LC	Light chain of myeloperoxidase
LC-MS	Liquid chromatography-mass spectrometry
LPO	Lactoperoxidase
LPS	Lipopolysaccharide
MALDI-MS	Matrix-assisted laser desorption ionization-mass spectrometry
mito-TEMPO-H	1-hydroxy-4-[2-triphenylphosphonio)-acetamido]-2,2,6,6-tetramethylpiperidine
MPO	Myeloperoxidase
MRI	Magnetic resonance imaging
MI	Myocardial infarction
4-NBAH	4-nitrobenzoic acid hydrazide
NETs	Neutrophil extracellular traps
NIR	Near infrared
NO•	Nitric oxide radical
NOX	NADPH oxidases
•OH	Hydroxyl radical
O <sub>2</sub> <sup>-</sup>	Superoxide radical
<sup>1</sup> O <sub>2</sub>	Singlet oxygen
<sup>-</sup> OCl	Hypochlorite
ONOO <sup>-</sup>	Peroxynitrite
PMN	Polymorphonuclear neutrophils
ROS/RNS	Reactive oxygen and nitrogen species
RA	Rheumatoid arthritis

Resorufin	7-hydroxyl-3H-phenoxazin-3-one
SNAPF	Sulfonaphthoaminophenyl fluorescein
SOD	Superoxide dismutase
SPNs	Semiconducting polymer nanoparticles
STAT	Signal transducer and activator of transcription
4-TFMBAH	4-(trifluoromethyl) benzoic acid hydrazide
2-TX	2-thioxanthine
TNF	Tumor necrosis factor
TPO	Thyroid peroxidase
YFP	Yellow fluorescence protein



## Chapter 1 Literature review

### 1.1 Introduction

Myeloperoxidase (MPO) within myeloid cells aids in the clearance of microbes by generation of peroxidase-mediated oxidants that kill engulfed pathogens trapped inside neutrophils and monocytes. Herein, we exam state-of-the-art regarding molecular imaging strategies for the (i) *in vitro* evaluation of MPO function, (ii) *in vivo* neutrophil chemotaxis and (iii) monitoring inflammation in mouse models. To date, there are a number of optical probes that target MPO reaction products for use in either cell-based conditions or triggered neutrophil migration as a function of inflammatory burst response after injury in zebrafish and mouse model systems. Presented here we review the following: (i) the broad impact of MPO on normal physiology, (ii) the difference between MPO and other peroxidase, (iii) the current optical probes for use as surrogates for direct measures of MPO-derived oxidants, (iv) the utility of a zebrafish tail-wound model for tracking neutrophil migration under the mpx promoter, and (v) the range of pre-clinical options, including optical, for imaging MPO accumulation in mice. We also will stress the advantages and the drawbacks of each host system, pharmacokinetic considerations prompting their cell culture or *in vivo* utility as indicators of MPO function. Taken together, our review should shed light on the fundamental rationals behind these techniques for assessing MPO activity and neutrophil response after injury

for the purpose of developing safe MPO inhibitors, as a potential therapy for chronic obstructive pulmonary disease (COPD) and / or rheumatoid arthritis (RA).

## **1.2 Physiological importance of MPO function**

Myeloperoxidase (MPO), a heme-containing peroxidase in myeloid cells (polymorphonuclear neutrophils (PMN) and monocytes), plays a central role in the development of the nascent inflammatory response and the perpetuation of chronic inflammation in diseases such as RA. From the initial trigger (i.e., damage and/ or infection), patrolling monocytes [1], mast cells [2] and dendritic cells [3] presumably respond to the injury almost immediately by increasing vascular permeability through histamine release and simultaneous establishment of gradient chemokines and chemo-attractants required to arrest circulating leukocytes (see Figure 1.1). A hallmark PMN burst occurs when responding (i.e., soon to be arrested) leukocytes crawl to a slow roll through interaction of leukocyte derived E-selectin with P-selectin [4]. PMN and other leukocytes essentially stop as the burden of the drag exerted on the cell overcomes blood flow pressures through, in part, binding of CD11b (in mice) with newly exposed intercellular adhesion molecule 1 on the activated endothelial cell surface (<sup>EC</sup>ICAM-1). This progress occurs near the damage and just prior to diapedesis [5]. Once at the inflammatory site, PMN and later PMN-signaled monocytes will begin to phagocytose foreign material (i.e., microbes) or damaged host cellular matter [4]. To combat pathogens in the area, PMN ensnare microbes through exocytosis of chromosomal material called neutrophil extracellular traps (NETs) enabling phagocytosis by other responding PMN in the localized microenvironment [6, 7]. Thirty percent of the total cellular MPO was released from neutrophils at the infection sites. The majority of

released MPO is able to bind with NETs and the enzymatic activity of MPO on NETs is responsible for antimicrobial activity and tissue injury after neutrophils release NETs [8]. Engulfed pathogens face harsh pH changes in acid vacuoles, degradation of cell wall components by PMN elaborated proteases (i.e., cathepsin G and elastase), and oxidation of DNA and proteins by the powerful oxidant hypochlorous acid (HOCl) generated by the prolific MPO-H<sub>2</sub>O<sub>2</sub> system [9]. In the context of pathobiology of human inflammatory diseases, MPO has been recognized as a biomarker for a heightened immune state due to the generation of these various oxidized DNA and protein adducts [10]. For example, reactive oxygen and nitrogen species (ROS/RNS) production during oxidative stress has been linked to MPO expression and activity in chronic obstructive pulmonary disease (COPD) [11], RA [12], atherosclerosis [13-15], and even cancer [16, 17]. In this review, we discussed the recent emerging studies on *in vivo* imaging using MPO as a target to monitor disease progression, tracking neutrophil migration, and detection methods for imaging inflammation in (pre)clinical applications.

### **1.3 MPO complexes with substrates or inhibitors**

As a general rule, all peroxidases have an active site heme group that contains a central iron atom that maintains its oxidation state (i.e., reactivity) through coordination with a distal histidine (His) residue. This important His coordination occurs from underneath the heme prosthetic group allowing for the entire proximal heme surface to be available to carry out heme-dependent peroxidase activity resulting in HOCl formation. There has been a number of important MPO structures solved that demonstrate complex formation between the MPO enzyme with a variety of ligands and/ or inhibitors that have indicated a relatively large space available for the substrates to bind in this solvent

exposed proximal surface cavern wherein the heme acts as the floor, the presence of a number of water molecules in this cavern that provide additional hydrogen bonding between the active site and MPO's various substrates, and a more narrow substrate binding and / or solvent-exposed chase leading to the active site (MPO isoform C (PDB accession number 1LXP), MPO co-crystalized with cyanide and thiocyanate (1DNW), MPO-cyanide complex (1DNU), MPO from human leukocyte (3F9P), thioxanthine inhibited MPO (3ZS1), ceruloplasmin bound MPO (4EJX) and MPO with HX1 (4C1M) [18-24]. One primary difference between mammalian peroxidases (e.g., MPO, lactoperoxidase (LPO), eosinophil peroxidase (EPO), and thyroid peroxidase (TPO)) from non-mammalian peroxidases (e.g., horseradish peroxidase (HRP), bacterial catalase-peroxidase (katG), lignin peroxidase, and ascorbate peroxidase) is the presence of specific linkages between the respective heme prosthetic group and the main peroxidase protein scaffold. In the case of MPO, the protoporphyrin IX macrocycle has three such covalent bonds with the MPO protein, causing the formation of a distant spectral signature [25]. These linkages correspond to the following: (1) an ester bond between aspartate residue of (<sup>LC</sup>Asp<sup>94</sup>) MPO light chain and the methyl side chain of pyrrole C, (2) another ester bond between glutamate on the heavy chain (<sup>HC</sup>Glu<sup>242</sup>) and the methyl side chain of pyrrole A, and (3) a vinyl sulfonium linkage between a heavy chain methionine (<sup>HC</sup>Met<sup>243</sup>) and pyrrole A [25]. Classic biochemical studies [25, 26] have demonstrated the presence of this vinyl sulfonium bond between MPO and the pyrrole A is marked by a distinct Soret (a.k.a. absorbance) band at 430 nm. Met<sup>243</sup> variants of MPO have diminished peroxidase activity compared to native MPO and site-directed disruption of this linkage causes the Soret band at 430 nm to be lost in favor of a 413 nm band that

is reminiscent of the absorbance spectra of LPO [25, 26]. Other Soret bands are responsible for the green coloration of MPO protein, namely bands at 496, 570, 620, and 690 nm [27]. Our recent study found that some potent MPO inhibitors like benzoic acid hydrazide (BAH) and its analogs cause disruption of these important ester linkages [28]. It is thought that in mammalian peroxidase these linkages impart a level of resistance to the powerful oxidants that they produce, namely HOCl and HOBr for MPO and LPO, respectively [29].

#### **1.4 Detection of MPO-derived ROS/RNS in isolated cells and *in vitro* assays**

To study MPO in any complex mixture, there must be effective means to differentiate between MPO-dependent and other ROS/RNS reaction products. As such, a number of sensors have been developed to meet this need for the study of various oxidants such as hydroxyl radical ( $\bullet\text{OH}$ ), singlet oxygen ( $^1\text{O}_2$ ), superoxide radical ( $\text{O}_2^-$ ), peroxynitrite ( $\text{ONOO}^-$ ) and hypochlorite ( $\text{OCl}^-$ ). A summary of these sensors are shown in Table 1.1. This section will focus on introducing most of these sensors, attributing unique properties that drive their utility and impart their relative limitations.

Generally speaking, the cellular redox homeostasis is maintained by a series of checks and balances between the production of ROS/RNS and the anti-oxidant system, wherein superoxide dismutase (SOD) produces  $\text{H}_2\text{O}_2$  from  $\text{O}_2^-$  and this is counteracted by the activity of catalase meant to degrade  $\text{H}_2\text{O}_2$  into  $\text{H}_2\text{O}$ . Other antioxidants act as general scavengers such as NADPH, glutathione, thioredoxin, and peroxiredoxin [30], which further modulates the levels of certain oxidants. Up-regulated NADPH oxidases increase the relative  $\text{O}_2^-$  levels contributing to the certain pathologies, such as cardiac hypertrophy, fibrosis, ischemic stroke, and neurodegenerative diseases [31]. Central to this and most

important to the discussion here is MPO that functions to generate the potent oxidants HOCl from  $\text{Cl}^-$  and  $\text{H}_2\text{O}_2$ , whilst generating other ROS (e.g.,  $\bullet\text{OH}$ ,  $^1\text{O}_2$ , and  $\text{ONOO}^-$ ) [32].

Given the relative importance of the redox state of the catalytic MPO iron, the use of electron paramagnetic or spin resonance (EPR/ESR) spectroscopy has become a sensitive method for assessment of inhibitor / substrate altered redox states [33]. Some probes for this application include 5,5-dimethyl-1-pyrroline *N*-oxide (DMPO) for trapping  $\text{O}_2^-$  [34], 5-(diethoxyphosphoryl)-5-methyl-1-pyrroline *N*-oxide (DEPMPO) for MPO and MPO-derived oxidants [35], 1-hydroxy-3-methoxycarbonyl-2,2,5,5-tetramethylpyrrolidine (CMH) for the spin trapping of  $\text{ONOO}^-$  and  $\text{O}_2^-$  [34], (1-hydroxy-3-carboxy-2,2,5,5-tetramethyl-pyrrolidine hydrochloride) CPH for stable trapping  $\text{O}_2^-$  [33], 1-hydroxy-4-[2-triphenylphosphonio)-acetamido]-2,2,6,6-tetramethylpiperidine (mito-TEMPO-H) for detection of mitochondrial  $\text{O}_2^-$  [36], and 3,5-dibromo-4-nitrosobenzenesulfonic acid (DBNBS) for trapping  $\text{NO}\bullet$ ,  $\text{ONOO}^-$  and  $\text{O}_2^-$  in biological systems [37]. The distinct advantage of the CPH probe is that it generates a more stable  $\text{NO}\bullet$  with a longer half-life for a better detection window, whereas the nitron spin traps DMPO and DEPMPO produce unstable  $\text{O}_2^-$  intermediates in biological samples [33]. Further, CPH probes are membrane permeable and can provide insights into generation of ROS in extracellular or intracellular environments (cytosol and mitochondria) compared to other probes [36].

There are also cell-permeable fluorogenic ROS/RNS sensors such as 2', 7'-dichlorodihydrofluorescein diacetate ( $\text{H}_2\text{DCFDA}$ ) and dihydrorhodamine 123 (DHR123) that are oxidized by  $\text{ROO}\bullet$ ,  $\text{ONOO}^-$  and  $\text{HOCl}$  [38].  $\text{H}_2\text{DCFDA}$  is converted into 2',7'-dichlorofluorescein (DCHF) by intracellular esterases within the cell [39]. Apart from the

relative non-selectivity to ROS species and oxidants, both cytochrome c and heme peroxidases catalyze the oxidation of DCHF and DHR123 [40]. NO• is able to oxidize another fluorescein-based probe 4-amino-5-methylamino-2',7'-difluorescein (DAF-FM) to fluorescent dye benzotriazole via oxidative cycloaddition reactions [41, 42]. Hydroethidine (HE)-based probe mito-SOX can detect O<sub>2</sub><sup>-</sup> in the mitochondria, whereas dihydroethidium (DHE) can detect O<sub>2</sub><sup>-</sup> general within cells [43]. These probes are not directly used for the detection of MPO-derived products but can be used to confirm the oxidant generated or present in a complex mixture.

Other ROS cell-permeable fluorogenic probes include 2-[6-(4'-amino)phenoxy-3H-xanthen-3-on-9-yl]benzoic acid (APF) and 2-[6-(4'-hydroxy)phenoxy-3H-xanthen-3-on-9-yl]benzoic acid (HPF) that undergo *o*-dearylation oxidation to form highly fluorescence products in the presence of •OH, ONOO<sup>-</sup> and <sup>-</sup>OCl [42, 44]. HPF can selectively detect the presence of •OH and ONOO<sup>-</sup>, whereas APF can be oxidized by •OH, ONOO<sup>-</sup>, and hypochlorite (<sup>-</sup>OCl) but not other ROS. MPO derived HOCl and EPO derived HOBr were specifically detected in neutrophils and eosinophil by the combination of APF and HPF, respectively [44, 45]. Other oxidation mediated probes include HKGreen-3 which detects ONOO<sup>-</sup> *in vitro* or in RAW 264.7 macrophages generating fluorescent *N*-methylrhodol by an *N*-dearylation reaction [46]. Similarly, a BODIPY-based fluorescent probe HKOCl-1 which detects HOCl due to the formation of benzoquinone from *p*-methoxyphenol [46, 47]. A red shifted fluorogenic sensor of peroxidase activity is 10-acetyl-3,7-dihydroxyphenoxazine (ADHP also known as Amplex Red), which has a strict H<sub>2</sub>O<sub>2</sub> dependency allowing H<sub>2</sub>O<sub>2</sub> to be used as a trigger for inhibitor studies, whereby the enzyme and compound can be allowed to reach

equilibrium prior to initiation of the chemical reaction (Figure 1.2). Previously, we used stopped flow spectroscopy and the ADHP substrate to study MPO inhibition by BAH and its analogs [28, 48]. ADHP also has been utilized for tissue-based assays for the presence of MPO activity as a surrogate for assessing inflammation [49]. There is evidence that ADHP can undergo auto-radical formation under prolonged exposure to excitation energy [44].

### **1.5 Strategies for imaging MPO activity and neutrophil migration *in vivo* in zebrafish**

Although *in vitro* assessment is complex given the various potential ROS/RNS produced, the use of the combination of newly engineered reporters and animal models has allowed for specific tracking of myeloid cells and monitoring of MPO activity *in vivo* often in real-time. To better understand the mechanisms underpinning neutrophils recruitment processes such as those central to Figure 1.1, some labs have begun to use transgenic zebrafish as a tool for testing toxicity, effects on developmental staging, and inhibition of cell migration [50-53]. The advantage of using zebrafish is that the embryo develops rapidly and reaching statistical power is relatively inexpensive. Importantly, the zebrafish neutrophils have multi-lobed nuclei and a heterophilic cytoplasm filled with both azurophilic and non-azurophilic granules reminiscent of its human counterpart [54]. The myeloid-specific peroxidase is stored in the azurophilic granules of zebrafish neutrophil [54]. Activity-based staining for peroxidase activity has been done in the cytoplasm of neutrophils from a fresh smear of zebrafish blood using benzidine dihydrochloride in the presence of H<sub>2</sub>O<sub>2</sub> to produce a diaminobenzidine brown-black precipitate that stains the MPO activity [54, 55]. Recently a transgenic zebrafish was



created with GFP under a neutrophil-specific MPO promoter [50]. Transection of the zebrafish tail induces injury and inflammation [50]. Visualization of neutrophil-mediated inflammation demonstrated retrograde chemotaxis as a novel mechanism to regulate the resolution phase in response to inflammation using *in vivo* time-lapse imaging [56]. To further prove the utility, this model was repeated by using these fish and injury created by mechanical generation of the wound before and 6 hours post tail-wounding shown in Figure 1.3A. Results indicate that there are an abundance of neutrophils at the wound in 3 days post fertilization (dpf) *mpo:GFP* embryo (Figure 1.3A). GFP-expressing neutrophils and mCherry-expressing macrophage in transgenic zebrafish allow exploring the distinct differences in the recruitment of neutrophils and macrophages using intravital imaging [57, 58]. Combined the neutrophil-tracking Tg (*mpo:GFP*) fish with Tg (*TCFsiam:mCherry*) Wnt reporter fish, Wnt- $\beta$ -catenin was identified as a signaling pathway to modulate the recruitment and resolution of inflammatory cell and injury microenvironment following amputation of the tail fin [58]. Tracking neutrophil migration was also performed using rhodamine-labeled *S. aureus* in the same model, whereby confocal images demonstrated the recruitment and phagocytosis role of neutrophils in host defense for the fish [59]. This transgenic zebrafish model also can be used to perform the high-throughput screening for identification of compounds that change recruitment of neutrophils or promote inflammation resolution [59, 60]. An inflammation model established in the transgenic zebrafish (*mpo:GFP*) induced by lipopolysaccharide (LPS) can be used to screen anti-inflammatory drugs [61].

To investigate this mechanism, HyPer was developed for a highly specific detection method of H<sub>2</sub>O<sub>2</sub> in zebrafish [51]. It is composed of a circularly permuted

yellow fluorescence protein (YFP) engineered in the bacterial H<sub>2</sub>O<sub>2</sub>-sensitive transcription factor OxyR. In the presence of H<sub>2</sub>O<sub>2</sub>, there is increased emission excited at 500 nm and decreased emission excited at 420 nm caused by conformational changes of YFP due to the oxidation of OxyR. Neutrophil recruitment to the wound was measured by imaging leukocyte-specific fluorescent tags (*mpo*:GFP and *lysC*:DsRED210) [51]. It was found that there was a sustained increase in H<sub>2</sub>O<sub>2</sub> concentration at the wound margin, leading to the increased recruitment of neutrophils at the wound [51]. Dual oxidase (Duox) activity in epithelial cells was required to form a tissue-scale gradient of H<sub>2</sub>O<sub>2</sub> induced by wounding in transgenic zebrafish model, which further led to the recruitment of leukocytes to the wound [51]. The transgenic zebrafish model with H<sub>2</sub>O<sub>2</sub> sensor and neutrophil trackers allows for the identification of the role of a tissue gradient of H<sub>2</sub>O<sub>2</sub> in the recruitment of neutrophils and understanding the reverse migration as a regulatory mechanism of inflammation resolution.

### **1.6 Strategies for imaging MPO activity in pre-clinical imaging in mice**

Bio-distribution studies indicate that there are static spatial and temporal differences in expression of mammalian peroxidases in host cells and tissues. Mobile immune cells are also an excellent source of stored peroxidases as these enzymes are sequestered in granules, as is the case of MPO and EPO [62]. In response to stimuli, MPO can be released from PMNs and flood the injured tissue with MPO to catalyze the production of the disinfectant HOCl. As such, both plasma and synovial fluid taken from RA patients has significantly higher MPO levels compared to healthy controls [12]. In addition, MPO deficiency attenuated the RA severity in mouse models without affecting circulating cytokine levels [63], indicating that MPO is a critical mediator of joint

inflammation and damage in experimental RA.

Since quantification of MPO levels can ultimately indicate the levels of inflammatory burden, the development of ROS/RNS directed imaging agents has been sought to strengthen the accuracy of disease diagnosis and assessment of therapeutic outcomes. Success of these probes is highly dependent on the application window, which is driven by the pharmacokinetic properties of the agent *in vivo*. Enhanced washout kinetics can lead to reduced circulation half-life and thereby limit agent distribution and impact accumulate at sites of inflammation. For example, solid tumor and regions of inflammation are known to be hyper-permeable to micro- and nano-particulates via enhanced permeability and retention properties [64]. Currently, there are already several *in vivo* imaging methods available, such as magnetic resonance imaging of MPO-induced oligomerization of chelated gadolinium containing serotonin analogs [65], fluorescence imaging of MPO-induced release of oxazine probes from a nanoparticle scaffold [66], and MPO-induced chemiluminescence using luminol [67, 68]. Previously, it was reported that bioluminescence imaging of MPO activity was successfully conducted in spontaneous large granular lymphocytic tumors in Gzmb: Tbx1 mice with intraperitoneal administration of luminol [67]. On the surface, these results are not surprising as these tumors are massively infiltrated with neutrophils. But the ability to perform a ‘pseudo’ western using chemiluminescence *in vivo* was very novel. The limitation of this approach is luminescent signal emitted from oxidation of luminol by MPO-derived oxidants can only be efficiently detected from superficial sites. This is partly, because photon scattered and absorbed as the light moves through blood and tissue [69]. This methodology is employed in Figure 1.3B, where we used an intraperitoneal injection of luminol to detect

MPO activity in inflammation sites associated with an acute cutaneous infection (Figure 1.3). This methodology has some limitation in that luminal has an extremely short half-life (20 min) in mice [67] and is cleared 90 % by the kidney and excreted through urine [70]. Another limitation is that this imaging method can only be used as a pan-inflammation type sensor as it does not discriminate between sterile inflammation and an active infection [71].

To overcome this limitation, hybrid techniques were developed that combined near-infrared nanoparticles quantum dots with luminal-based detection methods. The resulting agents use the luminol light to excite the 800 nm-emitting quantum dots [68]. As proof of principal of this technology, indicate MPO presence in both sterile inflammation triggered by LPS injection and in metastatic tumor model in athymic (nu/nu) mice [68].

Compared to luminescence imaging technology, fluorescence imaging allows us to detect the target protein in milliseconds although there is auto-fluorescence from tissue and hemoglobin when using fluorescence imaging technologies. Also it is not required to inject the substrate luciferin before imaging. To evaluate the relationship between MPO-derived oxidants and certain disease models, APF derived near-infrared dye sulfonaphthoaminophenyl fluorescein (SNAPF) was synthesized to detect MPO-derived HOCl from human whole blood and atherosclerotic plaque using fluorescence microscopy [72]. Due to the longer emission wavelengths SNAPF was also tested in a matrigel model to detect MPO activity *in vivo*. An activatable near-infrared (NIR) probe oxazine-coated nanoparticle was also synthesized to fluorescently image MPO activity in mouse hearts after myocardial infarction (MI) [66]. Based on 1-Ethyl-3-(3-

dimethylaminopropyl)carbodiimide (EDC) reaction, the carboxyl group of quenched oxazine intermediate can be attached to the amine group of Alex488 on nanoparticles. Once it is oxidized by MPO derived HOCl and peroxynitrite, this oxazine-based activatable probe can be activated and emit near-infrared light, and the half-life of this probe is about 9 hrs in mice [66]. This activatable probe acts as a novel prognostic indicator for MI using fluorescence reflectance imaging. Another quenched nanoparticle LS601R-PEG40, a non-fluorescent hydrocyanine probe conjugated with PEG40, can be oxidized to fluorescent LS601 in the presence of ROS [73]. This quenched probe acts as a novel diagnostic agent for the *in vivo* detection of injury-induced low level ROS production in a mouse model of hindlimb ischemia with high sensitivity and contrast [73]. In optical imaging, photo-acoustic imaging is a more promising and applicable imaging modality for the non-invasive imaging of physiology and pathology at the molecular level with higher spatial resolution and deep tissue penetration, which is unattainable by fluorescence imaging. A near-infrared light absorbing semiconducting polymer nanoparticles (SPNs) act as photo-acoustic molecular imaging probes for *in vivo* real-time imaging of ROS in living mice [74]. IR775S, a cyanine dye derivatives sensitive to ROS-mediated oxidation, was conjugated with SPN1 to synthesize a ratiometric photo-acoustic probe (RSPN, ratio of photo-acoustic amplitudes at 700nm/820nm) for the detection of ROS involved in the pathologies ranging from neurodegenerative and cardiovascular diseases to cancer [74]. This SPNs probe provide the stable nanoplatform to allow photons to be used to produce ultrasound waves in the presence of ONOO<sup>-</sup> and HOCl due to the ROS-mediated rapid oxidative decomposition of IR775S [74], which prolongs the circulation time and enhances the capability of photo-acoustic molecular

imaging of oxidative stress during inflammation in a mouse model of acute local hind limb edema non-invasively.

Magnetic resonance (MR) imaging is an accepted method of more applicable *in vivo* imaging approach in clinical settings. It allows us to capture non-invasive anatomical information, which is correlated to the function of 5-hydroxytryptamide (5-HT) conjugated to Gadolinium (Gd)-based, namely Gd-bis-5-HT-DTPA where a paramagnetic effect is produced upon production of the polymer [65, 75]. The enhanced MR signal can be prolonged up to 120 mins with MPO-Gd probe in matrigel experiment, mice brain, and in the infarct zone in mice [72, 76, 77]. With regard to cytotoxicity, the mono-5HT-DTPA-Gd has no substantial toxicity effect up to 5 mM, although there is significant toxic effect at 0.3 mM for the analogous to the levels seen in o-dianisidine coupled to DTPA-Gd agent. The toxic effect of bis-5HT-DTPA-Gd on the viability of the activated macrophages has no differences with the non-activated cells targeting radical generation using the DCFH-DA dye [76]. To satisfy the requirement of clinical translation of MPO activity *in vivo* visualization, a MR imaging protocol of MPO activity was optimized in a rabbit model of the inflamed intracranial aneurysm using MPO-specific Gd-containing contrast agent [78]. The translational role of this probe can be applied to diagnose the active demyelinating plaques for specific inflammatory plaque imaging as well as to non-invasively monitor the disease treatment.

### **1.7 Future direction for monitoring MPO activity and PMN recruitment non-invasively**

Coupled probe labeled inhibitors are not a new concept and have been used to study apoptosis, coagulation, fibrinolysis, cancers and other processes. Activity-based

protein profiling (ABPP) is a proteomic method for assignment the functions to the uncharacterized enzymes in proteomics. Several ABPP probes were designed for a couple of enzymes, such as serine hydrolases [79], cysteine hydrolases [80], metalloproteases [81], kinases [82], histone deacetylases [83, 84], oxidoreductases [85]. This so-called ABPP identifies biomarkers for central enzymes and uses proteomics methods to identify interacting proteins and complex that either block or active the formation of the complexes as evident by disappearance or appearance of their fluorescence bands [86]. One of the intriguing example on identification of biomarkers and inhibitors of these proteins for diseases using ABPPs is the use of fluorophosphonates in serine hydrolases [87]. Recent studies profiled serine hydrolase activities using fluorescent fluorophosphonates in several human melanoma and breast carcinoma cell lines [88]. A gel-based profile coupled with LC-MS analysis and avidin chromatography combined with biotinylated fluorophosphonates probes identified and enriched uncharacterized proteins KIAA1361 whose activity was highly increased in aggressive human breast tumor [88] [89]. The further application of fluorophosphonates probes in these cancer cell lines discovered a specific and potent carbamate inhibitor of KIAA1361 that slowed down the migration, invasion and *in vivo* tumor growth of human prostate cancer cell lines using competitive ABPP methods [90]. Recently application of this activity-based probe (ABPP) methodology was applied to MPO with the MPO inhibitor 2-thioxanthine, whereby the heme methyl group of MPO covalently forms the bond with the exocyclic sulfur of 2-TX [11, 19]. The rhodamine azide is able to undergo an alkyne cycloaddition reaction catalyzed by copper [91]. This type of thioxanthine-derived ABPP that senses MPO has future application to inhibitor and interaction screens aimed at understanding

gaps in MPO inhibitor design and biology, respectively.

### **1.8 Concluding remarks**

The development of next generation probes will lay the solid foundation for *in vivo* imaging of MPO, which also can enhance the localization, detectability of MPO and increase signal to noise ratio. The application of these novel probes with differences in tissue distribution and localization in combined modalities will further provide us with more accurate diagnosis and allow us to monitor the progression or therapeutic outcomes of MPO-associated inflammation diseases non-invasively. In addition, the transgenic zebrafish model expressing GFP under the neutrophil-specific *mpx* promoter provides the insights into the mechanism of neutrophil biology in response to wound, this model also can be used to investigate MPO inhibitors in zebrafish to determine whether these compounds can decrease the neutrophils migration and recruitment to the wound.



**Table 1.1 A summary of the sensors for the detection of MPO-derived oxidants and other ROS/RNS.**

Modality	Agent	Molecular Weight (Da)	Excitation $\lambda$ (nm)	Emissions $\lambda$ (nm)	Target	Cell Culture ( <i>in vitro</i> )	Pre-Clinical ( <i>in vivo</i> )
<b>EPR</b>	<b>DMPO</b>	113.2	-	-	$\cdot\text{OH}$ , $\text{O}_2^-$	✓	×
	<b>CMH</b>	201.3	-	-	$\text{ONOO}^-$ , $\text{O}_2^-$	✓	×
	<b>CPH</b>	223.7	-	-	$\text{ONOO}^-$ , $\text{O}_2^-$	✓	×
	<b>mito-TEMPO-H</b>	511.1	-	-	$\text{O}_2^-$	✓	×
	<b>DBNBS</b>	367.0	-	-	$\text{NO}^\cdot$ , $\text{ONOO}^-$ , $\text{O}_2^-$ , MPO	✓	×
<b>Fluorescence</b>	<b>APF</b>	423.4	490	515	$\cdot\text{OH}$ , $\text{ONOO}^-$ , and $\text{HOCl/Br}$	✓	×
	<b>HPF</b>	424.4	490	515	$\cdot\text{OH}$ , $\text{ONOO}^-$	✓	×
	<b>DAF-FM</b>	412.4	495	515	$\text{NO}^\cdot$	✓	×
	<b>H2 DCFDA</b>	487.3	495	527	$\cdot\text{OH}$ , $\text{ROO}^\cdot$ , $\text{ONOO}^-$ , $\text{HOCl}$	✓	×
	<b>HKGreen-3</b>	613.1	520	535	$\text{ONOO}^-$	✓	×
	<b>mito-SOX</b>	759.7	510	580	$\text{O}_2^-$ , heme peroxidases	✓	×
	<b>DHR123</b>	346.4	500	536	$\text{ONOO}^-$ , $\text{NO}_2^\cdot$ , $\text{HOCl}$	✓	×
	<b>HKOCI-1</b>	512.2	520	541	$\text{HOCl}$	✓	×
	<b>DHE</b>	315.4	518	605	$\text{O}_2^-$ , heme peroxidases	✓	×
	<b>ADHP</b>	257.2	571	585	heme peroxidases	✓	✓
	<b>SNAPF</b>	640.0	614	676	$\text{HOCl}$	✓	✓
<b>Quenched nanoparticle</b>	<b>Oxazine nanoparticle</b>	Oxazine 423.3	620	672	$\text{ONOO}^-$ , $\text{HOCl}$	✓	✓
	<b>LS601R-</b>	41,000	785	810	$\cdot\text{OH}$ , $\text{O}_2^-$	✓	✓

	<b>PEG40</b>						
	<b>Lucigenin</b>	510.5	-	470	$O_2^-$ and $H_2O_2$	✓	✓
<b>BLI</b>	<b>Luminol</b>	177.2	-	425	$^{\cdot}OH$ , $ONOO^-$ , $O_2^-$ , $HOCl$ and $HOBr$	✓	✓
	<b>L-012</b>	288.7	-	425	$^{\cdot}OH$ , $ONOO^-$ , $HOCl$ and $HOBr$	✓	✓
	<b>MCLA</b>	291.7	-	465	$O_2^-$ , MPO derived oxidants, $ONOO^-$	✓	✓
	<b>Pholasin</b>	34,600	-	Blue light	$^{\cdot}OH$ , $ONOO^-$ , $O_2^-$ and MPO	✓	✓
<b>CRET</b>	<b>Luminol- QD800</b>	N/A	-	800	MPO derived $HOCl$	✓	✓
	<b>MCLA- BP- AF594</b>	N/A	-	620	$O_2^-$ , and MPO derived oxidants	✓	✓
<b>FRET</b>	<b>HyPer sensor</b>	YFP420 YFP500	420/500	535	$H_2O_2$	✓	✓
<b>MSOT</b>	<b>NIR light- absorbing RSPN1</b>	IR775S 553.7	680	838	$ONOO^-$ , $HOCl$	✓	✓
<b>MRI</b>	<b>Gd-bis-5- HT-DTPA /Gd- 5-HT- DOTA</b>	707.2 788.7	-	-	MPO	✓	✓

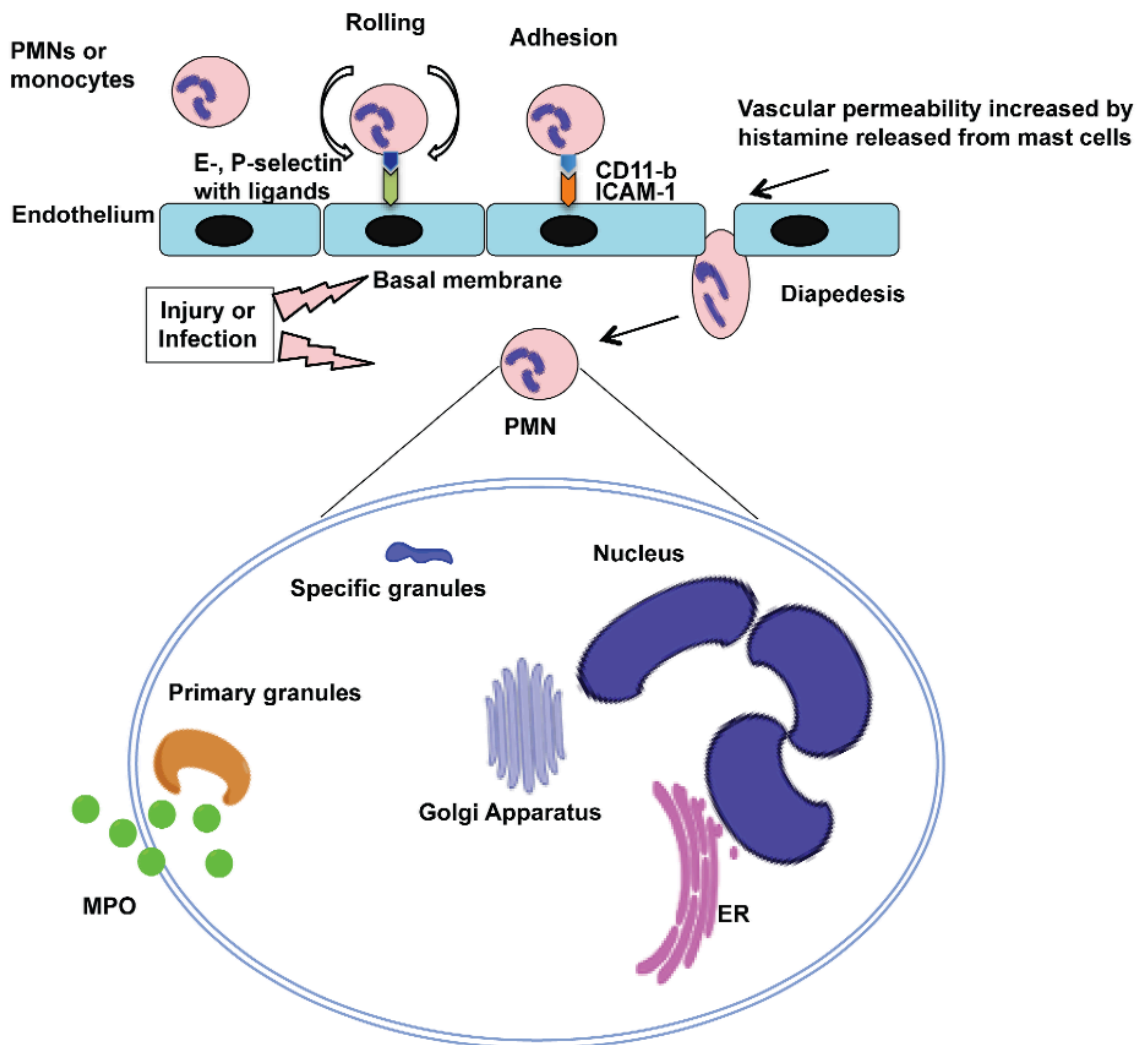


**Figure 1.1 Biology of PMNs in response to injury and inflammation.**

Localized over-expression of E- and P-selectin on activated endothelial cells slow the PMN roll upon endothelium. Responding PMN transmigrate through endothelial cells after  $^{PMN}CD11b$  hooks intercellular adhesion molecule 1 ( $^{EC}ICAM-1$ ) and arrive at the site of damage, just prior to diapedesis caused by increased vascular permeability by histamine released from mast cells. PMNs undergo phagocytosis of invasive microbes once they arrive at the infection site. In addition, MPO is secreted from patrolled neutrophils to produce potent antimicrobial reagent HOCl in response to infection.

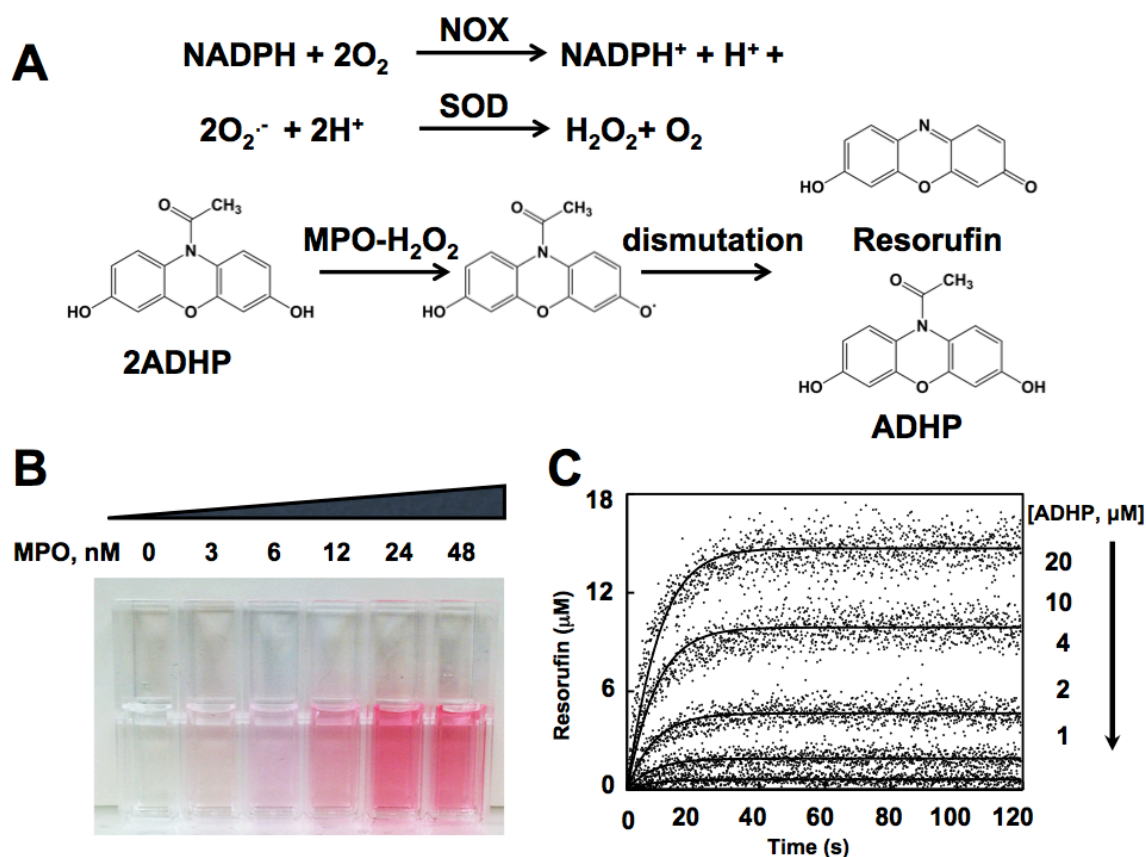


**Figure 1.2 Fluorescence reactions for measuring MPO activity.**

A, General mechanism of ADHP oxidation by a proposed two step reaction, whereby the MPO- $\text{H}_2\text{O}_2$  complex generates two ADHP radicals that undergo a subsequent enzyme independent dismutation reaction to complete formation of one resorufin and one ADHP molecule. B, Classical biochemical assays are possible using absorbance changes caused by the MPO-  $\text{H}_2\text{O}_2$  system and by the use of new fluorogenic probes, such as ADHP. Pictures are cuvettes containing increasing concentrations of the MPO- $\text{H}_2\text{O}_2$  system, as indicated, at static ADHP (40  $\mu\text{M}$ ). C, Stopped-flow progress curves of resorufin generation by MPO (23 nM) initiated by addition of  $\text{H}_2\text{O}_2$  (22  $\mu\text{M}$ ) for a series of given ADHP concentrations (adapted from [28]).

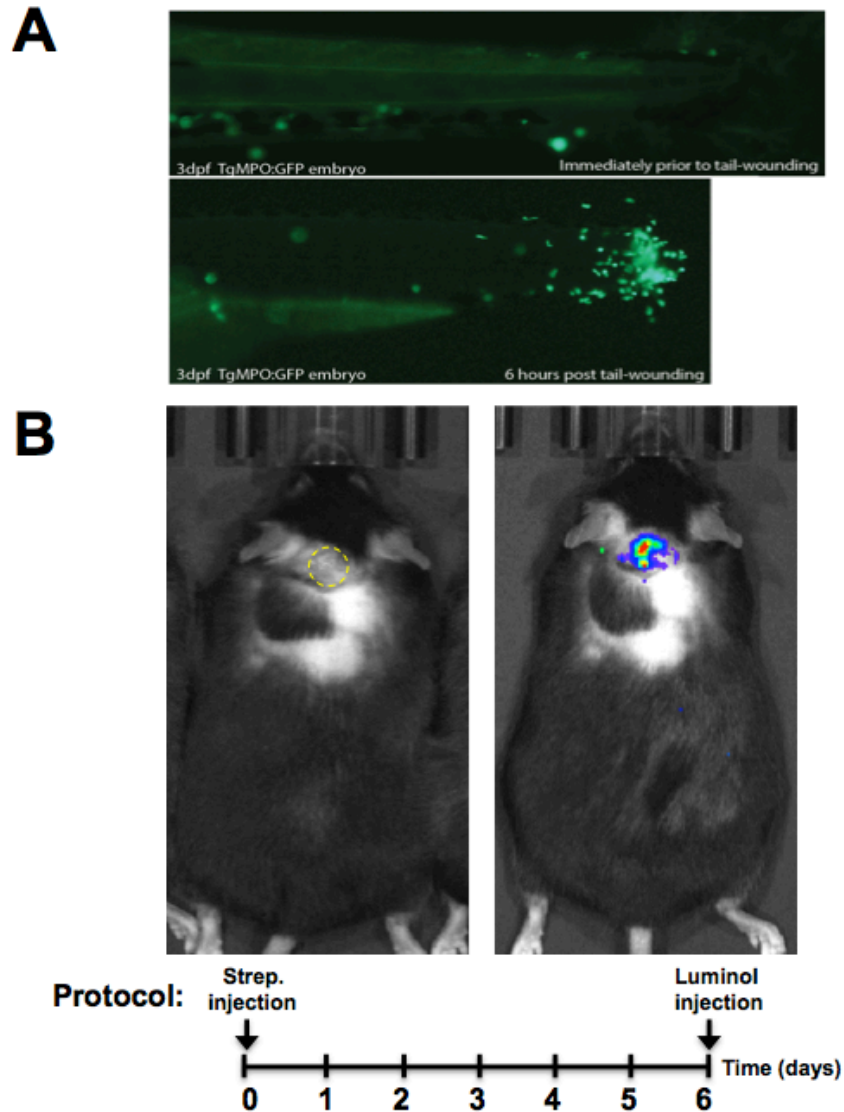


**Figure 1.3 *In vivo* monitoring PMN recruitment in zebrafish and MPO activity in mice.**

A, Tail-tip wound model is examined in green fluorescent protein driven by the MPO promoter.

B, A representative image of a mouse 6 days post subcutaneous injection of *Streptococcus pyogenes* ( $3 \times 10^{10}$  CFU in phosphate buffered saline) in the upper back of the animal shown in white light (*right image*) and bioluminescence imaging (*left image*). To visualize the MPO activity, an intraperitoneal injection of luminol (Sigma, 3 mg per kg body weight) was given 10 minutes prior to imaging using the IVIS Lumina XRMS system (PerkinElmer, Waltham, MA). A yellow dotted circle indicating in the white light photo where the infection was for reference. All

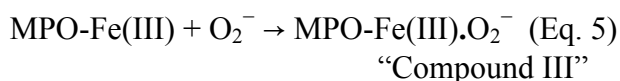
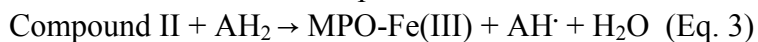
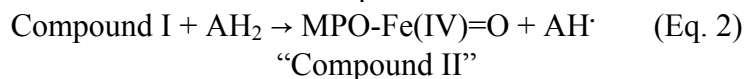
procedures were designed in accordance with the Guide for the Care and Use of Laboratory Animals of the National Institutes of Health and approved by the Institutional Animal Care and Use Committee of Auburn University.

## **Chapter 2 Ordered cleavage of myeloperoxidase ester bonds releases active site heme leading to inactivation of myeloperoxidase by benzoic acid hydrazide analogs**

### **2.1 Introduction**

Myeloperoxidase (MPO) is the only peroxidase capable of consuming hydrogen peroxide ( $\text{H}_2\text{O}_2$ ), in order to catalyze formation of hypochlorous acid (HOCl). Besides MPO-dependent generation of HOCl and hydroxyl radicals ( $\bullet\text{OH}$ ), MPO can accommodate and oxidize a number of small molecule substrates that bind to the active site displacing water molecules that are used in the electron transport chain along the heme ring surface [18]. Here, we sought to better understand the mechanism of MPO-mediated oxidation reactions by use of rapid reaction kinetic analysis of a previous uncharacterized fluorescence substrate to determine the overall kinetic steps from a substrate oxidation vantage point and to use this methodology for rapid characterization of MPO inhibitors for relative potency and mechanism of action.

Enzymatically, MPO follows the classical peroxidase cycle (Eq. 1-3) and is tolerant of diverse pH environments with peak activity in the absence of  $\text{Cl}^-$  exhibited at pH 5.5 [92, 93]. MPO is a ferric iron enzyme (MPO-Fe(III)), which becomes oxidized in the presence of  $\text{H}_2\text{O}_2$  to a short-lived redox intermediate termed compound I (half life  $\sim 100$  ms; [94]), which contains a ferryl  $\pi$  cation radical (MPO-Fe(IV)= $\text{O}^{\cdot+\pi}$ ) (Eq. 1) [95, 96]. Compound I can oxidize halides (e.g.  $\text{Cl}^-$ ,  $\text{Br}^-$ ,  $\text{I}^-$ ) with  $\text{Cl}^-$ , presumably being its main physiological substrate [97]. The MPO-dependent reactions follow the classic peroxidases catalytic cycle shown in Equations 1-3.



Reactive halide (eg.  $\text{Cl}^-$ ) generate HOCl through interaction with Compound I (Eq. 2) but not with Compound II (Eq. 2) or the superoxide inactivated Compound III (Eq. 5).

The active site Fe atom drives these reactions (Eq. 1-5) through octahedral coordination between the central protoporphyrin IX heme and the proximal histidine 336 on the MPO heavy chain ( $^{\text{HC}}\text{His}^{336}$ ), with redox chemistry occurring on the distal surface through displacement of 5 water molecules. There are hydroxylated methyl groups on pyrrole rings A and C that form two ester bonds with evolutionarily conserved peroxidase residues, namely a distal aspartate residue of the light chain ( $^{\text{LC}}\text{Asp}^{94}$ ) and a distal glutamate residue of the heavy chain ( $^{\text{HC}}\text{Glu}^{242}$ ). Interestingly, the active site of MPO differs from other peroxidases in that the heme moiety is slightly bowed cradling the five water molecules and these two ester bond linkages are in this distal heme environment. The heme has in-plane rings B and D and the asymmetry is caused by the aforementioned separate ester bonds with  $^{\text{LC}}\text{Asp}^{94}$  and  $^{\text{HC}}\text{Glu}^{242}$ , as well as a sulfonium ion linkage between the heme 2-vinyl group on ring A and methionine 243 on the heavy chain ( $^{\text{HC}}\text{Met}^{243}$ ) [25]. Due to the unique spectral signature of MPO, some distinct intermediates are produced by Equations 1-5, which can be observed through standard and stopped flow UV-Vis spectroscopy [25] and by magnetic circular dichroism [98, 99]. The MPO signature is exemplified by the Soret band at 430 nm representing the heme moiety with additional lower energy bands that arise from  $\pi$ - $\pi^*$  transitions in the four frontier orbital bands denoted as charge



transfer band 1 (CT1; 496nm),  $\alpha$  (570nm),  $\beta$  (620nm) and CT2 (690 nm) [27, 100]. Covalent modification or destruction of the heme can be monitored through rapid reaction kinetic analysis using stopped flow rapid sequential mixing techniques where changes to these absorbance peaks can be assigned and monitored for changes. Given the tremendous spectral and magnetic properties associational with the catalytic activity of MPO, it is a rich source with which to study enzyme inhibition and structure activity relationships.

It has been reported that certain reactive nitrogen containing compounds such as sodium azide ( $\text{NaN}_3$ ) [101, 102], salicylhydroxamic acid [24, 103], 4-aminobenzoic acid hydrazide (4-ABAH) [96], isonicotinylhydrazine (isoniazid) [104], *N*-acetyl-5-methoxytryptamine (melatonin) [105] and 4-hydroxy-2,2,6,6-tetra-methyl-1-piperidinyloxy (tempol) [106], can inhibit MPO activity. Other sulfur containing MPO inhibitors have also been reported such as diamino-diphenyl sulfone (dapson) [107], and propylthiouracil [108]. Recently, AstraZeneca has gained FDA-approval for the use of an irreversible MPO suicide substrate (2-thioxanthine; AZD5904) in the treatment of chronic obstructive pulmonary disease [19]. Despite the identification of these inhibitors there is no study currently in the literature that has taken on the challenge to analyze their inhibitory parameters for MPO in an attempt to define kinetic steps that govern the inhibitor potential under identical conditions and in parallel. It should be emphasized that despite recent advances in solving MPO-inhibitor crystal structures, there is no current structural data available for the inhibitors examined here.

Our study describes the use of steady state equilibrium and rapid-reaction kinetics investigation of the fluorogenic substrate 10-acetyl-3, 7-dihydroxyphenoxazine (ADHP) for studies of MPO catalysis, characterization of the global dependency of ADHP oxidation by the MPO- $\text{H}_2\text{O}_2$  system and its use to define the mechanism of the widely-used MPO inhibitors

namely 4-ABAH, isoniazid and  $\text{NaN}_3$  before expanding our focus to isomers and analogs of 4-ABAH compounds. The proposed mechanism by which ADHP is oxidized to fluorescent resorufin is shown in Figure 2.1A, whereby an initial ADHP radicals are formed and then interaction with another ADHP is needed to generate one molecule of resorufin [109].

For our studies presented here, we chose to focus on hydrazide analogs prior to moving to other classes of MPO inhibitors. Our results support the hypothesis that 4-ABAH and its isomer 2-ABAH are slow-tight binding inhibitors of MPO requiring at least two independent steps, whereas  $\text{NaN}_3$  and isoniazid-based inhibition have a single observable kinetic / inhibitory step. Covalent modification of MPO active site heme group was also readily apparent by use of ADHP oxidation following equilibrium dialysis of mixtures of the enzyme and its inhibitor, in this case for  $\text{NaN}_3$  or 4-ABAH. We determined that 4-ABAH covalently binds to the MPO enzyme active site, but that inhibition of peroxidase activity is not initiated until after  $\text{H}_2\text{O}_2$  is added. Analysis of the state of the heme moiety and whether it was destroyed by the benzoic acid hydrazide itself lead us to discover that this compound does not destroy the heme but rather mediates the preferential cleavage of the  $^{\text{HC}}\text{Glu}^{242}$  ester linkage causing a chemical rearrangement resulting in loss of the absorbance signature for the MPO sulfonium ion linkage at  $^{\text{HC}}\text{Met}^{243}$ . Mass spectroscopic analysis confirmed the oxylated heme protoporphyrin ring is released through hydrolysis of the ester linkage between  $^{\text{LC}}\text{Asp}^{93}$  and pyrrol ring C generating free heme in solution and MPO light chain. This study collectively demonstrates a new method for comparing MPO inhibitors reliability against one and other with regard to their overall efficacy and assessment of the minimal kinetic steps observed in the ADHP oxidation reactions, and the covalent nature of inhibition and their  $\text{H}_2\text{O}_2$ -dependency. We have used this methodology to define a new mechanism that explains  $\text{H}_2\text{O}_2$  catalyzed hydrazide-based

inhibition of MPO.

## **2.2 Materials and methods**

### **2.2.1 Materials**

Ultra-pure myeloperoxidase (MPO) was purchased from Lee Biosolutions Inc. (St. Louis, MO) and 10-acetyl-3, 7-dihydroxyphenoxazine (ADHP) was purchased from ABD Bioquest Inc. (Sunnyvale, CA). Sodium acetate, 3,3', 5,5'-tetramethylbenzidine (TMB), H<sub>2</sub>O<sub>2</sub>, 2-aminobenzoic acid hydrazide (2-ABAH), 4-(trifluoromethyl) benzoic acid hydrazide (4-TFMBAH), 3-(dimethylamino) benzoic acid hydrazide (3-DMABAH) were obtained from Sigma-Aldrich (St. Louis, MO, USA). 4-aminobenzoic acid hydrazide (4-ABAH), benzoic acid hydrazide (BAH), 4-fluorobenzoic acid hydrazide (4-FBAH), 4-nitrobenzoic acid hydrazide (4-NBAH), sodium azide (NaN<sub>3</sub>), Dimethyl sulfoxide (DMSO) were obtained from Alfa Aesar (Ward Hill, MA). For gel staining reagent Gelcode Blue and enhanced chemiluminescence reagent Western Lightning ultra was purchased from Pierce (Rochford, IL) and Perkin Elmer (Waltham, MA), respectively.

Sodium acetate buffer was adjusted with acetic acid to pH 5.6 (assay buffer). H<sub>2</sub>O<sub>2</sub> stock of 30% from obtained from BDH Chemicals (London, UK) and diluted to concentration on the day of the experiment with concentration verified by absorbance at  $\lambda_{240\text{nm}}$  using an extinction coefficient of 39.4 M<sup>-1</sup>cm<sup>-1</sup> [110]. ADHP, 4-ABAH, 2-ABAH, 4-BAH, 4-FBAH, 4-NBAH, 4-TFMBAH, 3-DMABAH, NaN<sub>3</sub> and isoniazid were dissolved in DMSO and subsequently diluted into assay buffer. The final concentration of DMSO in the reaction was less than 0.5 % (v/v), which did not affect fluorescence of the oxidized ADHP product 7-hydroxyl-3H-phenoxazin-3-one (resorufin; data not shown).

### **2.2.2 Steady state analysis of MPO activity kinetics**

ADHP oxidation (Figure 2.1A) was measured as a function of  $\text{H}_2\text{O}_2$  by use of Varioskan Flash plate reader with excitation of  $\lambda_{530\text{nm}}$  and emission of  $\lambda_{590\text{nm}}$ . Reactions of ADHP (20  $\mu\text{M}$ ) were incubated with MPO (2.8 nM) in assay buffer and initiated by the addition of 1/ 10th volume  $\text{H}_2\text{O}_2$  from a serial dilution basin. Initial rates for the velocity of these reactions plotted against  $\text{H}_2\text{O}_2$  concentration and kinetic parameters (Figure 2.1B). Due to the rapid rate of the reaction initial rates were obtained using the auto-injection functionality built into the reader. SkanIt software 2.4.3 parameters included an interval of 0.1 s for each of 1000 reads. Data was timed to remove the substrate depletion exhibited by the high rate of the substrate turnover and used to obtain approximation of the kinetic parameters of Compound I of the MPO- $\text{H}_2\text{O}_2$  system. These results were confirmed by analysis by simultaneous fits of the progress curves obtained in the stopped flow data as an ADHP dependency.

### **2.2.3 Transient state analysis by stopped flow kinetics**

ADHP oxidation (Figure 2.1A) was measured as a function of fluorescence intensity over time using QuantaMaster 80 (Photon Technology International, Birmingham, NJ) with a Xe - Arc lamp. Mixtures of MPO and ADHP were rapidly mixed with  $\text{H}_2\text{O}_2$  in acetate buffer (assay buffer) using RX2000 rapid mixing stopped-flow accessory (Applied Photophysics Ltd, Leatherhead, UK) under constant 25°C reaction conditions using isotemp 3016D (Fisher Scientific, Pittsburgh, PA). In addition, the mixture of MPO with ADHP and  $\text{H}_2\text{O}_2$  in assay buffer were loaded into two different drive syringes of the stopped-flow apparatus and maintained at 25°C for at least 10 min prior to triggering the pneumatic driver. Experiments were initiated with the optimized concentration of  $\text{H}_2\text{O}_2$  (22  $\mu\text{M}$ ; refer to Figure 2.1B) and performed in a total final volume of 500  $\mu\text{L}$ . After initiation by  $\text{H}_2\text{O}_2$ , we measured the time-dependent fluorescence change of produced resorufin using an excitation wavelength of 530 nm and an

emission wavelength of 590 nm to follow the reaction. Felix GX4.2.2 captured 10 reads per 1 s for 120 s. For all experiments, the slit widths of the spectrofluorometer were set to 8 nm excitation and 2 nm emissions. The fidelity of the kinetic experiments was maintained by RX pneumatic drive of stopped-flow rapid mixing accessory and recordings started prior to triggering rapid mixing of the reactants. The kinetic traces were trimmed to eliminate the delay in observed fluorescence change following mixing and each curve represents an average of at least 4 independently triggered event traces.

#### 2.2.4 Fluorescence data analysis

Raw fluorescence intensity measurements were converted into molar resorufin production using a standard curve. Sets of progress curves were initially fit with either a single or double exponential function using GraphPad Prism 5.0. The apparent first order rate constant ( $K_{on}^{app}$ ) was obtained by fitting  $k_{obs}$  independently versus the concentration for ADHP and MPO (see Figure 2.2);

$$Y = [c + a \exp(-k_{obs} * t)] \quad (\text{Eq.6}),$$

where y is the molar product formed, t is time, a is amplitude of the decay, c is the signal at infinite time and  $k_{obs}$  is the exponential rate constant.

#### 2.2.5 Simultaneous fits of progress curves to determine the specificity constant of MPO-H<sub>2</sub>O<sub>2</sub> system for ADHP

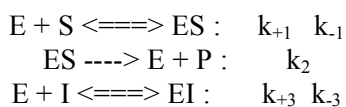
To obtain  $K_m$  and  $k_{cat}$ , Scientist software (MicroMath Inc., Saint Louis, Missouri) was used to fit simultaneously the produced resorufin progress curve as a function of ADHP concentration for the MPO-H<sub>2</sub>O<sub>2</sub> system (23 nM/ 22 μM) using the integrated Michaelis-Menten equation;

$$T = \left\{ \left( \frac{K_m}{k_{cat} * E_0} \right) * \ln \left( \frac{S_0}{S_0 - P} \right) + \left( \frac{P}{k_{cat} * E_0} \right) \right\} \quad (\text{Eq. 7}),$$

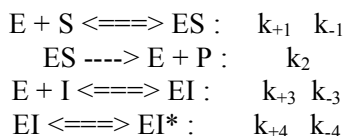
where P is the concentration of product formed, T is time,  $E_0$  is the total concentration of enzyme,  $S_0$  is the initial concentration of substrate ADHP,  $K_m$  is the Michaelis-Menten constant, and  $k_{cat}$  is the rate of substrate turnover.

### 2.2.6 Global analysis of the MPO inhibition

For the inhibitory effect of ABAH on MPO activity, a set of the time-dependent fluorescence progress curves was fit simultaneously by a slow-tight binding model using DynaFit 3 software ([111]; Biokine, Ltd. Watertown, MA, USA). Kinetic models of a one-step or a two-step mechanism are shown as follows:



#### Scheme I. The one-step model tested.



#### Scheme II. The two-step model tested.

The inhibitory efficiencies for the inhibitory effects of 4-ABAH and its analogs on MPO activity are obtained from DynaFit software. The overall inhibition constant ( $K_i$ ) associated with the formation of the reversible EI complex was determined when it met the model of a one-step slow tight-binding inhibitor, such as:

$$K_i = k_{-3} / k_{+3} \quad (\text{Eq. 8}).$$

When the inhibitory pattern met the requirement of a two-step slow tight-binding inhibitor model, the overall inhibition constant was determined as given by the following equation:

$$K_i^* = \frac{[E][I]}{[EI]+[EI^*]} = K_i \left( \frac{k_{-4}+k_{+4}}{k_{-4}} \right) \quad (\text{Eq. 9}).$$

$k_{+3}$ ,  $k_{-3}$ ,  $k_{+4}$ ,  $k_{-4}$  were obtained from simulating a set of fluorescence progress curves inhibited by different inhibitors using DynaFit 3, where  $K_i = k_{-3}/k_{+3}$ .

### 2.2.7 SDS-PAGE analysis

To determine the effect that the simplest benzoic acid hydrazide inhibitor or its analog 4-TFMBAH has on the heme catalytic ability of MPO, we incubated MPO (1.2  $\mu\text{M}$ ) for 10 min with different concentrations of BAH inhibitor (0, 0.025, 0.25, 2.5, 12.5 and 25 mM) with ADHP (40  $\mu\text{M}$ ) and timing of the reaction was measured following addition of  $\text{H}_2\text{O}_2$  (20  $\mu\text{M}$ ). All reactions were measured in assay buffer at room temperature. Samples of 20  $\mu\text{L}$  were added to non-reducing sample loading buffers, and then loaded without prior heating and resolved by 4-15% gradient SDS-polyacrylamide gel electrophoresis. Note that heat treatment was avoided due to the established autocatalytic cleavage of MPO heavy chain that results in the appearance of a 39 and 20 kDa band by SDS gel electrophoresis through specific cleavage of the  $^{\text{HC}}\text{Met}^{243}\text{-}^{\text{HC}}\text{Pro}^{244}$  bond [112, 113]. Total protein stained by GelCode Blue reagent (Pierce) and the location and status of the heme moiety of MPO was probed by use of Western Lightning reagent (Perkin Elmer) directly on the gel with images collected with a Fujifilm LAS-1000 luminescence imager.

### 2.2.8 MALDI-TOF method

Matrix-assisted laser desorption/ionization time-of-flight (MALDI-TOF) mass spectroscopy was used to analyze reaction conditions that were determined to maximized light

chain-heme formation products generation as determined by protein electrophoresis, namely MPO (1.2  $\mu$ M) with BAH (2.5 mM) pre-incubated for 10 min prior to the addition of H<sub>2</sub>O<sub>2</sub> (20  $\mu$ M). Protein samples were diluted to optimal concentration and spotted onto a 96-well plate using a sandwiched method where the protein solution was diluted 1 to 1 with sinapinic acid matrix (30 mg matrix in 1 ml 33% acetonitrile, 0.1% TFA, freshly prepared) were let air dry to complete at room temperature, and rinsed with H<sub>2</sub>O and dried prior to sinapinic acid matrix addition (1  $\mu$ L) to allow for crystal growth. The spectra were acquired using a MALDI-TOF (Microflex, Burker Daltonics) with flexControl (version 3.3) and data analysis by flexAnalysis software (version 3.3). Mass calibration used Insulin and BSA for instrument and for external spectrum. Laser power and voltages were tuned so an optimum signal to noise ratio was achieved. MALDI spectrum was calibrated against external standard, smooth and subtracted background. MPO parent and cleaved fragments with and without heme were identified in the MALDI spectrum range from 10,000 to 150,000 Da.

### **2.2.9 Liquid chromatography with tandem mass spectroscopy method**

Protein samples were prepared identical to the MALDI-TOF measurements but instead analyzed using an Ultra Performance LC Systems (ACQUITY, Waters Corp., Milford, MA) coupled with a quadrupole time-of-flight mass spectrometer (Q-TOF Premier, Waters) with electrospray ionization (ESI) detector in positive ion mode operated by the Masslynx software (V4.1). Each sample in H<sub>2</sub>O were injected into a C18 column (ACQUITY UPLC® BEH C18, 1.7  $\mu$ m, 2.1 x 50 mm, Waters) with a 150  $\mu$ L/min flow rate of mobile phase of solution A (95% H<sub>2</sub>O, 5% acetonitrile, 0.1% formic acid) and solution B (95% acetonitrile, 5% H<sub>2</sub>O, 0.1% formic acid) in a 10 min gradient starting at 95% A to 5% A in 6 min and back to 95% in 8 min.

The ion source voltages were set at 3 KV, sampling cone at 37 V and the extraction cone



at 3 V. The source and desolvation temperature were maintained at 120°C and 225°C, respectively, with the desolvation gas flow at 200 L/h. The TOF MS scan was from 500 to 3500  $m/z$  at 1 s with 0.1 s inter-scan delay. For real time mass calibration, direct infusion of sodium formate solution (10% formic acid/0.1M NaOH/isopropanol at a ratio of 1:1:8) at 1 sec/10 sec to ion source at 1 $\mu$ L/min was used. Scans at 4 min peak (data not shown) of 10 min LC chromatogram were combined, the multiply charged protein envelop from 800 to 2100  $m/z$  were processed using MaxEnt1 (Masslynx) to deconvolute to the molecular ion with iterations that converged. The spectrum was then smooth and centered to obtain the molecular mass. Result from LC-ESI<sup>+</sup>-MS measurement agrees with those by MALDI-TOF. For clarity, the MALDI-TOF results are shown in this paper.

## 2.3 Results

### 2.3.1 Effect of H<sub>2</sub>O<sub>2</sub> on oxidation of ADHP by MPO

Our initial attempts at characterization of the MPO-H<sub>2</sub>O<sub>2</sub> system involved use of guaiacol and 3, 3', 5, 5'-tetramethylbenzidine (TMB)-based absorbance assays because of our previous success in the use of these substrates in tissue homogenate assays of MPO activity [72, 114-116]. The oxidation of ADHP by MPO in the presence of H<sub>2</sub>O<sub>2</sub> is an ordered two-substrate (a.k.a. Ping-Pong) reaction (Figure 2.1A). Solubility issues of TMB under the reaction conditions over the range necessary for accurate  $K_m$  determination limited its utility. Similar problems were seen for guaiacol, which when added to buffer is a suspension not a true solution but these issue did not occur with ADHP. For oxidation of ADHP by MPO, reactions reached a plateau after 20 s following H<sub>2</sub>O<sub>2</sub> addition. It has been well documented that H<sub>2</sub>O<sub>2</sub> concentrations have a profound impact on the catalytic activity of MPO [93], but there is still uncertainty regarding the cause of this phenomena. During the preparation of this manuscript, Kettle *et al.* reported that H<sub>2</sub>O<sub>2</sub> at

high concentrations resulted in suicide inhibition of MPO by degradation of the heme linkage due to modification of methionine residues [117]. Interestingly, in that study  $^{\text{HC}}\text{Met}^{243}$  was not one of the methionine groups oxidized by  $\text{H}_2\text{O}_2$ . Furthermore, it was confirmed that our ratio of MPO to  $\text{H}_2\text{O}_2$  concentrations used here would represent Compound I (Figure 2.1B) and validates our contention that the kinetic properties would represent a defined species in the MPO reaction mechanism. Initially, we wanted to ensure that assessment of any of the MPO inhibitors was performed at the pinnacle of the  $\text{H}_2\text{O}_2$  dependency on the specificity constant for the enzyme ( $k_{\text{cat}}/K_m$ ) for ADHP, as such the relationship between velocity of ADHP oxidation at various  $\text{H}_2\text{O}_2$  concentrations was determined using the integrated Michaelis-Menten equation including  $\text{H}_2\text{O}_2$  substrate inhibition driven by the modification of methionine residues by the  $\text{H}_2\text{O}_2$ . Our results indicated that  $\text{H}_2\text{O}_2$  dependence of MPO activity was fit well to a model that included a substrate inhibition step with an apparent inhibitory rate constant  $K_i$  of 10.8 nM of this  $\text{H}_2\text{O}_2$  effect (Figure 2.1B) with data fitting, a maximal velocity of  $26 \mu\text{M s}^{-1}$  was demonstrated. Interpretation of the significance of this  $K_i$  value is problematic and not pursued further as it may represent a collective effect resulting from oxidation of several MPO residues.

### 2.3.2 Michaelis-Menten analysis of the ADHP substrate by MPO- $\text{H}_2\text{O}_2$ system

To obtain the Michaelis-Menten parameters  $K_m$  and  $k_{\text{cat}}$  for Compound I (Eq. 1), we chose two independent methods. Initially, we studied the oxidation of ADHP using the injector functionality built-in to the VarioSkan Flash fluorescence plate reader. The auto-injector dispensed the  $\text{H}_2\text{O}_2$  to initiate the reaction, as a means of generating a set of progress curves. Plots of initial velocities as a function of different concentrations of substrate ADHP are shown in Figure 2.1C. Michaelis-Menten analysis for MPO-mediated oxidation of ADHP gave a  $K_m$  of  $31 \pm 4 \mu\text{M}$  and the  $k_{\text{cat}}$  of  $186 \pm 6 \text{ s}^{-1}$ .

Our second method for determination of these Michaelis-Menten parameters was to use ADHP in stopped flow fluorescence spectroscopy studies. This method involved collection of the full substrate depletion / progress curves for molar product formed (also known as resorufin) and simultaneous fitting to the integrated Michaelis-Menten equation (Eq. 7) using Scientist software (Figure 2.1D). A residual plot stands for the goodness-of-fit of the model to the data (data not shown). The integrated Michaelis-Menten analysis determined the  $K_m$  to be  $39 \pm 11 \mu\text{M}$  with a  $k_{\text{cat}}$  of  $224 \pm 50 \text{ s}^{-1}$ . These two independent methods gave overlapping values and provided confidence as to initial values needed to begin analysis of the hydrazide analogs as MPO inhibitors. All errors are reported as 2 times standard deviations.

### 2.3.3 Characterization of ADHP conversion to resorufin by the MPO-H<sub>2</sub>O<sub>2</sub> system

Initially, we sought to determine the behavior of the ADHP substrate as a reporter of Compound I (Eq. 1), specifically how reaction  $V_{\text{max}}$  varied as a function of either altered substrate concentration (Figure 2.1D) or varied enzyme concentration (Figure 2.1E). Titrations demonstrate increasing reaction velocity over the range of ADHP substrate concentration assayed, namely 1, 2, 3, 10, 20, 40, 60, 70, and 80  $\mu\text{M}$  ADHP with MPO at 23 nM and H<sub>2</sub>O<sub>2</sub> at 22  $\mu\text{M}$  (Figure 2.1D). The enzyme dependency is shown in Figure 2.1E with constant ADHP concentration of 40  $\mu\text{M}$  with similar behavior exhibited. Observed rate constant ( $k_{\text{obs}}$ ) for both dependencies was calculated from single exponential function using the non-linear regression function built into GraphPad Prism 5.0. As expected, the  $k_{\text{obs}}$  also increased over the experimental range of ADHP concentrations from 1 to 80  $\mu\text{M}$  (Figure 2.1F) and for the converse experiment holding substrate constant over 3 to 45 nM MPO (Figure 2.1G). The apparent second order rate constant ( $K_{\text{on}}^{\text{app}}$ ) obtained from the slope of  $k_{\text{obs}}$  against ADHP concentration  $K_{\text{on}}^{\text{app}}$  was  $2.1 \pm 0.2 \text{ mM}^{-1} \text{ s}^{-1}$ .

### 2.3.4 Lineweaver-Burk analysis of 4-ABAH and $\text{NaN}_3$ -based inhibition of the MPO- $\text{H}_2\text{O}_2$ system

To determine the mechanism by which 4-ABAH inhibits MPO; we initially attempted to generate the classic Lineweaver-Burk profile to determine competitive, noncompetitive and mixed-type inhibition for 4-ABAH. In general, multi-substrate systems are typically not amendable to this analysis [118], due presumably to the multiple velocities observed. The reaction of MPO with 4-ABAH has been reported to be irreversible [96] and as such permanently disabled and was not competitive in nature. Unlike reversible inhibitors these types of mechanisms of inactivation are time-dependent as formation of a covalent bond can be generally slow, so we further sought to determine the number of steps that could be observed using ADHP as a reporter.

To determine the mechanism by which  $\text{NaN}_3$ , inhibits MPO, we initially wanted to confirm whether  $\text{NaN}_3$  was a reversible inhibitor in the absence of  $\text{H}_2\text{O}_2$ . ADHP oxidation was measured for a control reaction with  $\text{NaN}_3$  and before and after equilibrium dialysis (Figure 2.2A). Results indicated that  $\text{NaN}_3$  binding to the MPO enzyme was itself reversible as near complete fluorogenic potential was recovered (see the difference between progress curves b and c in Figure 2.2A). From there, we sought to conduct a full Lineweaver-Burk profile of  $\text{NaN}_3$  binding / inhibition of Compound I. Figure 2.2B shows the profile produced via auto-injection of substrate  $\text{H}_2\text{O}_2$  with a Varioskan Flash plate reader. The results of this experiment showed that  $\text{NaN}_3$  inhibits MPO by a competitive inhibition or mixed-type inhibition with ADHP (Figure 2.2B). From this, kinetic parameters ( $k_{\text{cat}}$  of  $207 \text{ s}^{-1}$  and  $K_{\text{m}}$  of  $28.8 \mu\text{M}$ ) for MPO oxidation of ADHP were determined from curves in the absence of inhibitor. These values were identical to values determined initially determined (Figure 2.1 and data not show). From interpretation of the

Lineweaver-Burk plots, the addition of  $\text{NaN}_3$  ( $7.5 \mu\text{M}$ ) decreased the apparent  $k_{\text{cat}}$  to  $161 \text{ s}^{-1}$  and the apparent  $K_m$  to  $111 \mu\text{M}$ . This result was extended when  $30 \mu\text{M}$   $\text{NaN}_3$  was added further decreasing the  $k_{\text{cat}}$  ( $108 \text{ s}^{-1}$ ) and the apparent  $K_m$  ( $167 \mu\text{M}$ ). This represents a 11-fold reduction in the apparent specificity constant ( $k_{\text{cat}}/K_m$ ) for the native system as compared to the highest concentration of  $\text{NaN}_3$  tested.

### **2.3.5 Global analysis of 4-ABAH on oxidation of the ADHP substrate by the MPO- $\text{H}_2\text{O}_2$ system by use of DynaFit modeling software**

Here we explored whether hydrazide analogs are indeed slow-tight binding inhibitors of MPO. Initially, we analyzed sets of 4-ABAH-dependent inhibition of MPO activity and altered 4-ABAH under constant ADHP concentration and compiled them in the DynaFit software. Simultaneous modeling of these curves with initial Michaelis-Menten parameters determined for the simplified MPO- $\text{H}_2\text{O}_2$  system (Figure 2.1) allowed us to discriminate between the one step model (Scheme I) and a two-step model (Scheme II) of slow binding inhibition. DynaFit results are shown in Table 2.1, where appropriateness of the model is assessed by automatic Akaike information criterion [119, 120]. The inhibitory efficiencies measured by DynaFit modeling for the inhibitory effects of 4-ABAH on MPO activity are shown in Table 2.2. Our results of  $\text{NaN}_3$  for the one-step model fit of slow binding inhibition can be found in Figure 2.3A and results for the two step model of the slow binding inhibition mechanism for 4-ABAH are shown in Figure 2.3B. The corresponding residual plots from Dynafit 3 are shown in their bottom panels, respectively.

### **2.3.6 Effect of 4-ABAH on oxidation of the ADHP substrate by MPO- $\text{H}_2\text{O}_2$ system**

Due to the fact that individual progress curves for 4-ABAH can be modeled well using a simple double exponential expression, we hypothesized that 4-ABAH could be acting as a slow-

tight binding irreversible inhibitor of MPO. To test this, we first had to confirm that 4-ABAH was an irreversible inhibitor of Compound I by equilibrium dialysis and reanalysis by stopped flow fluorescence spectroscopy. Our dialysis result showed no increase in activity post-dialysis indicating a permanent modification to the MPO active site (Figure 2.4A and Figure 2.4B). Phenotypically, there was loss of one step involved in 4-ABAH mediated inhibition of MPO, presumably due to pre-incubation of the reactants. It is worth noting that the presence of  $H_2O_2$  is required for this irreversible inhibition of MPO by 4-ABAH, consistent with the literature [96].

### **2.3.7 Comparison of hydrazide analogs and their effect on oxidation of ADHP by the MPO- $H_2O_2$ system**

We sought to compare the inhibition of Compound I by hydrazide-containing compounds with various electron withdrawing and electron donating groups. The  $IC_{50s}$  for different inhibitors using the half maximum of ADHP oxidation are shown along with their respective structures in Table 2.3. For comparison, kinetic parameters were also determined for isoniazid and  $NaN_3$ . Akaike information criterion based discrimination analysis is shown in Table 2.1, with 2-ABAH fitting best with a two-step slow binding inhibitor  $K_i^*$  of 0.16  $\mu M$ , which has a similar effect as 4-ABAH (Figure 2.3B). 3-DMABAH,  $NaN_3$ , 4-TFMBAH, and isoniazid are all best represented by a one-step slow binding inhibition model as shown in Table 2.2 with  $K_i$  of 0.56  $\mu M$ , 0.84  $\mu M$ , 3.08  $\mu M$ , 10  $\mu M$ , respectively. These results indicate that 2-ABAH is a 62-fold higher affinity inhibitor of Compound I as compared to isoniazid under the conditions tested. To evaluate this phenomenon further, the relationship between the overall inhibitory rate constants  $K_i$  for the *meta*- and *para*-substituted compounds with respect to the appropriate Hammett coefficients ( $\sigma$ ) were examined as shown in Figure 2.5A. It is linear between the  $\sigma$  value and its corresponding  $K_i$ . Further examination of the dependency of the  $\sigma$  value with respect to the phenomenological

IC<sub>50</sub> values showed a linear but less precise relationship (Figure 2.5B). There was weak linear correlation between the inhibitor constants and the hydrophobicity of the substituent under our conditions as shown in Figure 2.5C.

### **2.3.8 Benzoic acid hydrazide and analog mediated cleavage of MPO**

It has been reported that the heme group linked to the MPO active site can be degraded by H<sub>2</sub>O<sub>2</sub> when it was added to MPO at a 1000:1 ratio and incubated for 2 hrs [117]. As is shown in Figure 2.6A, the light chain of MPO is cleaved from MPO as we increase the concentration of BAH because the heavy chain (58.5 kDa) and light chain (14.5kDa) are linked via their covalent bond with the heme prosthetic group [117]. MPO is a dimer of heterodimers (146 kDa) consists of two identical glycosylated heavy and two light chains with the heavy chains linked by a single disulfide bond. Interestingly, once cleavage of the heme ring occurs the iron containing active site heme migrates with the light chain as evident by its ability to oxidize the chemiluminescent substrate (Figure 2.6B). Examination of the concentration dependence of this cleavage also shows a progressive loss of one and then both of the MPO light chains converting the MPO heavy chain into a specific product without peroxidase potential. To determine whether this observation was an isolated BAH phenomena, we tested in the same manner 4-TMFBAH, which showed a similar results, but with slightly altered concentration dependency (Supplementary Figure 2.1). These results indicate that the heme moiety was not degraded and remained intact with the Fe remaining coordinated in such a way as to still allow for peroxidase activity.

### **2.3.9 Analysis of hydrazide induced cleavage product by mass spectroscopy**

We were interested in determining the exact mass of the fragments of MPO generated in reaction mixtures of MPO, BAH and H<sub>2</sub>O<sub>2</sub>. To address these we used parallel techniques of MALDI-TOF and tandem liquid chromatography and electrospray mass spectroscopy. Our

results are shown in Figure 2.7, where a reference active site of MPO and linkage between ester of the hydroxylated methyl groups with (<sup>LC</sup>Asp<sup>94</sup>) and a distal <sup>HC</sup>Glu<sup>242</sup> are shown by the blue arrows in Panel A and the MALDI-TOF data is shown in Panel B. For clarity, the heme group in MPO is a protoporphyrin IX group or also referred to as heme b, which is comprised of a tetrapyrrole structure with rings denoted as A, B, C and D (Figure 2.7A). Although we noted peaks associated with the MPO dimer representing MPO (HC-heme b-LC), monomer of MPO (HC-heme b-LC), and cleavage products, we honed in on peaks of interest critical for our question coinciding with the range between 8,000 to 20,000 Da (Figure 2.7B). Our results indicate peaks in this range with  $m/z$  13,056.1 Da, which is converted overtime into a  $m/z$  12,407.1 Da peak representing a mass difference of 649.00 Da (data not shown regarding time course). The calculated average mass of heme b ( $C_{34}H_{32}FeN_4O_4$ ) is 616.48 Da and the addition of 2 oxygen molecules would render a theoretical mass nearly identical to the results we obtained ( $C_{34}H_{32}FeN_4O_6$ ; 648.49 Da). The appearance of the second cleavage product is important as it also explains why we also saw diminished chemiluminescence for the peroxidase activity in band roughly correlating to the LC-heme b reaction product at high concentration of the BAH (data not shown) and for 4-TFMBAH (Supplementary Figure 2.1). It should be emphasized that reactions without BAH or with high level of  $H_2O_2$  compared to MPO (1000 to 1 molar ratio) did not result in these ester cleavage products. Presumably, hydrolysis of the second ester is also by a nucleophilic acyl substitution to generate a free form of heme b with any modifications made to the rings by these cleavage reactions and as it turns out in our gel experiments it results in a LC band devoid of catalytic potential. As a confirmation that this result was not an artifact of the MALDI-TOF technique and preparation, we also performed a parallel liquid chromatograph and electrospray mass spectroscopy experiment that showed a parent monomer MPO (i.e. LC-Heme



b-HC) peak at  $m/z$  77,368 Da and a cleaved HC corresponding to the  $m/z$  64,470 Da peak. This results in difference of 12,898 Da, which is in good agreement the value seen for the electrospray mass of the LC-heme b intermediate of  $m/z$  13,049.5 Da.

### **2.3.10 Analysis of the spectral changes that occur during MPO based hydrazide inhibition**

In recent years, mechanistic studies on the interaction of MPO with potential active site ligands have been based primarily and on measurements of spectral changes that accompany formation of reactive heme intermediates (Eq. 1-5) during the myeloperoxidase catalytic cycle [19, 20, 96, 105, 106]. The spectral signature displays the classic Soret peak and four lower energy Q bands (Figure 2.7C). One of these bands is formed by the sulfonium linkage that heme makes with  $^{\text{HC}}\text{Met}^{243}$ . Of note, Kettle *et al.* recently reported that the  $^{\text{HC}}\text{Met}^{243}$  was not one of the methionine groups oxidized by high concentrations of  $\text{H}_2\text{O}_2$  leading to MPO inactivation [117]. Here, we sought to identify whether the sulfonium linkage is maintained in the BAH-mediated cleavage products or whether this unique bond is lost. We noted a blue shift of the 430 nm Soret peak to 418 nm peak when  $\text{H}_2\text{O}_2$  was added. There was also loss of both the  $\alpha$  (570nm) and CT2 (690 nm) peaks (Figure 2.7C). Collectively, these results indicate that the sulfonium linkage with  $^{\text{HC}}\text{Met}^{243}$  was lost with incubation of MPO with BAH and  $\text{H}_2\text{O}_2$ .

## **2.4 Discussion**

Mechanistic studies on the interaction of MPO with potential active site ligands have been based primarily, in recent years, on measurements of spectral changes that accompany formation of reactive heme intermediates (Eq. 1-3) during the classic peroxidase catalytic cycle [19, 20, 96, 105, 106]. This is a powerful technique that allows correlation of various agents or conditions on the formation of this short-lived Compound I and conversion to Compound II defined by Equation 1 & 2, respectively. Other studies have sought to characterize the potential

role of the chlorination cycle (Eq. 4) and its interplay with the peroxidase activity of enzyme and the potential added complexity of superoxide intermediate reactions (Eq. 5) and the superoxide dismutase activity of the MPO active site [121, 122]. Here we sought initially to provide a reliable platform to compare MPO inhibitors in the broadest sense without introducing questions of experimental bias (i.e. comparisons of potency across platforms). Furthermore we wanted to utilize a system or assay that was amendable to future high through put screening efforts. We chose here to study the fluorogenic peroxidase substrate ADHP [49, 123] as it has properties amendable to this goal. Furthermore, we wanted to study this substrate under conditions that maximize MPO function (i.e. pH 5.6) and in the absence of  $\text{Cl}^-$  ions, thereby eliminating the 2-electron transfer in Equation 5. Using this strategy, we determined the Michaelis-Menten parameters for MPO oxidation of ADHP (Figure 2.1). Once we confirmed the reliability of this new method and appropriate substrate / enzyme relationship occurred, we tackled the problem of examining the classic MPO inhibitors like  $\text{NaN}_3$  (Figure 2.2 & 2.3) and 4-ABAH (Figure 2.3 & 2.4). Keeping in mind that we were focused on a systematic approach to examining these inhibitors, we collected transient kinetic datasets for each inhibitor (Table 2.3) and then batch-wise analyzed them with DynaFit modeling software to assure consistent handling of the data. We were able to validate the obtained  $K_i$  and  $K_i^*$  values by these methods and compare them to the original phenotypic  $\text{IC}_{50}$  values (Table 2.3). From our results, we determine that both 2-ABAH and 4-ABAH were the most potent MPO inhibitors causing their action through a slow-tight binding mechanism with respective  $K_i^*$  formation rates of 0.16 and 0.23  $\mu\text{M}$ , which is in good agreement with the respective observed  $\text{IC}_{50}$  values of 0.71 and 0.50  $\mu\text{M}$  (Table 2.2). Furthermore 2-ABAH and 4-ABAH inhibited by a two-step mechanism as opposed to the other BAH and  $\text{NaN}_3$  inhibitors tested (Table 2.1) suggesting that the mere presence of the amino

group at either position on the BAH would be favorable; leading to this second step interaction.

A simple yet powerful benefit to the use of ADHP was our ability to discriminate between covalent and non-covalent interaction of the inhibitors with MPO in the absence of  $H_2O_2$  providing direct insight into the overall mechanism of action of a given compound. We examined the reversibility of the compound inhibitor by dialyzing mixes of the MPO and, for this experiment, either with  $NaN_3$  shown in Figure 2.2 and 4-ABAH in shown in Figure 2.4. It is established that  $NaN_3$  inhibits peroxidases by modification to the heme ring through formation of a  $\delta$ -meso-azidoheme adduct rather than direct interaction of the azide with the chelated Fe molecule [124]. In MPO, the A, B, C and D rings are bridged by four faces referred to as the  $\alpha$ -heme edge between ring A and B,  $\beta$ -heme edge between ring B and C,  $\gamma$ -heme edge between ring C and D, and  $\delta$ -heme edge between ring D and back to the A ring. The  $\delta$ -meso-azidoheme adduct at this site is a result of solvent accessibility of the substrate to the distal heme cavity on peroxidases [125]. Our studies here (Figure 2.2A) confirm that this inhibition of MPO by  $NaN_3$  is reversible and the interaction of 4-ABAH with MPO was covalent, both under conditions lacking  $H_2O_2$ . Furthermore, one step we observed for 4-ABAH inhibition of Compound I corresponds presumably to the slow binding step or covalent modification of the MPO protein is lost upon exhaustive dialysis (Figure 2.4). It should be emphasized that if modification of MPO active site were competitive or non-covalent there would be release of the weaker binding compound overtime by this equilibrium dialysis, essentially returning the MPO to its native state. Interestingly, this step of potential high affinity interaction or covalent modification is markedly absent in the other compounds tested with the exception of 2-ABAH, indicating that a like mechanism may occur.

Our report is not the first to study inhibition of peroxidases by hydrazide containing

compounds as it has been described for MPO and others peroxidase, such as horseradish peroxidase by alkyl hydrazine [126, 127] and phenylhydrazine [126, 127]; not to mention, microperoxidase-11 by 4-ABAH [128]. To evaluate this phenomenon further, we also wanted to validate that ADHP was accurately reporting on catalytic events within the active site. To do this we examined the relationship between the overall inhibitory rate constants, namely  $K_i$ , for the *meta*- and *para*-substituted compounds used here with respect to the appropriate Hammett coefficients ( $\sigma$ ) (Figure 2.5A). Given this linear relationship of this plot and high degree of correlation, it is likely that the same general mechanism is operating throughout the series [129]. Keeping in mind that a positive value of  $\sigma$  indicates an electron-withdrawing group and a negative value an electron-donating group, so  $-\text{CF}_3$  substitution would have an overall withdrawing function with a  $\sigma$  value of  $+0.54$  and be contrasted by the  $-\text{NH}_2$  substitution that carries a  $\sigma$  value of  $-0.66$ . Further examination of the dependency of the  $\sigma$  value with respect to the phenomenological  $\text{IC}_{50}$  values (Figure 2.5B) showed a similar but less precise relationship was indicated. Under our conditions there was extremely weak correlation between the inhibitor constants and the hydrophobicity of the substituent added (Figure 2.5C). It should be noted that due to limitations of the Hammett's coefficient interpretations, the 2-ABAH could not be examined in this way due to the *ortho*-effects resulting in potential interference between the moieties [129]. Taken together, there was clear evidence that use of ADHP oxidation is a powerful approach to study inhibitory aspects related to targeting MPO function and our handling of the batch data was appropriate given the high correlation of the Hammett plots (Figure 2.5A).

Spurred on by our findings that there was two distinct observable kinetic events occurring in 4-ABAH-mediated inhibition of Compound I, we decided to better understand the nature of

inhibition for the simple un-substituted BAH, as a means to ascribe one step to a physical event. Our initial hypothesis was that the heme b was being destroyed as was reported for potential carbene Fe-porphyrin complex described for cytochrome P450 [130] and more recently for H<sub>2</sub>O<sub>2</sub>-oxidative inhibition of MPO [117]. It is speculated that a phenol radical would add to the heme and cause a rearrangement that would free the Fe molecule, similar to the inactivation of myoglobin with phenylhydrazine. Contrary to this, we observed no evidence that Fe was released and that the heme b group was being destroyed. Moreover, Figure 2.6 showed convincingly that there is a LC-heme b band that remained active towards the luminol-based chemiluminescence substrate. This cleavage event could partially explain the problem in obtaining a structure of MPO with BAH, given BAH-mediated inhibition showed a release of heme b group, adding significant disorder to the forming unit cell due to a conversion of the covalent linked ester into an equilibrium interaction. One simple analogy would be that overtime the BAH essentially promotes ejection of the heme b payload from the peroxidase into the surrounding environment. To prove that the LC-heme b inhibition product was indeed formed, we setup two parallel and independent experiments to determine the actual mass of the LC-heme b reaction product. To confirm that this ester hydrolysis mechanism was broadly used by other BAH analog we also showed that 4-TFMBAH was capable of generating the similar reaction products (Supplementary Figure 2.1), though at a slightly altered concentration profile suggesting that there maybe potential in the future to modulate hydrolysis of the MPO ester bonds based on chemical properties of the modifications to the BAH platform. Our UV-Vis spectroscopic data (Figure 2.7C) also demonstrated the loss of the sulfonium ion linkage between <sup>HC</sup>Met<sup>243</sup> and the pyrrole A ring, which would be necessary to have the LC-heme b moiety release from the HC of MPO.

It should be emphasized that simplification of the overall number of parameters has aided in the overall evaluation of these inhibitors tested here and conditions will be examined in the future as layers of complexity are added (e.g. increasing the pH to more neutral conditions and addition of  $\text{Cl}^-$  ions to the system). Studies will also be necessary to expand the structure and activity relationship to analogous compounds to those tested to gain a greater understanding of the constraints of the MPO active site environment and the chemical influence analogous substitution have on MPO ester hydrolysis in the presence of  $\text{H}_2\text{O}_2$ . It is our contention that application of this new methodology (i.e. use of ADHP) will aid in rapid assessment of the MPO peroxidase function making high throughput screening possible and leading to rationale design application of inhibitors targeting MPO specifically. Furthermore, our observation here that BAH promotes the release of the heme b from the active site of MPO through cleavage of the ester linkages is novel and may promote a better understanding of the mechanism of action of this widely used inhibitor.

**Table 2.1 Discrimination analysis of two models for inhibition of MPO activity by the given compounds using DynaFit 3.**

The most plausible model is one with the highest Akaike weight. Columns represent residual sum of squares (RSS), the change in Akaike's information criterion ( $\Delta\text{AICc}$ ) and the resulting overall discriminatory Akaike weight.

Inhibitor	Model	$\Delta\text{AICc}$	Weight
2-ABAH	1 step	8.9	0.01127
	<b>2 step</b>	0	0.98873
4-ABAH	1 step	6.9	0.03093
	<b>2 step</b>	0	0.96907
3-DMABAH	<b>1 step</b>	0	0.88393
	2 step	4.1	0.11607
BAH	<b>1 step</b>	0	0.99685
	2 step	11.5	0.00315
4-FBAH	<b>1 step</b>	0	0.9196
	2 step	4.9	0.0804
NaN <sub>3</sub>	<b>1 step</b>	0	0.88144
	2 step	4.0	0.11856
4-TFMBAH	<b>1 step</b>	0	0.90896
	2 step	4.6	0.09104
4-NBAH	<b>1 step</b>	0	0.82051
	2 step	3.0	0.17949
Isoniazid	<b>1 step</b>	0	0.88569
	2 step	4.1	0.11431

**Table 2.2 Inhibitory efficiencies of hydrazide analogs on MPO activity.**

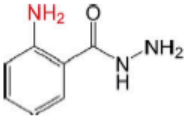
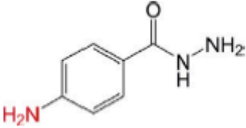
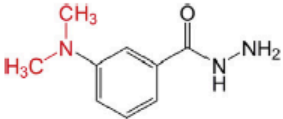
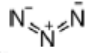
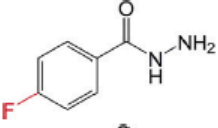
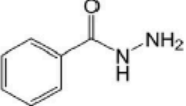
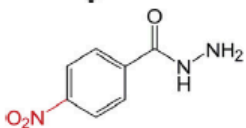
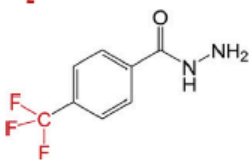
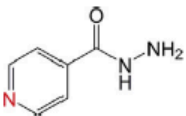
As measured in the MPO fluorescence stopped flow assay and simultaneous fit with either a 1 or 2-step slow tight-binding mechanism using DynaFit 3. Fixed constants  $k_{+1}=10 \mu\text{M}^{-1}\text{s}^{-1}$ ,  $k_{-1}=80 \text{ s}^{-1}$ ,  $k_{+2}=224 \text{ s}^{-1}$ .

Inhibitors	$k_{+3} (\mu\text{M}^{-1}\text{s}^{-1})$	$k_{-3} (\text{s}^{-1})$	$k_{+4} (\text{s}^{-1})$	$k_{-4} (\text{s}^{-1})$	$K_i (\mu\text{M})$	$K_i^* (\mu\text{M})$
2-ABAH	$0.10 \pm 0.0014$	$0.026 \pm 0.0003$	$0.0067 \pm 0.0004$	$0.0094 \pm 0.002$	0.26	0.16
4-ABAH	$0.13 \pm 0.0007$	$0.031 \pm 0.0001$	$0.038 \pm 0.003$	$0.73 \pm 0.06$	0.24	0.23
3-DMABAH	$0.09 \pm 0.0009$	$0.05 \pm 0.0005$	-	-	0.56	-
BAH	$0.0098 \pm 5.47\text{E-}05$	$0.0068 \pm 9.5\text{E-}05$	-	-	0.69	-
4-FBAH	$0.0075 \pm 4.93\text{E-}05$	$0.0062 \pm 0.0001$	-	-	0.83	-
NaN <sub>3</sub>	$0.185 \pm 0.0018$	$0.156 \pm 0.001$	-	-	0.84	-
4-TFMBAH	$0.0013 \pm 1.36\text{E-}05$	$0.004 \pm 0.0002$	-	-	3.08	-
4-NBAH	$0.0027 \pm 1.65\text{E-}05$	$0.01 \pm 0.0001$	-	-	3.70	-
Isoniazid	$0.0011 \pm 7.31\text{E-}06$	$0.011 \pm 0.0001$	-	-	10.00	-



**Table 2.3 Profile of IC<sub>50</sub> values for MPO inhibition.**

Inhibition of MPO activity (%) was determined from progress curves for resorufin generation by mixtures of MPO (23 nM) with ADHP (40 μM) initiated with H<sub>2</sub>O<sub>2</sub> (22 μM) in the presence of varied concentrations of 2-ABAH, 4-ABAH, 3-DMABH, NaN<sub>3</sub>, 4-FBAH, BAH, 4-NBAH, 4-TFMBH and Isoniazid. Columns presented are abbreviate compound names (inhibitor), compound structure with varied R groups shown in red, and 50% inhibitory concentration with standard error of the mean (IC<sub>50</sub> ± SEM). Data was analyzed as described under “Experimental Procedures.”

Inhibitor	Structure	IC <sub>50</sub> ± SEM (μM)
2-ABAH		0.50 ± 0.03
4-ABAH		0.71 ± 0.01
3-DMABAH		1.27 ± 0.07
NaN <sup>3</sup>		6.57 ± 0.32
4-FBAH		22.45 ± 2.19
BAH		40.83 ± 4.00
4-NBAH		54.62 ± 14.06
4-TFMBAH		142.70 ± 10.98
Isoniazid		277.10 ± 6.65

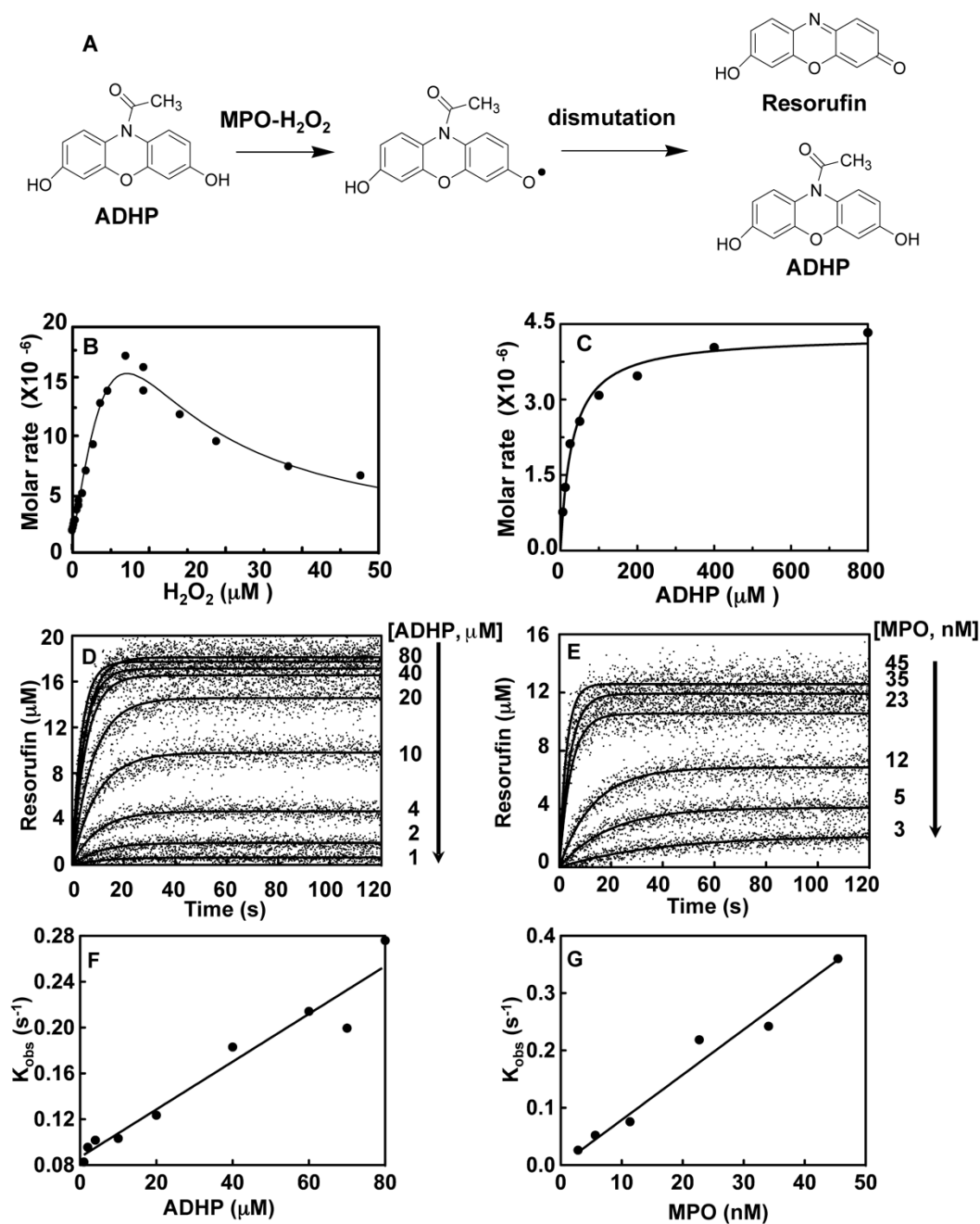


**Figure 2.1** Characterization of the ADHP oxidation by MPO-H<sub>2</sub>O<sub>2</sub> complex.

*A*, General mechanism of ADHP oxidation to resorufin by a proposed two step reaction, whereby the MPO-H<sub>2</sub>O<sub>2</sub> complex generates two ADHP radicals that undergo a subsequent enzyme independent dismutation reaction to complete formation of one resorufin and one ADHP molecule. *B*, The H<sub>2</sub>O<sub>2</sub> dependency for ADHP oxidation by Compound I assessed by initial rates

of fluorescence change. Reactions of MPO (2.8 nM) and ADHP (20  $\mu\text{M}$ ) were initiated by different concentrations of  $\text{H}_2\text{O}_2$ . *C*, Michaelis-Menten plot of initial rates versus given ADHP concentrations, progress curves of ADHP oxidation to resorufin generated by MPO- $\text{H}_2\text{O}_2$  complex over ADHP concentrations ranging from 6.25, 12.5, 25, 50, 100, 200, 400, and 800  $\mu\text{M}$ . Reactions of MPO (23 nM) and given ADHP concentrations were initiated by  $\text{H}_2\text{O}_2$  (22  $\mu\text{M}$ ) auto-injection. *D*, Stopped-flow progress curves of resorufin generation by MPO (23 nM) initiated by addition of  $\text{H}_2\text{O}_2$  (22  $\mu\text{M}$ ) for a series of given ADHP concentrations. *E*, the original fluorescence data was converted into produced resorufin and a set of produced resorufin progress curves was fitted to one phase exponential function using the non-linear regression. Observed rate constant ( $K_{\text{obs}}$ ) increases with increasing concentration of ADHP in Panel F and MPO- $\text{H}_2\text{O}_2$  complex in Panel G. Determination of apparent first order rate constant from the slope of  $K_{\text{obs}}$  as a function of ADHP concentrations. Single exponential function was used to obtain the observed rate constant ( $K_{\text{obs}}$ ). Titrations were performed and analyzed as described under “Experimental Procedures.”

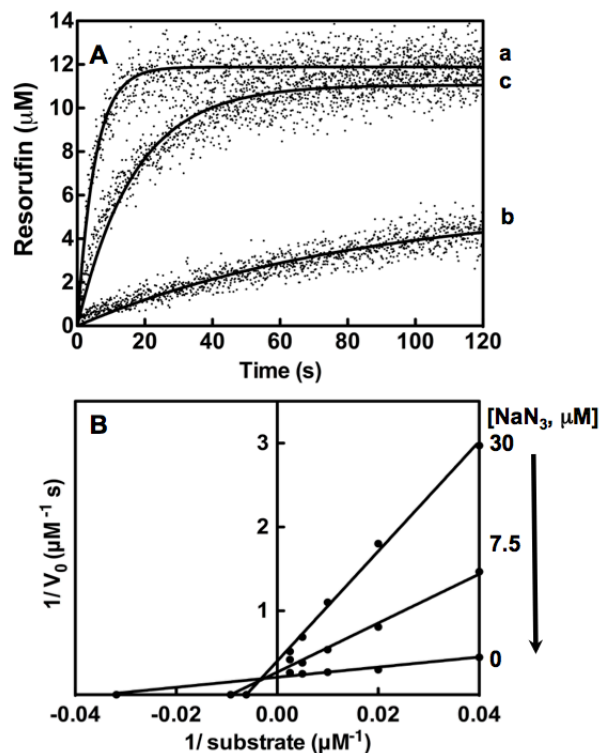


**Figure 2.2** NaN<sub>3</sub> inhibition of Compound I.

A, Stopped flow analysis of MPO (23 nM) without inhibitor (a), in the presence of NaN<sub>3</sub> (30 μM) after pre-incubation for 1 hr prior to triggering H<sub>2</sub>O<sub>2</sub> addition (b) and after equilibrium dialysis (c). B, Lineweaver-Burk plots of for NaN<sub>3</sub> inhibition on MPO calculated from resorufin production data. Titrations of 0, 7.5, 30 μM NaN<sub>3</sub> are shown for the different concentration of ADHP from 25, 50, 100, 200 and 400 μM. Titrations were performed and analyzed as described under “Experimental Procedures.”

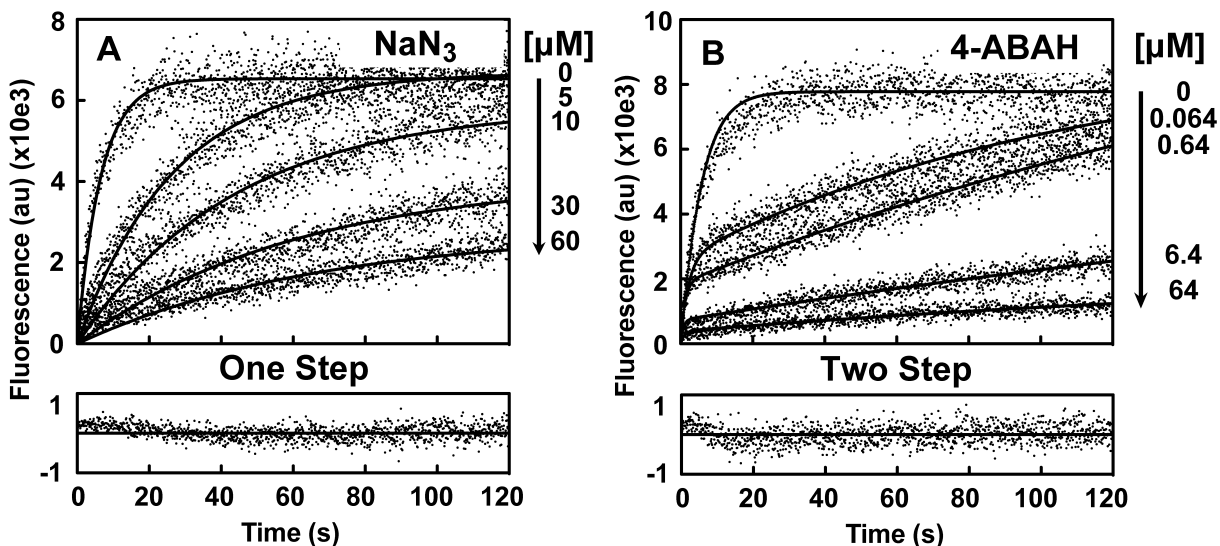


**Figure 2.3 Comparison of Compound I inhibition by NaN<sub>3</sub> and 4-ABAHA using simultaneous reaction modeling.**

*A*, Fluorescence progress curves presented in arbitrary units (au) for various indicated concentration of NaN<sub>3</sub> were globally fit to a one-step slow-tight binding model detailed in Scheme I. Representative goodness-of-fit for the 30 μM ABAHA with 15 μM ADHP reaction is shown as a residual plot. *B*, Similar plots for 4-ABAHA analyzed by a two-step slow-tight binding model (Scheme II) for indicated concentrations of 4-ABAHA to accommodate the bi-phasic phenotypic of the reaction. Representative goodness-of-fit for 0.64 μM ABAHA with 16 μM ADHP are also shown. Titrations were performed and analyzed as described under “Experimental Procedures.”

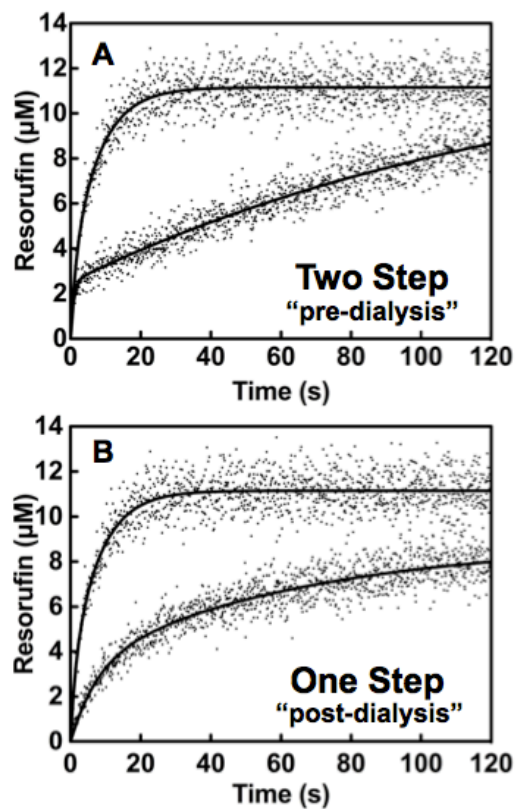


**Figure 2.4 Reversibility of 4-ABAH-mediated MPO inhibition.**

*A*, Stopped flow analysis of MPO (23 nM) and ABAH were mixed and incubated in assay buffer for 1 hr prior to triggering  $H_2O_2$  addition. *B*, Exhaustive dialysis of identical mixtures into assay buffer followed addition with  $H_2O_2$ . Titrations were performed and analyzed as described under “Experimental Procedures.”

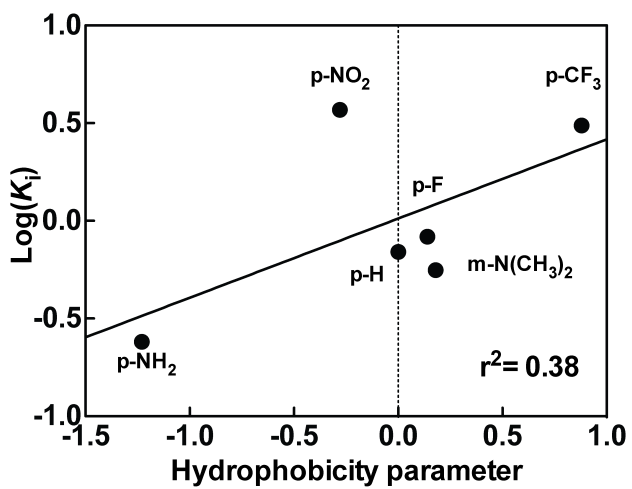
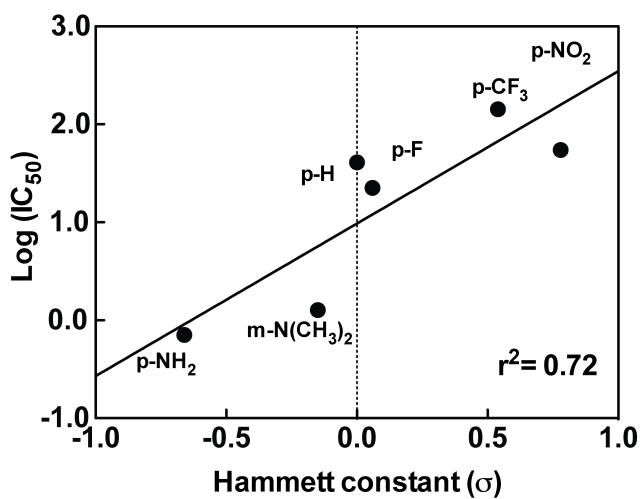
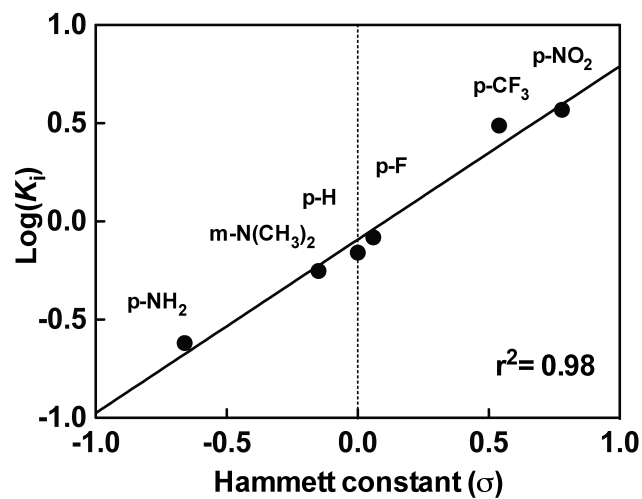


**Figure 2.5 Linear free-energy relationship of substituted benzoic acid hydrazide compounds tested on inactivation of Compound I.**

*A*, Correlation of the log of overall inhibitory rate constant ( $K_i$ ) for the compounds tested with their respective Hammett's constants ( $\sigma$ ). A positive value of  $\sigma$  indicates electron-withdrawing group and a negative value an electron-donating group. *B*, Correlation of the log of the half maximal inhibitory concentration ( $IC_{50}$ ) versus  $\sigma$ . *C*, Correlation of  $\text{Log}(K_i)$  versus hydrophobicity parameters. Titrations were performed and analyzed as described under "Experimental Procedures."



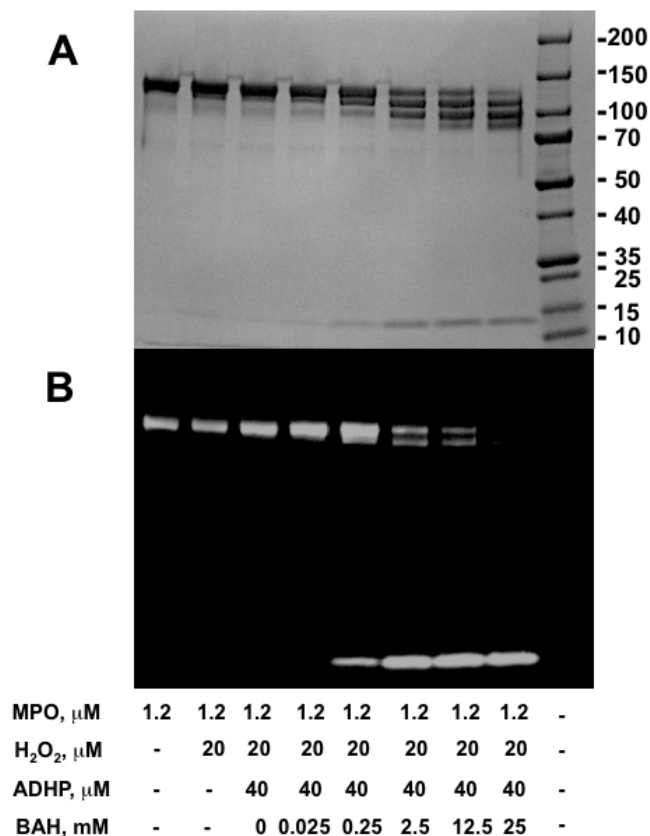


**Figure 2.6 Benzoic acid hydrazide-mediated cleavage of MPO active site heme.**

*A-B*, MPO (1.2  $\mu\text{M}$ ), ADHP (40  $\mu\text{M}$ ) with different concentrations of BAH inhibitor (0, 0.025, 0.25, 2.5, 12.5 and 25 mM) were incubated with H<sub>2</sub>O<sub>2</sub> (20  $\mu\text{M}$ ) at room temperature for 10 min. Samples of 20  $\mu\text{L}$  were added to non-reducing sample loading buffers, and then loaded without prior heating and resolved by 4-15% gradient SDS-polyacrylamide gel electrophoresis. Concentration dependence of BAH-mediated cleavage of heme moiety freeing the MPO light chain shown by SDS gel for protein (panel A) and by chemiluminescence (panel B). Note the progressive oxidative cleavage of the MPO protein marked by loss of one and then both of the MPO light chains (~14kD). The active site heme is attach to light chain as evident by the chemiluminescence band.

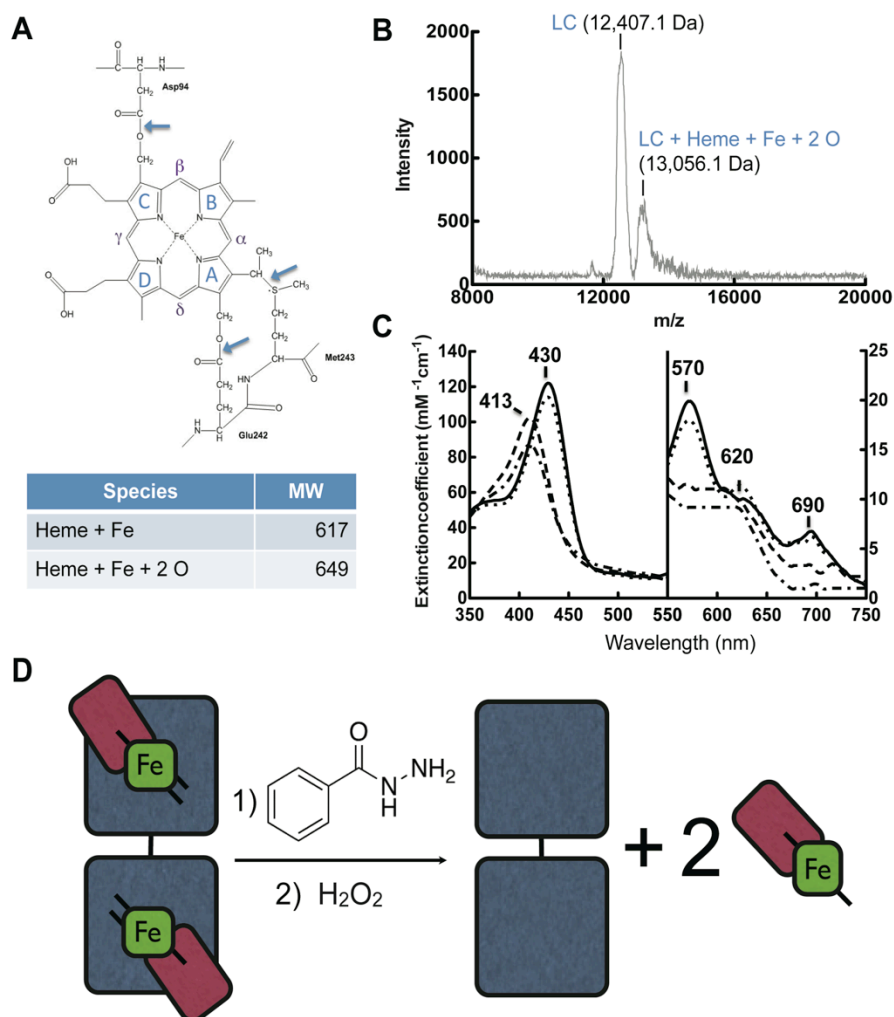
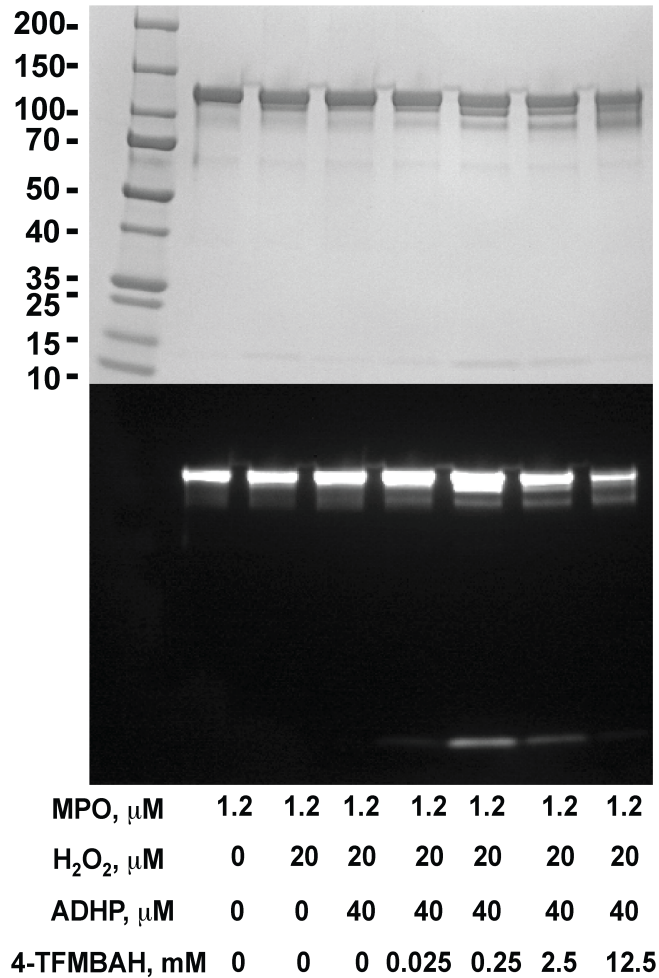


**Figure 2.7 Sequential hydrolysis of ester bonds results in cleavage of the catalytic heme from MPO active site.**

*A*, Structure and nomenclature of the tetrapyrrole ring of the heme in the MPO active site.

Figure adapted from (Kooter IM, 1999). *B*, Maldi-TOF mass spectroscopy analysis of reactions under conditions that maximize light chain-heme product formation, namely MPO (1.2  $\mu\text{M}$ ) with BAH (2.5 mM) pre-incubated for 10 min prior to the addition of  $\text{H}_2\text{O}_2$  (20  $\mu\text{M}$ ). These reactions

are identical to those in lane 6 in Figure 2.6. *C*, Spectroscopic analysis of MPO heme signature following addition of BAH. Curves represent MPO (black line), MPO with hydrazide (dotted), MPO with hydrazide post H<sub>2</sub>O<sub>2</sub> addition after 10 min (dashed) and again after 1hr (dot-dashed). *D*, Schematic representation of the release of the active site heme from MPO by reaction with BAH and H<sub>2</sub>O<sub>2</sub>. MPO subunits are shown as light chain (red), heme (green) and heavy chain (gray).



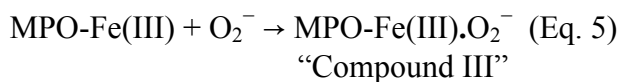
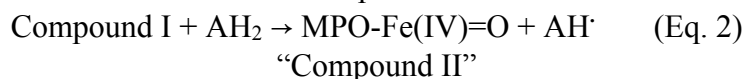
**Supplemental Figure 2.1 4-(trifluoromethyl) benzoic acid hydrazide-mediated cleavage of MPO active site heme.**

*A-B*, MPO (1.2  $\mu\text{M}$ ), ADHP (40  $\mu\text{M}$ ) with different concentrations of 4-TFMBAH inhibitor (0, 0.025, 0.25, 2.5, 12.5 and 25 mM) were incubated with H<sub>2</sub>O<sub>2</sub> (20  $\mu\text{M}$ ) at room temperature for 10 min. Samples of 20  $\mu\text{L}$  were added to non-reducing sample loading buffers, and then loaded without prior heating and resolved by 4-15% gradient SDS-polyacrylamide gel electrophoresis. Concentration dependence of 4-TFMBAH-mediated cleavage of heme moiety freeing the MPO light chain shown by SDS gel for protein (panel A) and by chemiluminescence (panel B).

## Chapter 3 Inactivation of myeloperoxidase by benzoic acid hydrazide

### 3.1 Introduction

Myeloperoxidase (MPO) is a heme-dependent peroxidase, but it is the only one capable of consuming hydrogen peroxide ( $\text{H}_2\text{O}_2$ ) to mediate chloride oxidation to hypochlorous acid (HOCl). In its resting state, MPO contains ferric heme (MPO-Fe(III)). Upon reaction with  $\text{H}_2\text{O}_2$  the MPO heme is oxidized to a short-lived intermediate termed Compound I (half life  $\sim 100$  ms; [94]), which contains a ferryl porphyrin  $\pi$  cation radical (MPO-Fe(IV)=O $^{\cdot+\pi}$ ) (Eq. 1) [95, 131]. In the absence of  $\text{Cl}^-$  and in the presence of classical peroxide electron donor ( $\text{AH}_2$ ), MPO follows a typical peroxidase catalytic cycle where Compound I is reduced back to the ferric state in two sequential one-electron steps (Eq. 2-3). In the first of these, the porphyrin radical is reduced leaving a ferryl heme known as Compound II (Eq. 2). A second equivalent of  $\text{AH}_2$  then reduces Compound II to ferric enzyme (Eq. 3). In the process two equivalents of electron donor are oxidized to the corresponding free radical product ( $\text{AH}^\cdot$ ) [92, 93].



In the presence of Cl<sup>-</sup>, MPO Compound I is uniquely able to oxidize Cl<sup>-</sup> to HOCl, and in the process Compound I is reduced directly to the ferric state (Eq. 4). Neither Compound II (Eq. 3) nor superoxide-inactivated Compound III (Eq. 5) participates in Cl<sup>-</sup> oxidation. These reactions (Eq. 1-5) occur through octahedral coordination of the active site Fe by the protoporphyrin IX heme and the proximal histidine 336 on the MPO heavy chain (<sup>HC</sup>His<sup>336</sup>).

MPO also auto-catalytically forms three covalent associations with the porphyrin macrocycle the sum of which is an arrangement found nowhere else in nature. An MPO light chain aspartate (<sup>LC</sup>Asp<sup>94</sup>) forms an ester with the methyl side chain of pyrrole C. Additionally, a heavy chain glutamate (<sup>HC</sup>Glu<sup>242</sup>) forms an ester with the methyl side chain of pyrrole A, and the immediately adjacent methionine (<sup>HC</sup>Met<sup>243</sup>) is involved in a vinyl-sulfonium linkage with pyrrole A [25]. Interestingly, these bonds establish, through the prosthetic group itself, a covalent link between MPO's light and heavy chains and may account for the distinct saddling observed in the MPO heme. The extent of covalent association between mammalian peroxidases and their heme varies. It is completely absent in all non-animal peroxidases including horseradish peroxidase (HRP) [29, 132, 133], lignin peroxidase [134], bacterial catalase-peroxidases (KatG) [135, 136], and ascorbate peroxidase [137], indicating that this type of heme modification is not required for classical peroxidase activity. However, mammalian peroxidases like lactoperoxidase (LPO) have two ester linkages analogous to those observed in MPO but lack the vinyl-sulfonium adduct [138, 139]. In LPO, the ester bonds are between the heme b and its single subunit via <sup>LPO</sup>Glu<sup>375</sup> and <sup>LPO</sup>Asp<sup>225</sup> to pyrrole rings A and C, respectively. It is thought that the covalent tethers between mammalian peroxidases and their heme cofactors afford them a certain level of resistance necessary to protect the heme from oxidation by the HOCl and HOBr, which they generate [29].

Recently, we reported that incubation of benzoic acid hydrazide (BAH) with MPO in the presence of H<sub>2</sub>O<sub>2</sub> causes a disruption of the linkages that occurred between the heme b and MPO heterodimer subunits [28]. Analysis of H<sub>2</sub>O<sub>2</sub>/BAH-treated MPO by SDS-PAGE revealed the co-migration of heme with the LC, suggesting that cleavage of the <sup>HC</sup>Glu<sup>242</sup> ester and vinyl-<sup>HC</sup>Met<sup>243</sup> sulfonium preceded loss of the <sup>LC</sup>Asp<sup>94</sup> ester bond. Indeed, H<sub>2</sub>O<sub>2</sub>/BAH- induced shifts in heme absorption were also consistent with the disruption of its vinyl-sulfonium linkage [28]. The molecular mechanism by which this cleavage takes place and the role of this cleavage in the inhibition of MPO remains to be elucidated. There also has been no study to our knowledge that reports correlation between the MPO heme liberation with any other inhibitors that did not involve concomitant Fe loss. A panel of BAH analogs were used here to probe structure and function (i.e. cleavage) relationship to better understand the underlying mechanism by which the disruption occurs. Furthermore, we tracked how a Cy5-hydrazide inhibitor was incorporated into the MPO protein to determine a key event in the reaction mechanism that should parallel the BAH analog mechanism of MPO inhibition. Using peptide mass mapping, we also identified three MPO lysine (Lys) residues (<sup>HC</sup>Lys<sup>138</sup>, <sup>HC</sup>Lys<sup>308</sup>, and <sup>HC</sup>Lys<sup>463</sup>) where benzoic acid radical form adducts following oxidation by Compound I. Additionally, we found a number of methionine (Met) residues (<sup>LC</sup>Met<sup>85</sup>, <sup>LC</sup>Met<sup>87</sup>, <sup>HC</sup>Met<sup>243</sup>, <sup>HC</sup>Met<sup>249</sup>, <sup>HC</sup>Met<sup>306</sup>, and <sup>HC</sup>Met<sup>385</sup>) that were differentially oxidized in the presence of BAH with a relatively low concentration of H<sub>2</sub>O<sub>2</sub> compared to the native MPO protein. Oxidation of <sup>HC</sup>Met<sup>243</sup>, in particular, may be a direct result of inhibition by BAH but further studies are needed to refine the exact chemical reactions leading to release of the heme from the HC of MPO. Finally, we tested whether BAH could be used to liberate the heme b prosthetic group from the active site of the analogous ester linkages present in LPO. Taken together, these studies provide new insight into the molecular mechanism

of MPO inhibition by BAH providing new avenues for future drug discovery efforts that aims to limit the production of peroxidase-derived oxidants in chronic inflammatory diseases [140].

## **3.2 Materials and methods**

### **3.2.1 Materials**

Ultra-pure myeloperoxidase (MPO) purified from human neutrophils was obtained from Lee Biosolutions Inc. (St. Louis, MO) and lactoperoxidase (LPO) of bovine and superoxide dismutase (SOD) were purchased from Worthington Biochemical Corporation (Lakewood, NJ). 4-aminobenzoic acid hydrazide (4-ABAH), benzoic acid hydrazide (BAH), 4-fluorobenzoic acid hydrazide (4-FBAH), 4-nitrobenzoic acid hydrazide (4-NBAH), sodium azide ( $\text{NaN}_3$ ), Dimethyl sulphoxide (DMSO) from Alfa Aesar (Ward Hill, MA). Cyanine5 (Cy5) hydrazide was purchased from Lumiprobe Corporation (Hallandale Beach, FL).  $\text{H}_2\text{O}_2$ , glutathione (GSH), 2-aminobenzoic acid hydrazide (2-ABAH), 4-(trifluoromethyl) benzoic acid hydrazide (4-TFMBAH), 3-(dimethylamino) benzoic acid hydrazide (3-DMABAH) were purchased from Sigma-Aldrich (St. Louis, MO, USA). Fetal bovine serum were purchased from Innovative Research Inc. (Novi, MI). For protein staining, Gelcode Blue was purchased from Pierce (Rochford, IL), with tracking of the heme prosthetic group accomplished by use of the chemiluminescent Western Lightning ultra-reagent from PerkinElmer Inc. (Waltham, MA).

The acetate assay buffer was prepared to pH 5.6 by adjusting the pH of the sodium acetate with acetic acid. All working solutions of  $\text{H}_2\text{O}_2$  were prepared fresh daily by diluting 30%  $\text{H}_2\text{O}_2$  (BDH Chemicals, London, UK) and measuring the  $\text{H}_2\text{O}_2$  concentration using the extinction coefficient for  $\text{H}_2\text{O}_2$  at 240 nm of  $39.4 \text{ M}^{-1} \text{ cm}^{-1}$  [117, 141]. Cy5-hydrazide, 4-ABAH, 2-ABAH, BAH, 4-FBAH, 4-NBAH, 4-TFMBAH, 3-DMABAH,  $\text{NaN}_3$  and isoniazid were dissolved in DMSO and subsequently diluted into acetate buffer. MEBSS buffer (144 mM NaCl, 5.4 mM



KCl, 800  $\mu$ M MgSO<sub>4</sub>, 800  $\mu$ M NaH<sub>2</sub>PO<sub>4</sub>, 1.2 mM CaCl<sub>2</sub>, 5.6 mM glucose, 4 mM Hepes, pH 7.4 with 1% fetal bovine serum) was used in the luminescence assay for MPO activity, in accordance with the literature [67].

### 3.2.2 SDS-PAGE analysis of (heme b)-LC generation

To determine the effect that BAH analogs and the fluorescent analog Cy5-hydrazide have on the heme catalytic ability of MPO, MPO (1.2  $\mu$ M) was incubated at room temperature with different BAH analogs following addition of H<sub>2</sub>O<sub>2</sub> (20  $\mu$ M). These samples of 20  $\mu$ L were added to non-reducing sample loading buffer (Bio-rad), and loaded without prior heating onto a 4-15% gradient SDS-polyacrylamide gel electrophoresis (SDS-PAGE). Of note, heat treatment was avoided to minimize the autocatalytic cleavage of MPO heavy chain at <sup>HC</sup>Met<sup>243</sup>-<sup>HC</sup>Pro<sup>244</sup> bond that results in 39 kDa and 20 kDa bands [112]. Protein staining of elaborated gels was performed by GelCode Blue reagent (Pierce) followed by probing of the gel for the movement of the heme b through topical application of Western Lightning reagent (PerkinElmer Inc.). The light production generated as a result of this chemiluminescence reaction was collected using a Fujifilm LAS-1000 luminescence imager. For reactions examining incorporation of Cy5-hydrazide, an additional fluorescence scan was performed with fluorescent-labeled protein bands detected with a FLA-5100 imager with the 670 nm far-red laser and the Cy5 filter set (Fujifilm Inc., Tokyo, Japan). These scans were performed using excitation at  $\lambda_{640\text{ nm}}$  and emission at  $\lambda_{670\text{ nm}}$ . Total protein staining was done with Gelcode Blue reagent and imaged with Bio-Rad Gel Doc imager using Quantity One version 4.6.9. The luminescence signal of the gel was quantified using ImageJ 64 software (National Institutes of Health, Maryland, USA).

### 3.2.3 MPO fluorescence assay

MPO peroxidase activity was measured by monitoring the formation of resorufin from the oxidation of 10-acetyl-3,7-dihydroxyphenoxazine (ADHP) by MPO. This assay was used to determine whether SDS in loading buffer could diminish MPO activity for the gel analysis. Reaction of ADHP (20  $\mu\text{M}$ ) and MPO (28 nM) were incubated with or without 2% SDS in acetate assay buffer for 5 mins and initiated by the addition of  $\text{H}_2\text{O}_2$  (40  $\mu\text{M}$ ) by use of Varioskan Flash plate reader with excitation of  $\lambda_{530\text{nm}}$  and emission of  $\lambda_{590\text{nm}}$ . SkanIt software 2.4.3 parameters included an interval of 0.1 s for each of 1000 reads.

### **3.2.4 MPO activity kinetics**

To evaluate the inhibitory effect of Cy5-hydrazide on the peroxidase activity of MPO, a luminescence assay was performed with luminol as the peroxidase substrate. In reactions of 200  $\mu\text{L}$  total volume, MPO (140 nM) was incubated with the luminol substrate (400  $\mu\text{M}$ ) in MEBSS buffer for a series of Cy5-hydrazide concentrations for 5 mins before triggering the reaction by the addition of  $\text{H}_2\text{O}_2$  (20  $\mu\text{M}$ ). Dispensing of  $\text{H}_2\text{O}_2$  was done using the auto-injection function of the Varioskan plate reader controlled by the SkanIt software version 2.4.3. Measurements were taken at 1 s intervals over 2 mins. The inhibitory rate constant for the reaction was not determined due to the inherent difficulty of relating these observed luminescence progress curves to molar product formed, instead apparent  $\text{IC}_{50}$  values for Cy5-hydrazide were determined based on using the curve amplitude and converting that to the percentage of total inhibition of MPO peroxidase activity at a given Cy5-hydrazide concentration using Prism software (GraphPad Software, Inc., La Jolla, CA).

### **3.2.5 Mass spectrometric analysis**

To determine the BAH-induced MPO modification, we performed a peptide mass fingerprinting (PMF) experiment using mass spectrometry. The analyzed reactions consisted of

MPO alone and MPO with H<sub>2</sub>O<sub>2</sub> in the presence of BAH. These reactions were subjected to tryptic digestion and peptide mapping at Creative Proteomics Inc. (New York, NY). Side-by-side reactions for identical samples of MPO (1.2 μM) with and without H<sub>2</sub>O<sub>2</sub> (40 μM) and BAH (5 mM) in a total of 50 μL and further diluted with 50 μL of 100 mM Tris-HCl (pH 8.5). Then protein disulfide bonds of the diluted sample were reduced for 40 min with 5 mM dithiothreitol at room temperature and alkylated for 40 min with 15 mM iodoacetamide in the dark. The alkylated protein samples were digested overnight at 37°C with sequencing-grade trypsin (Promega Corp., Madison, WI) in a 1:50 enzyme-to-substrate ratio. Following digestion, the peptide mixtures were acidified with trifluoroacetic acid (TFA) to a final concentration of 1% TFA, and desalted by filter-aided sample preparation (FASP) method [142]. Finally, the desalted peptide samples were dried in a vacuum concentrator and these products were analyzed by nanoLC-MS/MS. For LC-MS/MS analysis of the dried tryptic peptides were dissolved in 10 μL of 0.1% formic acid in water and subjected to Easy-nLC1000 nano-flow UPLC-System (Thermo Fisher Scientific, Dionex Co., CA). The nanoLC separation was accomplished by a four-step gradient from 0.1% formic acid in H<sub>2</sub>O to 0.1% formic acid in acetonitrile. The Q Exactive hybrid quadrupole-Orbitrap mass spectrometer (ThermoFisher Scientific, USA) was used to analyze the peptide mixture; raw MS/MS data was analyzed by using MaxQuant version 1.4.1.2 (Max Planck Institute of Biochemistry, Martinsried, Germany). Replicative LC-MS/MS acquisitions and analysis were performed to maximize modification sites identification.

### **3.3 Results**

#### **3.3.1 MPO cleavage by H<sub>2</sub>O<sub>2</sub>/BAH versus H<sub>2</sub>O<sub>2</sub> alone**

To compare the cleavage products of MPO by BAH, separate reactions were assessed for changes in banding patterns and through tracking the migration of the heme b prosthetic group.

Reactions of MPO (1.2  $\mu\text{M}$ ) with BAH (2.5 mM, lane 2) in the presence of increasing concentrations of  $\text{H}_2\text{O}_2$ , namely 8  $\mu\text{M}$  (lane 3), 40  $\mu\text{M}$  (lane 4), 80  $\mu\text{M}$  (lane 5), 160  $\mu\text{M}$  (lane 6), 800  $\mu\text{M}$  (lane 7) and 8 mM (lane 8) for 10 min (Figure 3.1A and 3.1B) were compared to similar reactions without BAH (Figure 3.1C and 3.1D). As shown in Figure 3.1A and 3.1B, the formation of the (heme b)-LC cleavage product was increased as we increased the concentration of  $\text{H}_2\text{O}_2$  from 8  $\mu\text{M}$  to 160  $\mu\text{M}$ . In contrast, treatment of MPO with higher concentrations of  $\text{H}_2\text{O}_2$  alone (Figure 3.1C and 3.1D) showed that the inactivation of MPO by higher concentration of  $\text{H}_2\text{O}_2$  (800 $\mu\text{M}$  and 8 mM) caused destruction of the heme group as demonstrated by the lack of a functional (heme b)-LC reaction product. Our results agree with the literature observation that incubation of MPO with high relative concentrations of  $\text{H}_2\text{O}_2$  would cause loss of the active site Fe atom [117].

### 3.3.2 Screening of BAH analogs for generation of the (heme b)-LC reaction product

We recently reported the inhibition of MPO by BAH and several of its analogs, determining  $\text{IC}_{50}$  values and inhibition constants ( $K_i$ ) for each one [28]. A table summarizing these data can be found in *Supplementary material* (Table. S3.1). In order to explore the impact of hydrazide structure on MPO cleavage, we compared whether BAH analogs can cleave MPO native protein, we investigated the effect of BAH analogs on the MPO protein using SDS-PAGE analysis and our aforementioned ability to track the heme activity. Initially, we assessed the extent of cleavage products generated at concentration equal to 5-fold of the  $\text{IC}_{50}$  values previously determined [28]. These results indicated that BAH was the most potent modification of this cleavage (data not shown). To determine the extent of cleavage possible, we did the following experiments. MPO was incubated with different BAH analogs at 4mM inhibitor concentration, namely, BAH, NBAH, TFMBAH, isoniazid, 2-ABAH, 4-ABAH, 3-DMABAH,

NaN<sub>3</sub>, and 4-FBAH in the presence of 20 μM H<sub>2</sub>O<sub>2</sub> for 1h. Based on general protein staining and heme-dependent luminescence (Figure 3.2A), we found several BAH analogs (i.e. 4-FBAH, BAH and 3-DMABAH) in reactions were cleaved MPO dimer into (heme b)-LC and the HC, but this cleavage product was not present in an appreciable amount with NaN<sub>3</sub> and isoniazid. In addition, we quantitated the amount of (heme b)-LC generated by densitometry and expressed these results as LC percentage cleavage shown in Figure 3.2B. The correlation between the LC cleavage percentages and Hammett constants of BAH analogs were plotted to illustrate the structural and functional cleavage effect of BAH on MPO. We found that three of these compounds, namely, BAH, 4-FBAH and 3-DMBAH incubation mediate the greatest MPO cleavage into the HC and the (heme b)-LC as shown in Figure 3.2C. These results indicate that the cleavage efficiency of BAH analogs were greatest when the Hammett constant is close to neutral.

### **3.3.3 The cleavage of MPO by BAH analogs is mediated by formation of Compound I**

We observed by general protein staining (Figure 3.3A) and heme-dependent chemiluminescence (Figure 3.3B) the concentration dependent cleavage of MPO by BAH. Notably, no exogenous H<sub>2</sub>O<sub>2</sub> was added to these reactions. To determine whether catalytic amounts of H<sub>2</sub>O<sub>2</sub> were being generated in these reactions, the same reactions were set up with reagents pre-incubated with catalase for 1 hr in prior to mixing. As shown in Figure 3.3C and 3.3D, pre-incubation with catalase showed no cleavage with increased BAH concentration. These results indicated that the cleavage of MPO into HC and the (heme b)-LC was dependent on H<sub>2</sub>O<sub>2</sub>, implying the participation of MPO Compound I in the process. This is consistent with previous reports showing that H<sub>2</sub>O<sub>2</sub> is required for the irreversible inactivation of MPO by 4-ABAH [96].

### 3.3.4 Inactivation of MPO by Cy5-hydrazide

For the tracking of the modification to the MPO subunits, it was necessary to include Cy5-hydrazide as a reporter of the underlying chemical reaction. Inhibition of MPO by Cy5-hydrazide was confirmed by its concentration-dependent decrease in luminol oxidation catalyzed by MPO/H<sub>2</sub>O<sub>2</sub> (Figure 3.4A). Typical reaction traces showed an initial increase in luminescence followed by a steady-state plateau and slow decay of the signal. Increasing concentrations of Cy5-hydrazide resulted in decreased initial rates and extents of luminol oxidation. An IC<sub>50</sub> (5.5 μM) for Cy5-hydrazide inhibition of MPO was calculated by plotting the maximum observed luminescence of each kinetic progression curve against Cy5-hydrazide concentration (Figure 3.4B). The data were fit to non-linear least squares function in GraphPad Prism software (GraphPad Software, Inc., La Jolla, CA).

### 3.3.5 Cleavage of MPO by Cy5-hydrazide

A possible consequence of BAH-dependent cleavage of (heme b)-LC from the parent MPO heterodimer is the covalent modification of the protein by the hydrazide. Given the observed inhibition of MPO by Cy5-hydrazide, we sought to use its fluorescent properties to determine whether the process resulted in MPO HC labeling. MPO treated with H<sub>2</sub>O<sub>2</sub> and increasing concentrations of Cy5-hydrazide was evaluated by SDS-PAGE by general protein staining to identify HC-LC cleavage (Figure 3.5A), fluorescence to detect Cy5-hydrazide (Figure 3.5B), and luminescence to detect protein-linked heme (Figure 3.5C). Cy5-hydrazide cleaved MPO dimer into the HC and (heme b)-LC in a manner similar to that seen for BAH, 4-FBAH and DMABAH. Three separated bands of heavy chains (2HC-2(heme b)-2LC dimer, 2HC-1(heme b)-1LC and 2 HC) were produced in reactions containing 5 mM Cy5-hydrazide (Figure 3.5A). Further, HC of MPO was labeled with Cy5-hydrazide in a concentration dependent

manner (Figure 3.5B). Finally, increasing Cy5-hydrazide concentration increased generation of (heme b)-LC (Figure 3.5C) consistent with Cy5-hydrazide labeling of the heavy chain. Furthermore, we found the bottom (heme b)-LC band was not modified by direct attachment of the Cy5 radical to the heme prosthetic group as the luminescence reactions still were occurring (Figure 3.5C). Of note, similar reactions employing fluorescein-hydrazide did not result in labeling of either chain of the MPO protein and did not generate the expected (heme b)-LC fragment (data not shown), presumably due its poor accessibility to the heme active site.

### **3.3.6 Time-dependent Labeling MPO by Cy5-hydrazide**

To determine the relative rates of Cy5-hydrazide labeling and protein cleavage events, we monitored the reaction of MPO with H<sub>2</sub>O<sub>2</sub> and 2.5 mM Cy5-hydrazide at 30 minute intervals for 4 hours. The time course was set up as individual reactions that were stagger-started. This allowed us to simultaneously quench the MPO activity by addition of the 2% SDS contained in the gel loading buffer. This experimental design was necessary as we were afraid that the addition of the aliquots from a single reaction into the catalase might not stop these reactions adequately. We were able to validate this quenching protocol by addition of 2% SDS into fluorescence ADHP assays for reactions of MPO and H<sub>2</sub>O<sub>2</sub>. Addition of the SDS completely inactivated the MPO-H<sub>2</sub>O<sub>2</sub> (data not shown). As in Figure 3.5, we evaluated SDS-PAGE separated reaction products by general protein staining, fluorescence, and luminescence (Supplementary Figure 3.1). These results indicated that MPO HC labeled with Cy5-hydrazide in a time dependent manner. Although dependent on maximal intensity parameters used for the fluorescence imaging (Supplementary Figure 3.1B), the appearance of the (heme b)-LC product lags behind the Cy5-hydrazide labeling. This indicates that the final release of the (heme b)-LC from the sulfonium linkage maybe a slower process than the initial labeling and ester bond

disruption. It is important to note that the LC of MPO was still not labeled although the LC was cleaved from the MPO dimer by Cy5-hydrazide as observed in the protein staining.

### 3.3.7 Mass spectrometric analysis

To determine which MPO amino acid becomes modified during reaction with hydrazide analogs, we processed identical samples of MPO (1.2  $\mu\text{M}$ ) with and without  $\text{H}_2\text{O}_2$  (40  $\mu\text{M}$ ) and BAH (5 mM). SDS-PAGE analysis of the reactions showed the incubation of with  $\text{H}_2\text{O}_2$  and BAH resulted in release of the (heme b)-LC fragment (data not shown). Once confirmed, reaction samples were subjected to tryptic digestion and peptide mapping using LC-MS/MS. To identify the modified sites on MPO, mass spectrometer data was pooled and analyzed for either an accurate mono isotopic mass modifier for  $\text{C}_7\text{H}_5\text{O}$  of 104.03 Da or the intact BAH modifier corresponding to  $\text{C}_7\text{H}_8\text{N}_2\text{O}$  of 136.15 Da. The rationale for this approach was based on BAH ( $\text{C}_7\text{H}_8\text{N}_2\text{O}$ ) reaction with any amino acid in the MPO protein; causing hydrazine release; thus both products were screened for in both datasets.

Using the same search parameters, the MPO alone sample lacked the presence of either a 104 or 136 Da molecular weight adduct. For the inactivated MPO/  $\text{H}_2\text{O}_2$ / BAH sample, three confident 104 Da modification sites at Lys (K) were identified. As shown in Figure 3.6A, MS/MS fragmentation of the doubly charged ion ( $m/z$  806.90 Da) gave a sequential b and y ion sequence to match the sequence of one peptide from human MPO (K<sup>138</sup>NQADCIPFFR,  $[\text{M}^+\text{H}]^+$  1612.79 Da) with a benzoic acid radical modification. The b and y ions showed that the BAH modification site was located at the <sup>HC</sup>Lys<sup>138</sup> residue (Table 3.1). MS/MS fragmentation of the doubly charged ion ( $m/z$  522.78 Da) gave a sequential b and y ion sequence to match the sequence of one peptide from human MPO (K<sup>308</sup>YLPTYR,  $[\text{M}^+\text{H}]^+$  1044.55 Da) with a BAH modified MW. MS/MS fragmentation of the doubly charged ion ( $m/z$  994.16 Da) showed a



sequential b and y ion sequence to match the sequence of one peptide from human MPO (K<sup>463</sup>LMEQYGTPNNIDIWMGGVSEPLKR, [M<sup>+</sup>H]<sup>+</sup> 2980.47 Da) with a benzoic acid hydrazide modification (Supplementary Figure 3.2). The coverage based on peptides identified by the program represented was 73% and these exact amino acids are indicated by the bold text from the mature MPO protein shown in Figure 3.6A. To assess the relative proximity of the benzoic acid (added 104 MW) adducts to the central heme and substrate accessibility channel, a representative image was constructed using the coordinates deposited in the Protein Data Bank (NCBI accession code 3F9P). In this representation, the mature MPO protein is a homodimer; each monomer consists of a light chain (106 amino acids, shown as pink) and a heavy chain (467 amino acids, light blue). Modified residues of three Lys residues are depicted in red as shown in Figure 3.6B.

In addition, mass spectrometry analysis of tryptic MPO peptides indicated eight peptides had an increased mass corresponding to oxidization of methionine (Met) residues. Comparison with the MPO protein alone, there are 7 methionine (Met) residues (<sup>LC</sup>Met<sup>85</sup>, <sup>LC</sup>Met<sup>87</sup>, <sup>HC</sup>Met<sup>243</sup>, <sup>HC</sup>Met<sup>249</sup>, <sup>HC</sup>Met<sup>306</sup>, <sup>HC</sup>Met<sup>343</sup> and <sup>HC</sup>Met<sup>385</sup>) were differentially oxidized for MPO in a reaction of MPO (1.2 mM) with BAH (5 mM) in the presence of sub-inhibitory concentrations of H<sub>2</sub>O<sub>2</sub> (40 μM) in 50mM sodium acetate buffer as shown in Table 3.2. Comparison of the oxidized Met residues reported by Paumann-Page *et al.* for inhibitory concentrations of H<sub>2</sub>O<sub>2</sub> (1.5 mM) eliminated additional oxidation seen in <sup>HC</sup>Met<sup>287</sup>, <sup>HC</sup>Met<sup>411</sup>, <sup>HC</sup>Met<sup>422</sup>, <sup>HC</sup>Met<sup>465</sup> and <sup>HC</sup>Met<sup>478</sup>. Interestingly, the <sup>HC</sup>Met<sup>411</sup> and <sup>HC</sup>Met<sup>465</sup> residues on MPO can be eliminated from consideration also because they were oxidized in the reaction of MPO without H<sub>2</sub>O<sub>2</sub> and may be indicate that some particular Met residues are oxidized at a basal level in MPO.

### 3.3.8 The specificity of BAH cleavage for MPO

To evaluate whether this unique mechanism of ester bond hydrolysis and heme release is specific to MPO or broadly applicable to all such linked peroxidases, we analyzed identical reactions of either MPO or LPO. As previously mentioned, LPO is also a mammalian peroxidase and, similar to MPO, it possesses 2 ester bonds with one each ligating the heme pyrrole A and C rings. BAH mediated cleavage was seen for MPO and not LPO. Figure 3.7 is the results of obtained for the general protein staining (Figure 3.7A) and heme-dependent chemiluminescence (Figure 3.7B). Treatment of LPO with BAH and H<sub>2</sub>O<sub>2</sub> had no effect on the protein as monitored by either method. The LPO protein remained intact (Figure 3.7A), and of the same relative quantity of active heme remained associated with the LPO protein (Figure 3.7B). We found no evidence for the hydrolysis of the ester bonds in the case of LPO incubation with BAH as determined by the lack of degradation or cleavage bands or loss of catalytic potential due to heme liberation for the parent protein (Figure 3.7). It is possible that lack of cleavage of the heme in the case of LPO is governed by other structural constraints that the BAH does not match well with and that another hydrazide could fit the LPO lock more efficiently and allow for release the heme b for this peroxidase. These results indicate that BAH-mediated peroxidase cleavage is specific to MPO and suggest that fluorescent hydrazides could be applied for the specific labeling of MPO.

### **3.4 Discussion**

This study had 2 broad goals (1) to probe the structure and function relationship between BAH mediated cleavage of ester linkages from the heme b prosthetic group to the parent MPO heterodimer subunits and (2) to gain insight into the underlying chemistry that allows this cleavage to occur. The concentration dependent relationship for reactions in the presence and absence of BAH in mixtures of increasing H<sub>2</sub>O<sub>2</sub> concentration presented in Figure 3.1 clearly

demonstrates that the underlying mechanism of inactivation of MPO by BAH is fundamentally different from the heme destruction caused by high levels of H<sub>2</sub>O<sub>2</sub> [117]. Most obviously, the latter results in the disruption of the porphyrin macrocycle and release of iron (Fe) from the cofactor, which is evident in lanes 7 and 8 in both cases. In contrast, the hydrazide-dependent mechanism leaves the heme intact over a significant range of concentration and this activity with respect to oxidation to produce chemiluminescent signal remains associated with the LC-heme product (Figure 3.1).

Hydrazide-containing compounds are well-documented inhibitors of MPO and others peroxidases, including studies of HRP by phenylhydrazide [126, 127] and microperoxidase-11 by 4-ABAH [128]. The inhibition of various peroxidases have been studied for a number of these enzymes but most demonstrate loss of the Fe coordination by the modification of the heme b ring as is the case for the hydrazide-induced carbene Fe-porphyrin complex described for cytochrome P450 [130] and or methionine-oxidation of MPO by incubation with excess H<sub>2</sub>O<sub>2</sub> [117]. In both of these cases, the Fe is lost due to rearrangement of electrons in the architecture of the heme. However, hydrazide-mediated ester bond disruption is a new observation in the field of MPO inactivation [28]. Here we probed the ability of different BAH analogs to fit into the active site channel of MPO and how modifications to the inhibitor might impact their relative access to the HC ester bond position between the pyrrole ring C and a distal <sup>HC</sup>Glu<sup>242</sup>. To do this we again tracked the heme b via chemiluminescence signal (Figure 3.2A-B) and correlated the extent of (heme b)-LC protein band development with their respective Hammett coefficients ( $\sigma$ ) for the *meta*- and *para*-substituted compounds (Figure 3.2C). In the Hammett relationship analysis, positive  $\sigma$  indicates an electron-withdrawing group and a negative value for  $\sigma$  is an electron-donating group, so -CF<sub>3</sub> has an overall + 0.54 electron-withdrawing potential and the -NH<sub>2</sub>

substituent carries a  $\sigma$  value of -0.66. Interestingly, maximal generation of (heme b)-LC product occurs at near neutral electron potential indicating that the cleavage is not dependent on the electron potential associated with the aromatic ring and may instead be dependent on accessibility to the heme b ring in the MPO active site (Figure 3.2C). Once accessibility of the inhibitors to the heme b prosthetic group was a potential concern, we wanted to confirm that Compound I was the oxidizing species and that  $\text{H}_2\text{O}_2$  was expressly required (Figure 3.3).

To probe the mechanism by which BAH analogs mediate the disruption of  $^{\text{HC}}\text{Glu}^{242}$  ester bond linkage, we characterized the inhibitory effect of a fluorescence hydrazide analog as a means to track the underlying chemistry. Luminescence-based kinetic results showed that indeed addition of Cy5-hydrazide and  $\text{H}_2\text{O}_2$  mediated inhibition of MPO (Figure 3.4) and follow-up SDS gel analysis of the MPO/Cy5-hydrazide/ $\text{H}_2\text{O}_2$  system confirmed disruption of the ester bond at  $^{\text{HC}}\text{Glu}^{242}$  (Figure 3.5) and vinyl-sulfonium linkage. The loss of vinyl-sulfonium bond must occur either directly through electron rearrangements triggered by the initial disruption of the ester bond linkage or by a separate nucleophilic attack event. Of note, access of the inhibitor-tethered probes to the catalytic site directly affected the cleavage and resulting labeling. For instance, both cleavage and labeling were not seen for other fluorescein reporters hydrazides, presumably due to lack of the aliphatic hydrocarbon chains that are present in the Cy5-hydrazide (see Figure 3.4B *inset* for structure of the Cy5-hydrazide used here). It appears from our data (Figure 3.5) that loss of the vinyl-sulfonium bond maybe an overall slower process evident by the delay or lag seen in the appearance of the (heme b)-LC band relative to the Cy5-hydrazide labeling of the HC (Figure 3.5B & Supplementary Figure 3.1B). The labeling did not appear non-specific in nature under our conditions, as the parent MPO bands were not modified by the Cy5-hydrazide during either the concentration dependence (Figure 3.5) or the time course shown

(Supplementary Figure 3.1), thus indicating modification of MPO by the Cy5-hydrazide only followed the cleavage event.

To better understand the sites of modification of MPO caused by BAH inhibition, a peptide mass fingerprinting (PMF) study was performed comparing MPO alone and MPO treated with a relatively low concentrations  $\text{H}_2\text{O}_2$  (40  $\mu\text{M}$ ) in the presence of BAH. Our goal was to determine sites that may help to explain our Cy5-hydrazide inhibition and labeling experiments. Coverage of identified peptides was 73% of the mature MPO protein (Figure 3.6). Scanning for the peptides modifications of either 136 or 104 Da showed three Lys ( $^{\text{HC}}\text{Lys}^{138}$ ,  $^{\text{HC}}\text{Lys}^{308}$ , and  $^{\text{HC}}\text{Lys}^{463}$ ) residues where the benzoic acid adducts (104 Da) had formed following oxidation of the BAH by Compound I causing the release of the  $\text{NH}_2\text{-NH}_2$ . The literature does report that formation of phenyl radicals follows incubation of phenylhydrazide with HRP in the presence of  $\text{H}_2\text{O}_2$ , whereby the  $\text{N}_2$  is lost upon radical formation and the phenyl radical adds directly to the heme b ring, which presumably causes loss of the centrally bonded Fe [126]. A similar radical formation would explain the addition of the 104 Da adduct to each of the Lys residues *in lieu* of the possible full BAH adduct (136 Da), but unlike the case with HRP we have no evidence for any of these radicals being added to the covalently tethered heme ring of MPO. Unfortunately, these Lys modifications once mapped on the MPO crystal structure (Figure 3.6B) demonstrated the modification were peripheral to the heme and important active site residues, thus implying these alteration do not explain the inhibition of BAH by MPO. In fact, these benzoic acid radicals may modify the Lys residues on the back of the neighboring juxtaposed MPO molecule in the dimer.

One draw back of this PMF method is that to identify the modification you must have prior knowledge of the underlying chemistry and deviation from the predictions are not readily

apparent. It is interesting that we can observe oxidation of the  $^{13}\text{C}\text{Met}^{243}$ , presumably due to the loss of the vinyl-sulfonium bond consistent with our previous results [28]. Optimally, application of the fluorescence probe tracker (i.e. Cy5-hydrazide) could be used to address this fundamental question as to where the R-group of a R-NH<sub>2</sub>-NH<sub>2</sub> compound (i.e. R-group is Cy5) would ultimately reside. Solubility issues of MPO labeled with Cy5-hydrazide hampered initial mass spectrometer studies and thus we had to revert back to the aforementioned BAH-mediated MPO inhibition. Use of Cy5-hydrazide demonstrated that the dye did not co-migrate with the (heme b)-LC band on the SDS-gel (see Figure 3.5 & Supplementary Figure 3.1). Collectively, our data only supports the scenario, whereby the Cy5 labels the HC of MPO. It is possible these findings would apply to any hydrazide analog capable of mediating the hydrolysis of the ester bond at  $^{13}\text{C}\text{Glu}^{242}$  including BAH, 4-FBAH, and DMABAH. Furthermore, to mediate the cleavage of the ester bond and specific labeling of the MPO HC a nucleophilic substitution (i.e. SN<sub>2</sub>) reaction must occur between the terminal NH<sub>2</sub>- group of the Cy5- hydrazide and the carbonyl of the  $^{13}\text{C}\text{Glu}^{242}$  directly bonded to the ester linkage. This potential mechanism would allow for the new bond formation between the NH<sub>2</sub>- group and carbonyl, as the ester bond is lost. We determined that BAH could not mediate the necessary cleavage in the absence of the H<sub>2</sub>O<sub>2</sub> (Figure 3.3C-D) indicating a role for MPO driven catalysis in the mechanism of disruption of ester bond at  $^{13}\text{C}\text{Glu}^{242}$ . It is apparent that a further chemical rearrangement leads to oxidation of the  $^{13}\text{C}\text{Met}^{243}$  as indicated by the PMF results but the exact chemical nature of transient species remains illusive and future studies needed to determine to characterize this further.

Taken together, our results showed that BAH and other benzyl hydrazides can mediate this unique ester bond hydrolysis that is different from the inhibition recently described for H<sub>2</sub>O<sub>2</sub> [117]. We showed that BAH must be oxidized by Compound I to mediate the cleavage of the

heme anchoring ester linkages. We showed that certain fluorescent reporter hydrazide compounds mediated a similar cleavage event as seen for BAH of the MPO protein releasing the still active (heme b)-LC subunit from the parent HC of MPO. This labeling is predicted to be possible through a nucleophilic attack at the carbonyl at <sup>HC</sup>Glu<sup>242</sup> leading to chemical rearrangements resulting in the loss of the sulfonium ion linkage between <sup>HC</sup>Met<sup>243</sup> and the pyrrole A ring. Although unable to prove this by MS analysis, we did observe oxidation of the <sup>HC</sup>Met<sup>243</sup> to a sulfoxide, which resulted in the loss of the vinyl-sulfonium bond. We also presented evidence for modification to the MPO protein in BAH reactions with H<sub>2</sub>O<sub>2</sub> that causes other important changes to the MPO protein including benzoic acid radical adduct formation of three Lys (<sup>HC</sup>Lys<sup>138</sup>, <sup>HC</sup>Lys<sup>308</sup>, and <sup>HC</sup>Lys<sup>463</sup>) residues and oxidation of the <sup>HC</sup>Met<sup>243</sup> and <sup>HC</sup>Met<sup>249</sup> residues can not be ascribed to simple incubation with H<sub>2</sub>O<sub>2</sub>. Finally, we showed that this unique cleavage is specific to MPO and does not occur to an appreciable level in the analogous mammalian peroxidase LPO (Figure 3.7). Our findings presented here may provide new avenues to fuel drug discovery efforts to designing new MPO inhibitors that would limit inflammation.

**Table 3.1 Mass spectrometry analysis of tryptic MPO peptides indicated three peptides had an increased mass corresponding to the formation of the benzoic acid adducts.**

Comparison was made between peptides observed in the MPO protein alone and a reaction of MPO (1.2  $\mu$ M) with BAH (5 mM) in the presence of H<sub>2</sub>O<sub>2</sub> (40  $\mu$ M) in 50mM sodium acetate buffer at pH 5.6. The statistical probabilities for the correct identification peptides are shown by the peptide–spectrum matches with the Sequest score (XCorr) and the posterior error probability (PEP) values. The smaller the PEP value, the more certainty there is in the identification of a correctly matched peptide.

MPO amino acid	Identified modified peptide	Oxidized residue	MH+ [Da]	XCorr	PEP
<sup>HC</sup> Lys <sup>138</sup>	<b>I</b> kNQADcIPFFR	K2	1612.79	2.25	7.9E-3
<sup>HC</sup> Lys <sup>308</sup>	<b>k</b> YLPTYR	K1	1044.55	2.18	5.9E-2
<sup>HC</sup> Lys <sup>463</sup>	<b>k</b> LMEQYGTPNNIDIWMGGVSEPLKR	K1	2980.47	4.13	6.4E-5



**Table 3.2 Mass spectrometry analysis of tryptic MPO peptides indicated eight residues had an increased mass corresponding to oxidization of methionine (Met) residues.**

Comparison was made between peptides observed in the MPO protein alone and a reaction of MPO (1.2  $\mu$ M) with BAH (5 mM) in the presence of H<sub>2</sub>O<sub>2</sub> (40  $\mu$ M) in 50 mM sodium acetate buffer at pH 5.6. The <sup>HC</sup>Met<sup>243</sup> and <sup>HC</sup>Met<sup>249</sup> peptide was identified as the sole peptide not previously identified as a sensitive to oxidization by inhibitory concentrations (1.5 mM) of H<sub>2</sub>O<sub>2</sub> as previous reported by Paumann-Page *et al.* [19]. The statistical probabilities for the correct identification peptides are shown by the peptide–spectrum matches with the Sequest score (XCorr) and the posterior error probability (PEP) values. The smaller the PEP value, the more certainty there is in the identification of a correctly matched peptide.

MPO Amino Acid	Identified Modified Peptide	Oxidized Residue	MH+ [Da]	XCorr	PEP
<sup>LC</sup> Met <sup>85</sup> , <sup>LC</sup> Met <sup>87</sup>	SL <b>m</b> F <b>m</b> QWGQLLDHDLDF <b>T</b> PEPAAR	M3; M5	2850.32	2.95	1.7E-2
<sup>LC</sup> Met <sup>87</sup>	SLMF <b>m</b> QWGQLLDHDLDF <b>T</b> PEPAAR	M5	2834.32	4.41	6.4E-8
<sup>HC</sup> Met <sup>243</sup> , <sup>HC</sup> Met <sup>249</sup>	<i>SSEmPELT<b>S</b>mHTLLLR</i>	M4; M10	1876.91	2.89	9.4E-6
<sup>HC</sup> Met <sup>306</sup>	KIVGAMVQIITYRDYLPLVLGPTA <b>m</b> R	M25	2934.63425	2.91	4.4E-2
<sup>HC</sup> Met <sup>343</sup>	IANVFTNAFRYGH <b>T</b> LIQPF <b>m</b> FR	M20	2659.35807	4.07	4.7E-5
<sup>HC</sup> Met <sup>385</sup>	GL <b>m</b> ATPAK	M3	804.42266	1.69	2.4E-2

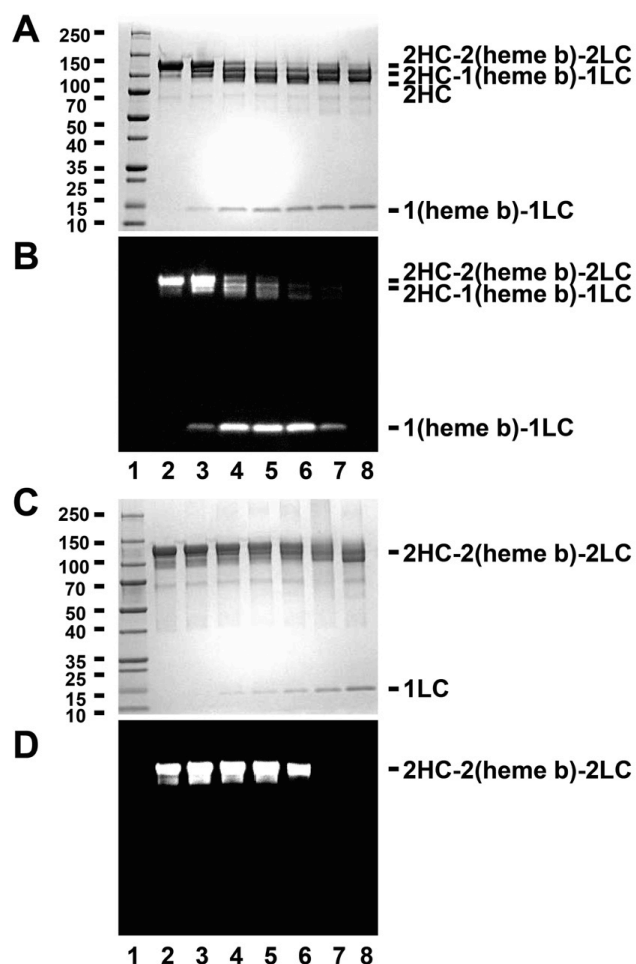


**Figure 3.1 Effect of BAH on MPO compared to the heme destruction generated by high dose  $H_2O_2$  treatment.**

A-B, Total protein-stained gel image (A & C) and luminescence generated images (B & D) for a molecular weight marker (lane 1), MPO alone (1.2  $\mu$ M, lane 2), and reactions of MPO (1.2  $\mu$ M) with BAH (5 mM) in the present of increasing concentrations of  $H_2O_2$ , namely 8  $\mu$ M (lane 3), 40  $\mu$ M (lane 4), 80  $\mu$ M (lane 5), 160  $\mu$ M (lane 6), 800  $\mu$ M (lane 7) and 8 mM (lane 8) for 10 min. C-D, Similar reactions were set up without BAH for 10 min prior to loading the sample. Experiments conducted as described under “Experimental Procedures.”

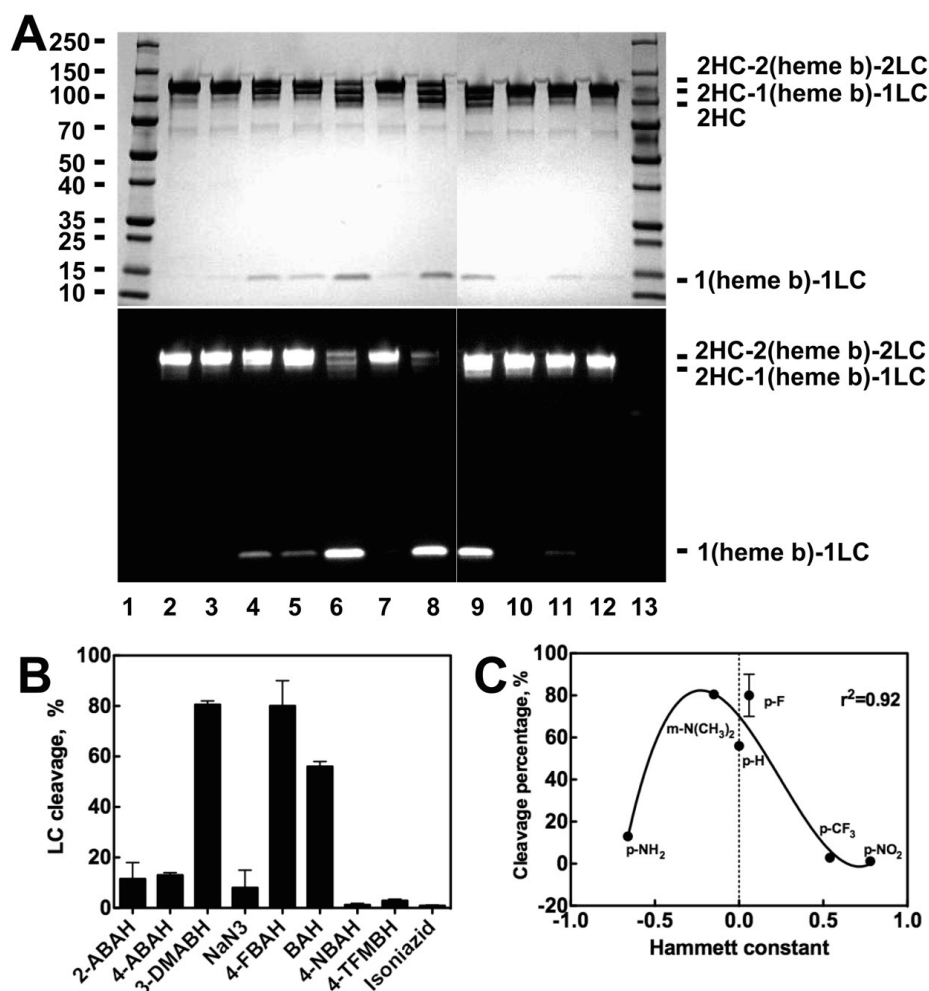


**Figure 3.2 Screening of BAH analogs for production of (heme b)-LC cleavage product.**

A, A representative protein-stained gel images (*upper*) and luminescence generated images (*lower*) for the molecular weight marker (lane 1), MPO alone (1.2  $\mu$ M, lane 2), 1.2  $\mu$ M MPO with 20  $\mu$ M H<sub>2</sub>O<sub>2</sub> (lane 3), 1.2  $\mu$ M MPO with 20  $\mu$ M H<sub>2</sub>O<sub>2</sub> incubated for 1 hr with the different BAH analogs each at 4 mM inhibitor concentration, including 2-ABAH (lane 4), 4-ABAH (lane 5), 3-DMABAH (lane 6), NaN<sub>3</sub> (lane 7), 4-FBAH (lane 8), BAH (lane 9), 4-NBAH (lane 10), 3-TFMBAH (lane 11) and isoniazid (lane 12). B-C, Quantification of the experiment results in Panel A. The cleavage percentage is expressed relative to the protein densitometry for MPO alone. This screen was repeated (n=3) and relative densitometry (%) for the generation of the

protein stained (heme b)-LC cleavage product is shown (Panel B) alongside a correlation of (heme b)-LC cleavage product as a function of the Hammett constant ( $\sigma$ ) (Panel C), this correlation was analyzed with non-linear regression to a third order polynomial using GraphPad Prism software. Quantification was done from three independent experiments and shown as mean  $\pm$  S.E.M. Additional methods related to this screen are available under “Experimental Procedures.”

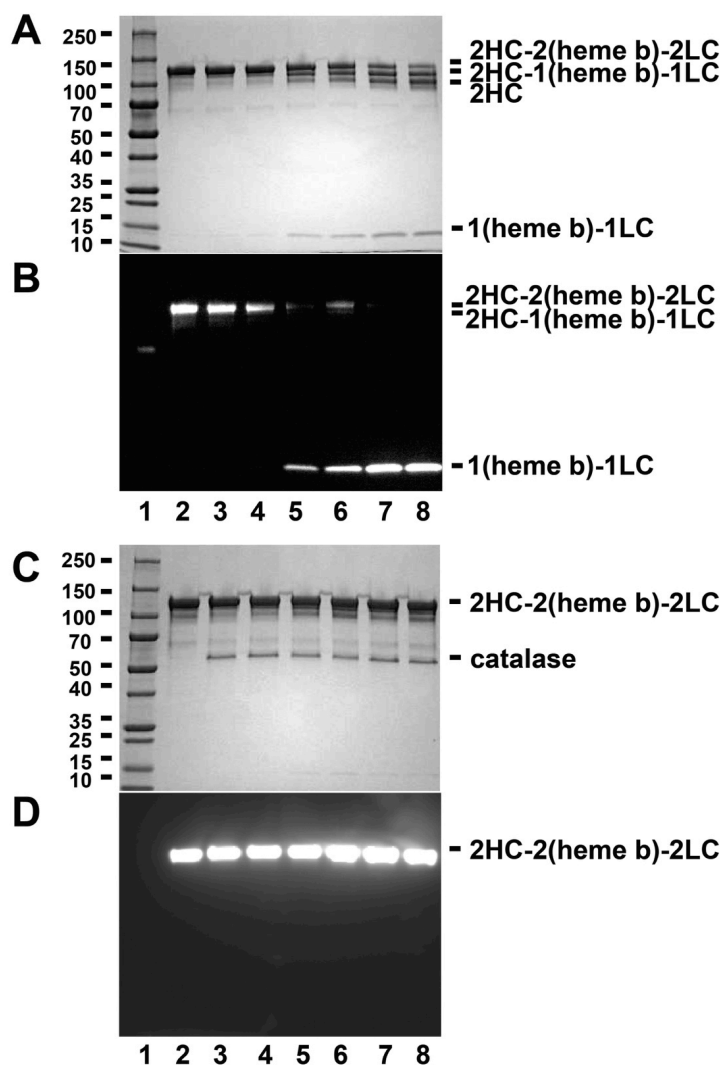


**Figure 3.3 Cleavage of MPO by BAH is dependent on  $H_2O_2$ .**

A-B, Protein-stained image (A & C) and luminescence imaging (B & D) for a molecular weight marker (lane 1), MPO alone (1.2  $\mu$ M, lane 2), and reactions of MPO (1.2  $\mu$ M) with increasing concentrations of BAH, namely 0.025 mM (lane 3), 0.25 mM (lane 4), 2.5 mM (lane 5), 5 mM (lane 6), 12.5 mM (lane 7) and 25 mM (lane 8) for 10 min. C-D, Similar reactions where BAH and MPO were separately incubated with catalase (20 units) for 1hr prior to mixing. Experiments conducted as described under “Experimental Procedures.”

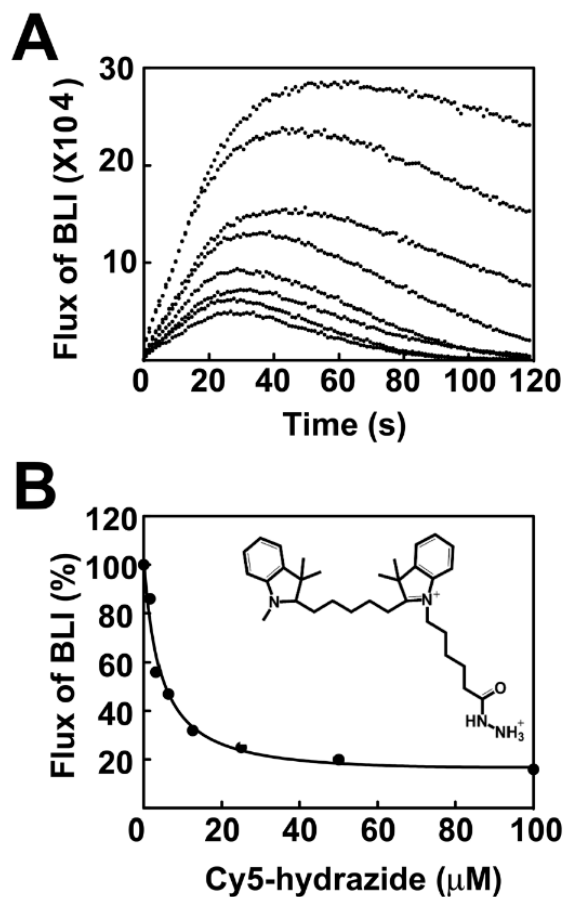


**Figure 3.4 Inactivation of MPO by Cy5-hydrazide.**

A, Reactions of 400  $\mu\text{M}$  luminol were incubated with MPO (140 nM) in MEBSS buffer in the absence or presence of varied final concentration of Cy5-hydrazide (1.6  $\mu\text{M}$ , 3.125  $\mu\text{M}$ , 6.25  $\mu\text{M}$ , 12.5  $\mu\text{M}$ , 25  $\mu\text{M}$ , 50  $\mu\text{M}$ , 100  $\mu\text{M}$ ). The auto-injector function of the Varioskan plate reader was used to initiate the reaction via addition of 20  $\mu\text{M}$   $\text{H}_2\text{O}_2$ . B, Apparent  $\text{IC}_{50}$  of Cy5-hydrazide (5.5  $\mu\text{M}$ ) on MPO was calculated based on the percentage of inhibition of MPO peroxidase activity. Titrations were performed as described in greater detail under “Experimental Procedures.”

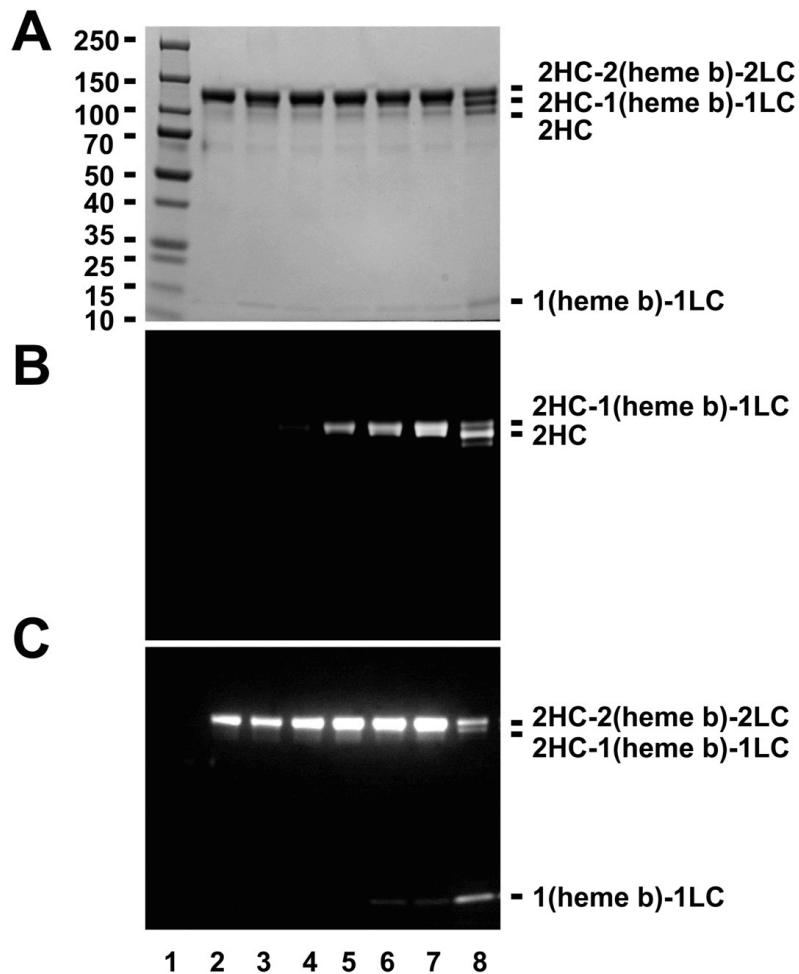


**Figure 3.5 Tracking Cy5 modification following cleavage of the (heme b)-LC from HC of MPO.**

Protein-stained bands (A), fluorescence (B), luminescence imaging (C) for a molecular weight marker (lane 1), MPO alone (1.2  $\mu$ M, lane 2), and reactions of MPO (1.2  $\mu$ M) with increasing concentrations of Cy5-hydrazide, namely 0.05 mM (lane 3), 0.1 mM (lane 4), 0.5 mM (lane 5), 1 mM (lane 6), 2 mM (lane 7) and 5 mM (lane 8) in the presence of 20  $\mu$ M H<sub>2</sub>O<sub>2</sub> for 10 min. Additional details related to this experiment can be found in “Experimental Procedures.”

A

CPEQDKYRTI	TGMCNRRSP	TLGASNRAFV	RWLP AEYEDG	FSLPYGWTPG	50
VKRN <sup>G</sup> FPVAL	ARAVSNEIVR	FPTDQLTPDQ	ERSL <sup>M</sup> <sup>F</sup> MQWG	QLL <sup>H</sup> LDLDF	100
PEPAARAS <sup>FV</sup>	TGVN <sup>C</sup> ETSCV	QQPPCFPLKI	PPNDPRI <sup>K</sup> NQ	ADCIPFFRSC	150
<sup>#</sup> PACPGSN <sup>*</sup> ITI	RN <sup>Q</sup> INAL <sup>T</sup> SE	VDAS <sup>M</sup> VYGSE	EPLARN <sup>L</sup> R <sup>N</sup> M	SNQLGLLAVN	200
QRFQDNGRAL	L <sup>P</sup> FDNLHDDP	CLLT <sup>*</sup> NRSARI	PCFLAGD <sup>T</sup> RS	SEM <sup>P</sup> ELT <sup>S</sup> M <sup>H</sup>	250
TLLLREHNRL	A <sup>T</sup> ELKSLNPR	WDGERLYQEA	RKIVGAMVQI	ITYRDYLP <sup>L</sup> V	300
LGPTA <sup>M</sup> R <sup>K</sup> YL	PTYRSY <sup>N</sup> DSV	DPRIANVFTN	AFRYG <sup>H</sup> T <sup>L</sup> IQ	PF <sup>M</sup> FR <sup>L</sup> DNRY	350
QPMEPNPRVP	LSRVFFASWR	VVLEGGIDPI	LRGL <sup>M</sup> ATPAK	LNRQ <sup>N</sup> QIAVD	400
EIRERLFEQV	MRIGLDLPAL	<sup>N</sup> MQRSRDHGL	PGYNAWRRFC	GLPQPETV <sup>G</sup> Q	450
LGTVLRNLKL	AR <sup>K</sup> LMEQYGT	PNNIDIWMGG	VSEPLKRKGR	VGPLLACIIG	500
TQFRKLRDGD	RFWWENEGVF	SMQQRQALAQ	ISLPRIICDN	TGITT <sup>V</sup> SKNN	550
IFMSNSYPRD	FV <sup>*</sup> NCSTLPAL	NLASWREAS			579

B

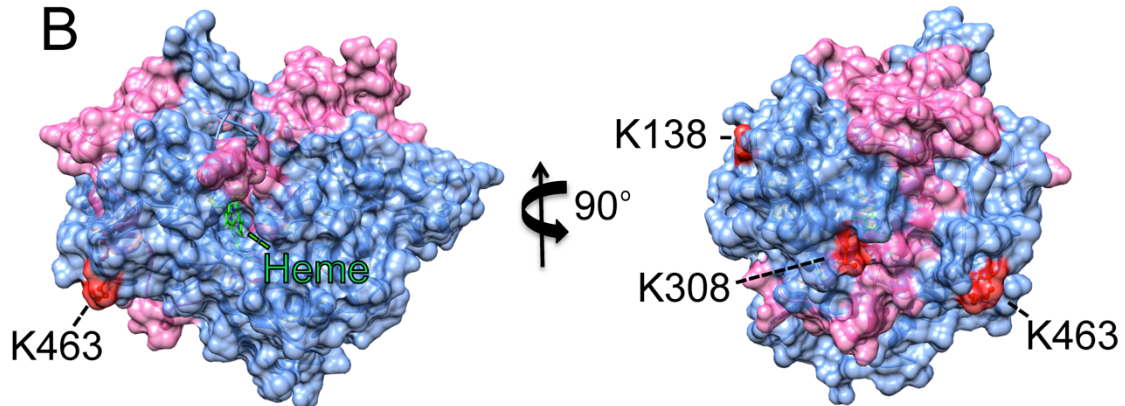




**Figure 3.6 Identification of modified sites on myeloperoxidase after incubation with BAH and H<sub>2</sub>O<sub>2</sub>.**

A, LC-MS/MS analysis rectified 73% coverage of the mature MPO protein. The amino acid sequence of the heterodimer MPO is shown with the light chain designated by the blue text and the heavy chain by the black text. Peptides coverage generated from the tryptic digestion of MPO followed by nanoLC-MS/MS analysis is shown in bold, oxidized methionine residues are highlighted in red with white text, and each modified lysine residues (<sup>HC</sup>Lys<sup>138</sup>, <sup>HC</sup>Lys<sup>308</sup>, and <sup>HC</sup>Lys<sup>463</sup>) are shown in larger red text. Orange text indicates a hexa-peptide excised from the mature MPO protein, thus not factored into the coverage. Highlighted in green are <sup>LC</sup>Asp<sup>94</sup> and <sup>HC</sup>Glu<sup>242</sup> that form ester bond linkages with the heme b. Other important residues are marked including catalytic residues (*turquoise*), glycosylation sites (\*), the bridging cysteine (#) and calcium-binding residues (*underlined*). (B) The 3D structure of the MPO monomer (PDB #3F9P) is shown with <sup>HC</sup>Lys<sup>138</sup>, <sup>HC</sup>Lys<sup>308</sup>, and <sup>HC</sup>Lys<sup>463</sup> indicated in red. The mature MPO is a homodimer, each monomer consists of a light chain (106 amino acids, *pink*) and a heavy chain (467 amino acids, *light blue*). The structure was oriented with a central heme is in the center and then rotated to the right. The image was created using Chimera ([www.cgl.ucsf.edu/chimera](http://www.cgl.ucsf.edu/chimera)).

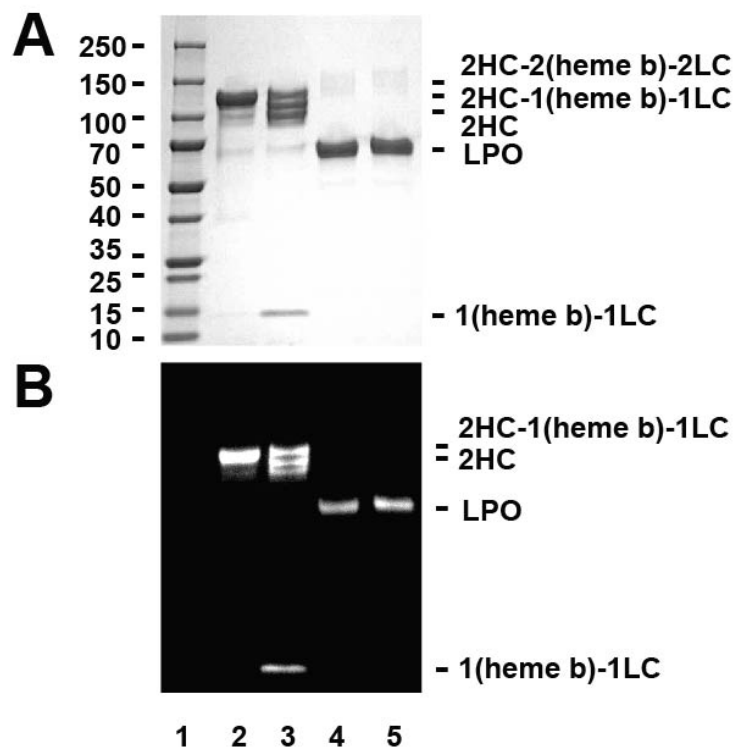
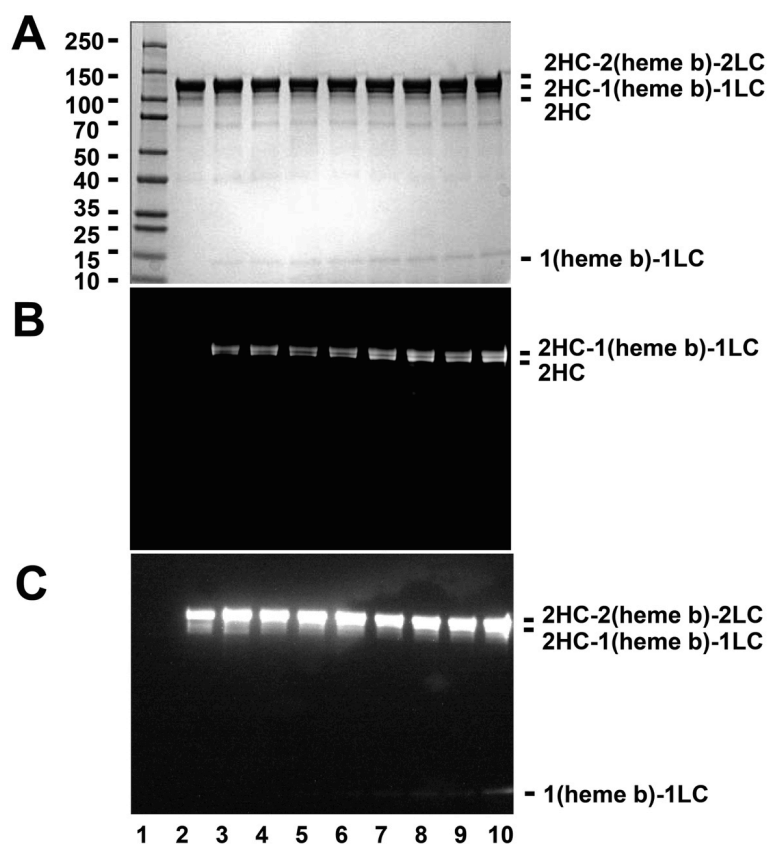


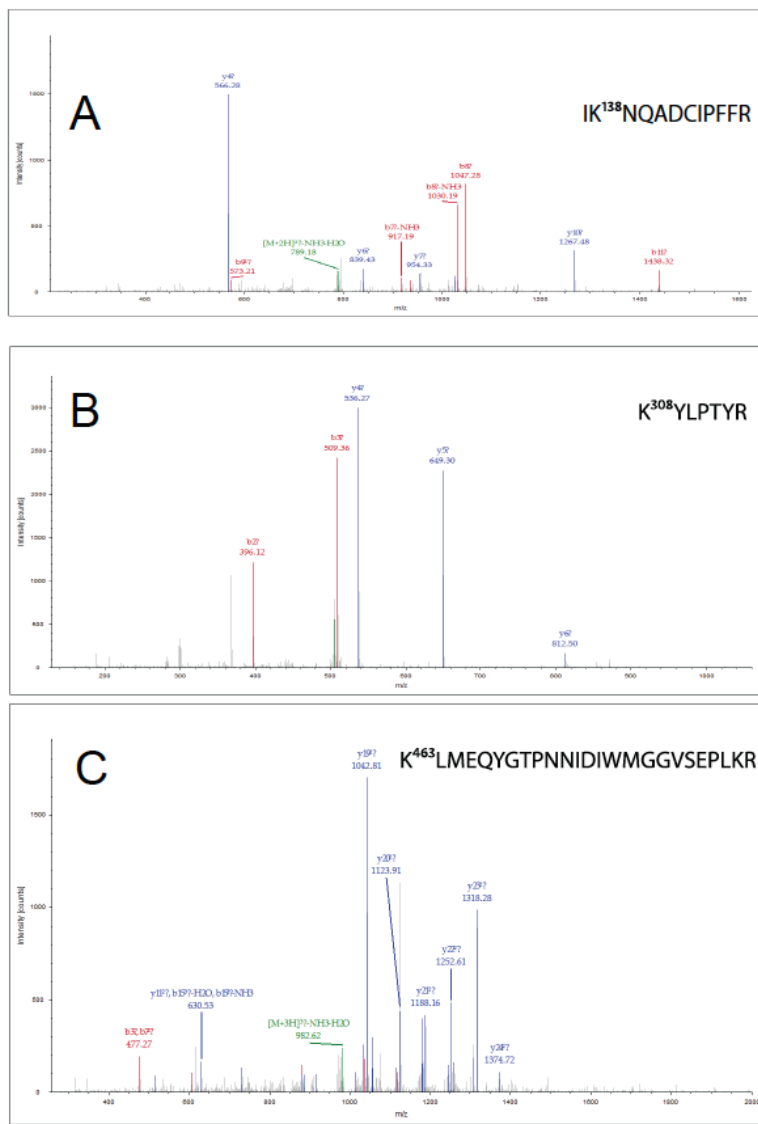
**Figure 3.7 BAH mediated release of heme b is specific to MPO.**

Total protein-stained gel images (Panel A) and luminescence generated images (Panel B) for a molecular weight marker (lane 1), MPO alone (1.2  $\mu$ M, lane 2), and reactions of MPO (1.2  $\mu$ M) with 20 mM BAH in the presence of 20  $\mu$ M H<sub>2</sub>O<sub>2</sub> (lane 3), LPO (1.5  $\mu$ M) alone (lane 4), and LPO (1.5  $\mu$ M) with 20 mM BAH in the presence of 20  $\mu$ M H<sub>2</sub>O<sub>2</sub> (lane 5) at room temperature for 30 min. Experiments conducted as described under “Experimental Procedures.”



**Supplementary Figure 3.1 Stability and time dependent HC-labeling of MPO by Cy5-hydrazide.**

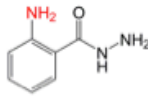
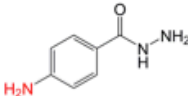
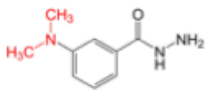
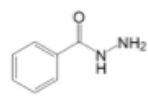
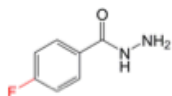
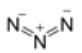
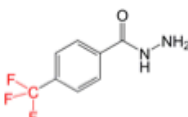
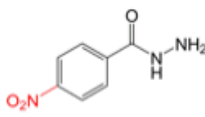
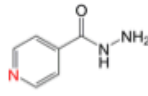
Protein-staining (A), fluorescence (B), and luminescence (C) images of a SDS-PAGE gel of a MPO inactivation reaction sampled at 30 min intervals (lane 2-10) over 4h. The time course was set up as individual reactions that were staggered. This allowed us to simultaneously quench the MPO activity by addition of the 2% SDS contained in the gel loading buffer (Data not shown). The reaction contained MPO (1.2  $\mu$ M) and a lower dose of Cy5-hydrazide (2.5 mM) with 20  $\mu$ M  $H_2O_2$  added. Lane 1 is a molecular weight marker and the experiments conducted as described under “Experimental Procedures.”



**Supplementary Figure 3.2 LC-MS/MS spectrometry analysis of MPO modification by BAH in the presence of sub-inhibitory concentrations of H<sub>2</sub>O<sub>2</sub>.**

MS/MS fragmentations of the doubly charged ions (m/z 806.90 Da, m/z 522.78 Da, m/z 994.16 Da) gave their corresponding b and y ion sequences used to identify the sequences and specific amino acid peptide from human MPO (IK<sup>138</sup>NQADCIPFFR, [M<sup>+</sup>H]<sup>+</sup> 1612.79 Da, K<sup>308</sup>YLPTYR, [M<sup>+</sup>H]<sup>+</sup> 1044.55 Da, K<sup>463</sup>LMEQYGTPNNIDIWMGGVSEPLKR, [M<sup>+</sup>H]<sup>+</sup> 2980.47 Da) with a benzoic acid radical modification (A, B, C).

**Supplementary Table 3.1** Summary of the hydrazide analogs used in this study presented with the reported  $K_i$  determine values previously determined in Huang *et al.* ABB 2014.

Inhibitor	Structure	$K_i$ ( $\mu\text{M}$ )
<b>2-ABAH</b>		<b>0.16</b>
<b>4-ABAH</b>		<b>0.23</b>
<b>3-DMABAH</b>		<b>0.56</b>
<b>BAH</b>		<b>0.69</b>
<b>4-FBAH</b>		<b>0.83</b>
<b>NaN<sub>3</sub></b>		<b>0.84</b>
<b>4-TFMBAH</b>		<b>3.08</b>
<b>4-NBAH</b>		<b>3.7</b>
<b>Isoniazid</b>		<b>10</b>

## **Chapter 4 Inhibition of myeloperoxidase by rheumatoid arthritis drug tofacitinib**

### **4.1 Introduction**

Rheumatoid arthritis (RA), a systemic and chronic autoimmune disease, is characterized by dysregulation of pro-inflammatory cytokines in inflammation and structural damage of joints. The up-regulated cytokines are responsible for the recruitment and activation of immune cells (CD4+ T cells, B cells, macrophages and neutrophils) in the synovial fluid and inflamed joints of RA [143]. The abnormal immune response may cause joint damage and systemically affect the other organs, which gives rise to the co-morbidities [144, 145]. The representative co-morbidities include lung cancer [146], serious infections [147], myocardial infarction and other cardiovascular diseases [148]. It may cause significant disability without constant medical interference [144].

The cytokines play a pathological role in the progression of RA [149, 150]. Biological interference of cytokines such as interleukins (IL) and tumor necrosis factor (TNF) showed clinical promise and efficacy for the treatment of RA [151]. Janus kinase (JAK) family of non-receptor tyrosine kinases (JAK1, JAK2, JAK3 and tyrosine kinases 2) are critical in regulating immune and inflammatory responses to cytokines [152]. The binding of cytokines to their receptors integrates the signals from cytokines to initiate the signal transduction [153]. The activation of JAKs phosphorylates cytokine receptors, resulting in the phosphorylation and activation of the signal transducers and activators of transcription (STATs) to regulate gene

expression [153, 154]. The compelling evidence that interleukins-JAKs signaling pathway amplify oxidative stress at inflammation sites has focused attention on it as a pharmacological target of RA. Clinical studies with tofacitinib, an oral JAK inhibitor, approved the effective treatment of RA and plaque psoriasis through targeting JAKs [155-157]. The structural comparison of tofacitinib and thioxanthine gives us a clue on the inhibition of myeloperoxidase (MPO) activity.

MPO is a heme-containing peroxidase in myeloid cells (neutrophils and macrophages). It is an abundant protein accounting for 5% of the dry weight in neutrophils and present a less extent in monocytes and macrophages [10]. MPO catalyzes the production of HClO by reacting with H<sub>2</sub>O<sub>2</sub> and Cl. In the context of pathobiology of human inflammatory diseases, MPO has been widely recognized as a biomarker for heightened immune function because of its potential to catalyze the formation of various radicals, secondary MPO-derived DNA and protein products [10]. A plethora of evidence support MPO is a pathogenic mediator of joint inflammation and destruction. There is also an increased amount of MPO plasma level in RA [12, 158, 159]. Recent studies reported that both plasma and synovial fluid (SF) levels of MPO protein were significantly higher in patients with RA compared with healthy controls and the activity of MPO was also correlated with the protein level in SF [12]. In addition, MPO deficiency attenuated RA severity in mouse models without increasing circulating cytokine levels [63], which indicated that MPO is a critical mediator of joint inflammation and tissue damage in experimental RA.

Here we found an oral JAK inhibitor tofacitinib reversibly inhibited MPO peroxidase activity and was docked into the active site moiety of MPO using SYBYL-X 1.3 software. MPO fluorescence endpoint assay determined K<sub>d</sub> (434.08 μM) of tofacitinib on MPO inhibition by using Scientist software. Stopped-flow rapid kinetic analysis determined the K<sub>i</sub> of tofacitinib on

MPO inhibition fitting the progress curves in DynaFit software 3. Analysis of tofacitinib/BAH-treated MPO by SDS-PAGE and in-gel luminescence imaging revealed that tofacitinib prevented the cleavage of MPO by BAH in the presence of H<sub>2</sub>O<sub>2</sub>, which indicates that it may compete with the active site of MPO with BAH. Spectral analysis of reactions of MPO with tofacitinib/BAH demonstrated that tofacitinib could interfere the Soret peak shift from 430 to 413 nm of MPO caused by BAH. This study collectively demonstrates tofacitinib as a reversible inhibitor of MPO providing new avenues for future drug development efforts that aim to diminish the formation of peroxidase-derived oxidants in chronic inflammatory diseases.

## **4.2 Material and Methods**

### **4.2.1 Materials**

Human neutrophil MPO was obtained from Lee Biosolutions Inc. (St. Louis, MO). Tofacitinib citrate was purchased from Euroasia's (Mumbai, India). Benzoic acid hydrazide (BAH) and dimethyl sulphoxide (DMSO) were obtained from Alfa Aesar (Ward Hill, MA). Gelcode Blue was purchased from Pierce (Rochford, IL) for protein staining. The chemiluminescent Western Lightning ultra-reagent was obtained from PerkinElmer Inc. (Waltham, MA) to track the heme prosthetic group.

The assay buffer was prepared by adjusting the pH of sodium acetate buffer to 5.6 with acetic acid. Working solutions of H<sub>2</sub>O<sub>2</sub> were made fresh daily by diluting 30% H<sub>2</sub>O<sub>2</sub> (BDH Chemicals, London, UK) according to the extinction coefficient for H<sub>2</sub>O<sub>2</sub> at 240 nm, 39.4 M<sup>-1</sup>cm<sup>-1</sup> [117, 141]. BAH and tofacitinib citrate were dissolved in DMSO and subsequently diluted into assay buffer. MEBSS buffer (144 mM NaCl, 5.4 mM KCl, 1.2 mM CaCl<sub>2</sub>, 800 μM MgSO<sub>4</sub>, 800 μM NaH<sub>2</sub>PO<sub>4</sub>, 4 mM Hepes, 5.6 mM glucose, pH 7.4 with 1% fetal bovine serum) was used in the luminescence assay for MPO activity, in accordance with the literature [48, 67]. Phosphate



buffer and PBS were prepared to determine the effect of pH on the fluorescence intensity of MPO reaction.

Mice were purchased from Jackson Laboratories (Bar Harbor, ME). Mice were maintained at the Auburn University College of Veterinary Medicine with *ad libitum* access to alfalfa-free chow and water. The Institutional Animal Care and Use committee of Auburn University approved mouse protocols and all procedures were followed in accordance with the Guide for the Care and Use of Laboratory Animals of the National Institutes of Health. For all animal experiments, mice were anesthetized by isoflurane (Piramal Healthcare, Boston, MA) with 1-3% medical grade oxygen using a XGI-8 Anesthesia System (Perkin Elmer). For bioluminescence imaging experiments, we used the IVIS Lumina XRMS Imager (PerkinElmer, Waltham, MA).

#### **4.2.2 MPO fluorescence activity assay**

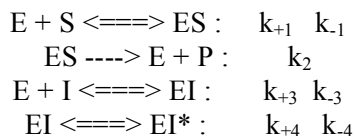
MPO peroxidase activity was measured by monitoring the formation of resorufin from the oxidation of ADHP. This assay was used to study the inhibitory effect of tofacitinib on MPO activity. ADHP oxidation was measured as a function of tofacitinib by use of Spectramax GeminiXPS plate reader (Molecular Devices, CA, USA) with excitation of  $\lambda_{530\text{nm}}$  and emission of  $\lambda_{590\text{nm}}$ . Reactions of ADHP (25  $\mu\text{M}$ ) were incubated with MPO (1.12 nM) and titrated tofacitinib in assay buffer and initiated by the addition of 5  $\mu\text{M}$   $\text{H}_2\text{O}_2$ . The fluorescence intensity endpoint reading was performed after incubation for 5 min. SoftMax Pro software 4.7 parameters included auto-mix time 5 s and auto-calibrate on. Scientist software (MicroMath Inc., Missouri, USA) was used to fit the produced resorufin as a function of tofacitinib concentration for the inhibition of MPO- $\text{H}_2\text{O}_2$  system using the quadratic binding equation.

#### **4.2.3 Transient state analysis by stopped flow kinetics**

To measure MPO activity, ADHP oxidation was monitored as a function of fluorescence intensity over time using QuantaMaster 80 (Photon Technology International, Birmingham, NJ) with a Xe - Arc lamp. Mixtures of MPO, tofacitinib and ADHP were rapidly mixed with H<sub>2</sub>O<sub>2</sub> in acetate buffer (assay buffer) using RX2000 rapid mixing stopped-flow accessory (Applied Photophysics Ltd, Leatherhead, UK) as previously described [28]. In addition, the mixture of MPO, different concentrations of tofacitinib with ADHP and H<sub>2</sub>O<sub>2</sub> in assay buffer were loaded into two different drive syringes of the stopped-flow apparatus and maintained at 25°C for at least 10 min prior to triggering the pneumatic driver. Experiments were initiated with the optimized concentration of H<sub>2</sub>O<sub>2</sub> [28] and performed in a total final volume of 500 μL. The stopped-flow procedures were the same as previously described [28].

#### 4.2.4 Global analysis of the effect of tofacitinib on MPO Inhibition

For the inhibitory effect of tofacitinib on MPO activity, a set of the time-dependent fluorescence progress curves was fit simultaneously by a slow-tight binding model using DynaFit 3 software ([111]; Biokine, Ltd. Watertown, MA, USA). Kinetic models of a two-step mechanism are shown as follows:



**Scheme I. The two-step model tested.**

The inhibitory efficiencies for the inhibitory effects of tofacitinib on MPO activity are obtained from DynaFit software. By using the examination of a two-step slow tight-binding inhibitor model, the overall inhibition constant ( $K_i^*$ ) was determined as given by the following equation:

$$K_i^* = \frac{[E][I]}{[EI]+[EI^*]} = K_i \left( \frac{k_{-4} + k_{+4}}{k_{-4}} \right) \quad (\text{Eq. 1}).$$

$k_{+3}$ ,  $k_{-3}$ ,  $k_{+4}$ ,  $k_{-4}$  were obtained by simulating a set of fluorescence progress curves inhibited by tofacitinib using DynaFit 3, where  $K_i = k_{-3} / k_{+3}$ . For reversibility kinetic study of MPO activity, sets of progress curves were fit with a single exponential function using GraphPad Prism 5.0.

#### 4.2.5 SDS-PAGE analysis of effects of tofacitinib on MPO cleavage by BAH

To determine the effect of tofacitinib on the heme catalytic ability of MPO, MPO (1.2  $\mu\text{M}$ ) was incubated at room temperature with BAH following addition of tofacitinib and  $\text{H}_2\text{O}_2$  (20  $\mu\text{M}$ ). These samples of 20  $\mu\text{L}$  were added to non-reducing sample loading buffer (Bio-rad), and loaded without prior heating onto a 4-15% gradient SDS-polyacrylamide gel electrophoresis (SDS-PAGE). Of note, heat treatment was avoided to prevent the autocatalytic cleavage of MPO heavy chain at  $^{\text{HC}}\text{Met}^{243}\text{-}^{\text{HC}}\text{Pro}^{244}$  bond that gives rise to 39 kDa and 20 kDa bands [112]. The movement of the heme b on the gel was monitored through topical application of Western Lightning reagent (PerkinElmer Inc.) after protein staining of elaborated gels. Total protein staining was done with Gelcode Blue reagent (Pierce) and imaged with Bio-Rad Gel Doc imager using Quantity One version 4.6.9. A Fujifilm LAS-1000 luminescence imager was used to collect the light production generated as a result of this chemiluminescence reaction.

#### 4.2.6 Spectral analysis of MPO

Spectral scans of MPO were performed on a UV-vis Evolution<sup>TM</sup> 300 spectrophotometer (Thermo Fisher Scientific Inc, MA, USA) using 1.2  $\mu\text{M}$  MPO in 100 mM acetate sodium buffer (pH 5.6) in the presence or absence of tofacitinib in a total volume of 1 mL.  $\text{H}_2\text{O}_2$  titrations were conducted with sequential 10  $\mu\text{L}$  additions to the 990  $\mu\text{L}$ . Absorbance readings were recorded every nanometer from 350 nm to 750 nm. The spectral scanning speed was 120 nm per min and

spectral scanning band was 1 nm with very high smooth. The spectra for each curve of reactions were obtained by subtracting out the spectrum for blank with acetate buffer.

#### **4.2.7 Inhibition of MPO activity by tofacitinib using luminescence assay**

To evaluate the inhibitory effect of tofacitinib on MPO activity, a luminescence assay was developed with luminol as the peroxidase substrate. In reactions of 200  $\mu$ L total volume, MPO (9 nM) was incubated with the luminol substrate (400  $\mu$ M) in MEBSS buffer for a series of tofacitinib concentrations for 5 mins before triggering the reaction by the addition of H<sub>2</sub>O<sub>2</sub> (20  $\mu$ M). Dispensing of H<sub>2</sub>O<sub>2</sub> was performed using the auto-injection function controlled by the SkanIt software version 2.4.3 built within the Varioskan plate reader. Measurements were taken at 1 s intervals over 2 mins. The apparent IC<sub>50</sub> values for tofacitinib were determined based on the percentage of inhibition of MPO activity using Prism software (GraphPad Software, Inc., CA, USA). The luminescence intensity imaged from the 96-wells plate was performed using a Fujifilm LAS-1000 luminescence imager.

### **4.3 Results**

#### **4.3.1 Inhibition of MPO by tofacitinib**

Recent studies found that an oral JAK inhibitor tofacitinib was effective for the treatment of rheumatoid arthritis [155, 156]. It was reported that thioxanthines were mechanism-based inhibitors of MPO [19]. The structural comparison between this potent inhibitor and tofacitinib gives a clue on inhibition of MPO by tofacitinib shown in Figure 4.1A. Our study found that MPO activity was also inhibited by tofacitinib. We also found that JAK inhibitor tofacitinib can be docked in the active site pocket of MPO using the docking software Sybyl-X 1.3 as shown in Figure 4.1C. The hydrogen and ligand trifluoromethyl-substituted aromatic hydroxymate (HX1) were removed from MPO in complex with the reversible inhibitor HX1 (PDB accession number

4C1M) prior to docking tofacitinib into the active site pocket of MPO. To further determine the inhibitory potency of tofacitinib on MPO, the MPO peroxidase activity was measured by the oxidation of ADHP to produce resorufin fluorescent product using fluorescence plate reader. Reactions of 1.12 nM MPO were incubated with 25  $\mu$ M ADHP and 5  $\mu$ M H<sub>2</sub>O<sub>2</sub> in the presence of titrated concentration of tofacitinib prior to performing the fluorescence intensity endpoint reading. As shown in Figure 4.1B,  $K_d$  ( $434.08 \pm 38.31 \mu$ M) of tofacitinib on MPO in acetate buffer (pH=5.6) was calculated after fitting the data in Scientist software.

#### **4.3.2 Global analysis of tofacitinib on oxidation of the ADHP by the MPO-H<sub>2</sub>O<sub>2</sub> system by use of DynaFit modeling software**

To verify the potency of MPO inhibition by tofacitinib, stopped flow rapid kinetic study was performed to monitor the MPO activity in the presence of different concentration of tofacitinib. We further explored whether the mechanism of MPO inhibition by tofacitinib was via one-step slow binding or two-step slow binding mechanism. Initially, we analyzed sets of tofacitinib-dependent inhibition of MPO peroxidase activity under the constant concentration of ADHP substrate and compiled these progress curves in the DynaFit software. MPO (23 nM) was preincubated with 40  $\mu$ M ADHP in the absence or in the presence of increasing concentration of tofacitinib and then initiated with 20  $\mu$ M H<sub>2</sub>O<sub>2</sub> using stopped-flow spectrofluorometer. Under the simplified MPO-H<sub>2</sub>O<sub>2</sub> system, simultaneous modeling of the progress curves with initial Michaelis-Menten parameters determined previously, provided us with examination of a two-step model of MPO inhibition by tofacitinib. We also obtained the inhibitory efficiencies measured by DynaFit modeling for the inhibition of MPO by tofacitinib as shown in Table 4.1. The results of tofacitinib for the two-step model of slow binding inhibition is shown in Figure 4.2A. The value of  $Ki^*$  (298  $\mu$ M) was determined by calculating from inhibitory efficiencies

using the equation. The representative residual plots from DynaFit modeling are shown in the bottom panel.

#### **4.3.3 Rapid kinetic dialysis studies confirm that MPO inhibition by tofacitinib is reversible**

To further determine the reversibility of MPO inhibition by tofacitinib, MPO activity was monitored through the oxidation of ADHP by the use of MPO rapid stopped-flow assay. MPO (23 nM) was preincubated with 40  $\mu$ M ADHP in the absence or in the presence of 2 mM tofacitinib and then initiated with 20  $\mu$ M  $H_2O_2$  using stopped-flow spectrofluorometer. As shown in Figure 4.2B, the fluorescence intensity of the reaction was increased within 20 seconds and then reaches equilibrium (curve a). The MPO activity was decreased in the reaction with tofacitinib (curve c). The dialysis result showed that MPO activity was restored after overnight dialysis of the reaction of MPO with the same concentration of tofacitinib as curve c (curve b of Figure 4.2B). There was no increase in MPO activity for inhibition of MPO by ABAH as previously reported using the same method [28]. The representative residual plots from Graphpad Prism 5 are shown in the bottom panel. These results indicate that tofacitinib reversibly inhibits MPO activity.

#### **4.3.4 Tofacitinib prevents the destruction of the MPO heme in the presence of high concentration of $H_2O_2$**

MPO is a dimer (146 kDa) linked through a central disulfide bond. Each MPO monomer consists of a glycosylated light chain (14.5 kDa) and a heavy chain (58.5 kDa) linked through the heme. It has been previously demonstrated that the MPO heme can be degraded to release iron in the presence of high concentration of  $H_2O_2$  when it was added to MPO at more than 1000:1 ratio and incubated for 2 h [117]. The light chain of MPO can be released from the heavy chain after the heme is broken. Reactions of MPO (1.2  $\mu$ M) with tofacitinib (2.5 mM, lane 3) in the

presence of increasing concentration of H<sub>2</sub>O<sub>2</sub>, namely 8 μM (lane 3), 40 μM (lane 4), 80 μM (lane 5), 160 μM (lane 6), 800 μM (lane 7) and 8 mM (lane 8) for 10 min (Figure 4.3A and 4.3B) were compared to similar reactions without tofacitinib (Figure 4.1C and 4.1D). As shown in Figure 4.3A, there was no light chain produced in the reactions of MPO with high concentration of H<sub>2</sub>O<sub>2</sub> (160 μM, 800 μM in lane 6 and lane 7, respectively) and the produced LC was decreased in the reaction of MPO incubated with tofacitinib in the presence of 8 mM H<sub>2</sub>O<sub>2</sub> (lane 8 in Figure 4.3A) compared to the similar reaction without tofacitinib (lane 8 in Figure 4.3C). We also found there was apparent luminescence on the protein band from the reaction of MPO incubated with tofacitinib in the presence of 800 μM H<sub>2</sub>O<sub>2</sub> (lane 7 in Figure 4.3B), which did not happen in the similar reaction without tofacitinib (lane 7 in Figure 4.3D). These results indicate that tofacitinib prevented the destruction of MPO heme by high concentration of H<sub>2</sub>O<sub>2</sub>, which probably is due to competition of MPO active site between tofacitinib and H<sub>2</sub>O<sub>2</sub>.

#### **4.3.5 Tofacitinib competes with the active site of MPO with BAH**

We previously found BAH cleaved the light chain of MPO out of the heavy chain in the presence of H<sub>2</sub>O<sub>2</sub> [28]. Here, the cleavage of MPO by BAH was used as an indicator for the binding of tofacitinib with the MPO active site. Reactions of MPO (1.2 μM) with H<sub>2</sub>O<sub>2</sub> (20 μM, lane 3) in the presence of increasing concentration of tofacitinib, namely 0.5 mM (lane 4), 1 mM (lane 5), 2 mM (lane 6), 4 mM (lane 7), 8 mM (lane 8) for 10 min (The left panel in Figure 4.4A and 4.4B) were compared to similar reactions added with BAH (The middle panel in Figure 4.4A and 4.4B). As shown in the left panel in Figure 4.4A and 4.4B, there was no produced light chain of MPO in the reaction of MPO with various concentration of tofacitinib. BAH cleaved the light chain with heme out of the heavy chain of MPO as shown in the third lane of the middle panel of Figure 4.4A and 4.4B, which is consistent with our previous results [28]. Increased concentration

of tofacitinib prevented the cleavage of MPO by BAH as shown in the middle panel (lane 4 to lane 8). To further confirm these results, similar reactions with increased concentration of BAH (5 mM) were found to enhance the cleavage effect of BAH on MPO as shown in the right panel (Figure 4.4A and 4.4B). These results demonstrated that tofacitinib prevented the cleavage of MPO by BAH, which further indicates that tofacitinib competes with the active site of MPO with BAH.

#### **4.3.6 Spectroscopic analysis of the effect of tofacitinib on the MPO heme signature**

Spectral changes of MPO for the formation of reactive heme intermediates have been primarily used to investigate the mechanistic interactions of MPO with potential ligands. To analyze the effect of tofacitinib on MPO Soret peak, we performed the spectroscopic scanning of reactions of MPO, BAH and tofacitinib in the presence of  $H_2O_2$ . As shown in Figure 4.5A, curves represent MPO (black line), MPO with hydrazide (dotted), MPO with hydrazide post  $H_2O_2$  addition after 10 min (dashed) and again after 1hr (dot-dashed). In the presence of BAH, the spectral shifts of MPO heme group from 430 to 413 nm occurred. As shown in Figure 4.5B, curves represent MPO (black line), MPO with tofacitinib (dotted), MPO with tofacitinib post  $H_2O_2$  addition after 10 min (dashed) and again after addition of BAH (dot-dashed) for 10 min. The pre-incubation of MPO with tofacitinib interfered that the spectral shifts occurred in the reaction of MPO with BAH in the presence of  $H_2O_2$ . This study demonstrated that tofacitinib could prevent the spectral shifts of MPO heme group from 430 to 413 caused by BAH interference. This indicates tofacitinib can interrupt or block the accessibility of BAH to the active site on MPO.

#### **4.3.7 Inhibition of MPO luminescence production by tofacitinib**

Luminol was previously used to monitor the MPO activity in both inflammation model



and cancer model [67]. We also established a biochemical luminescence assay to characterize the MPO peroxidase activity *in vitro* [48]. To evaluate the inhibitory effect of tofacitinib on peroxidase activity of MPO, this assay was performed with luminol as the peroxidase substrate. The inhibitory rate constant for the reaction was not determined due to the inherent difficulty of relating these observed luminescence progress curves to molar product formed. Instead apparent  $IC_{50}$  values for tofacitinib were determined based on the percentage of inhibition of MPO peroxidase activity. Apparent  $IC_{50}$  of tofacitinib (28  $\mu$ M) on MPO was calculated based on the percentage of inhibition of MPO peroxidase activity (Figure 4.6A). The plot of endpoint readings of luminescence for reactions of MPO versus increasing concentrations of tofacitinib was shown in Fig. 4.6B. The apparent  $IC_{50}$  was obtained by fit the data. The luminescence intensities for MPO reactions with tofacitinib (the reaction condition is the same as the reaction in Figure 4.6B) were decreased as the concentration of tofacitinib increased as shown in Figure 4.6C.

#### **4.3.8 Bioluminescence imaging of MPO activity in Matrigel implant *in vivo***

Bioluminescent reaction of MPO with luminol depends on the concentration of  $H_2O_2$ . Therefore, we optimized the concentration of  $H_2O_2$  in MPO reaction to improve the imaging protocol of MPO activity in mice. 180 nM MPO with 400 mM  $H_2O_2$  (site 1), 180 nM MPO with 2 mM  $H_2O_2$  (site 2), 180 nM MPO with 4 mM  $H_2O_2$  (site 3), 180 nM MPO with 40 mM  $H_2O_2$  (site 4) in the presence of 100 mM luminol in Matrigel were implanted on the back of mice. The time course bioluminescence imaging of MPO activity was taken from 5 min to 16 min at 1-min interval as shown in Supplementary Figure 2. The luminescence yield was more stable when we used 40 mM  $H_2O_2$  in the reaction as shown in Figure 7A. With this optimized reaction condition for *in vivo* imaging of MPO activity, we embedded the mixture of MPO, 100 mM luminol and Matrigel (site 1), the mixture of 180 nM MPO, 1mM tofacitinib, 100 mM luminol and Matrigel

(site 2), the mixture of 180 nM MPO, 40 mM H<sub>2</sub>O<sub>2</sub>, 100 mM luminol and Matrigel (site 3), the mixture of 180 nM MPO, 40 mM H<sub>2</sub>O<sub>2</sub>, 100 mM luminol, 1 mM tofacitinib and Matrigel (site 4) on the backs of mice. The bioluminescence imaging of MPO activity was taken from 5 min to 16 min at 1-min interval as shown in Supplementary Figure 3. In the presence of tofacitinib, the MPO-mediated luminescence is decreased significantly in the reaction compared to the same reaction without tofacitinib (site 4 versus site 3) as shown in Figure 7B. Therefore, We further demonstrated that tofacitinib inhibited MPO activity in mice implanted with Matrigel.

#### 4.4 Discussion

The compelling evidence that MPO mediated oxidation to amplify oxidative stress at inflammation sites has focused attention on it as a pharmacological candidate of RA and other inflammatory diseases. Previously, it was reported that tofacitinib, an oral JAK inhibitor, was effective in the treatment of moderate to severe RA and then became a FDA-approved drug for RA. Here, we assigned the additional function of tofacitinib to be a weak inhibitor of MPO for the treatment of RA. Tofacitinib may also be a promising lead for the treatment of other inflammatory diseases by targeting MPO.

Based on the structural similarity between thioxanthines and tofacitinib, it is plausible to speculate the possibility of inhibition of MPO by tofacitinib. The docking results provide us with more evidence of interaction between the active site pocket and tofacitinib (Figure 4.1C). The further biochemical assay determined the  $K_d$  value of tofacitinib on MPO inhibition (Figure 4.1B). The stopped-flow fluorescence kinetic study revealed that tofacitinib acted as a reversible inhibitor because there was restored activity of MPO in the reaction of MPO with tofacitinib after overnight dialysis (Figure 4.2). Thioxanthines is a potent mechanism-based inhibitor of MPO. The inhibition mechanisms disparity of MPO between tofacitinib and thioxanthines

probably are due to the difference of structural comparison. The crystal structural results showed there were interactions between MPO and thioxanthines. The MPO inhibitor 2-thioxanthine is a covalent inhibitor of MPO, whereby the heme methyl group of MPO covalently forms the bond with the exocyclic sulfur of 2-TX. Tofacitinib does not have exocyclic sulfur to form covalent bond with MPO but can still be easily docked in the active site pocket of MPO.

The previous findings showed that MPO was converted into the Compound III that is an inactive form of MPO by high concentration of  $H_2O_2$ . We found tofacitinib interfered with the inactivation of MPO by high concentration of  $H_2O_2$  (Figure 4.3). Initially, we speculated that tofacitinib could be oxidized by  $H_2O_2$ , which may decrease the concentration of  $H_2O_2$  or delete  $H_2O_2$ . However, LC-MS study found there was no oxidized product in the reaction of MPO with tofacitinib in the presence of high concentration of  $H_2O_2$  (Supplementary Figure 4.1). Therefore, it is plausible that tofacitinib may serve by diverting the conversion of MPO intermediate to prevent the formation of Compound I and Compound II. We also reported that BAH cleaved the LC with heme out of MPO heavy chain by breaking the ester bonds. The cleavage of MPO by BAH was used as an indicator to study the inhibition of MPO by tofacitinib. The presence of tofacitinib in the reaction of MPO and BAH leads to the attenuation of dose-dependent cleavage effect of BAH on MPO and increased concentration of BAH results in more LC and luminescence signal from the LC with heme based on the results of protein staining experiment and in-gel luminescence imaging (Figure 4.4). These results are also consistent with the results from spectral scanning analysis of MPO reactions with tofacitinib and BAH as shown in Figure 4.5 (430-413 nm). It is possible that tofacitinib competes with the accessibility of the active site pocket of MPO with BAH.

*In vitro* MPO luminescence assay was used to further confirm the inhibition of MPO by

tofacitinib. This assay is cost-effective and more sensitive since the recent study showed that luminol was used to monitor MPO activity *in vivo* [67] and the bioluminescent substrate luminol analog L-012 was used to measure MPO activity in human plasma samples combined with designated MPO activity on a polymer surface (MAPS) [160]. We determined the apparent  $IC_{50}$  of tofacitinib on MPO inhibition using this rapid luminescence assay (Figure 4.6). We attempted to explore the reason for the difference between  $K_d$  value and the apparent  $IC_{50}$  of tofacitinib. Phosphate buffer with different pH values were used to analyze the relationship between pH and the potency of tofacitinib inhibition on MPO. We found the maximal fluorescence intensity was increased as the pH value of reaction buffer was increased from 5 to 8, but the potency of MPO inhibitor tofacitinib is not completely dependent on the pH value of reaction buffer (Table 4.2). The further *in vivo* imaging of MPO inhibition by tofacitinib in implant Matrigel showed that tofacitinib inhibited MPO activity *in vivo* using bioluminescence imaging (Figure 4.7 and Supplementary Figure 4.2 & 4.3).

**Table 4.1 Inhibitory efficiencies of tofacitinib on MPO activity.**

As measured in the MPO fluorescence stopped flow assay and simultaneous fit with a 2-step slow tight-binding mechanism using DynaFit 3. Fixed constants  $k_{+1}=10 \mu\text{M}^{-1}\text{s}^{-1}$ ,  $k_{-1}=80 \text{ s}^{-1}$ ,  $k_{+2}=224 \text{ s}^{-1}$ .

<b>Inhibitor</b>	<b><math>k_{+3}</math></b>	<b><math>k_{-3}</math></b>	<b><math>k_{+4}</math></b>	<b><math>k_{-4}</math></b>	<b><math>K_i</math></b>	<b><math>K_i^*</math></b>
<b>Tofacitinib</b>	<b><math>0.001 \pm 0.1\text{E-}06</math></b>	<b><math>0.014 \pm 0.002</math></b>	<b><math>53.8 \pm 5</math></b>	<b><math>2.5 \pm 0.24</math></b>	<b>13.25</b>	<b>298.94</b>

**Table 4.2 Effect of pH on the  $K_d$  value of tofacitinib for the MPO fluorescence reaction.**

<b>pH of Phosphate Buffer</b>	<b>5.7</b>	<b>6</b>	<b>6.5</b>	<b>7</b>	<b>8</b>
<b>Maximum of FI</b>	<b>3373</b>	<b>4910</b>	<b>8640</b>	<b>11800</b>	<b>12250</b>
<b><math>K_d</math> (<math>\mu\text{M}</math>)</b>	<b>252</b>	<b>329</b>	<b>386</b>	<b>328</b>	<b>55</b>

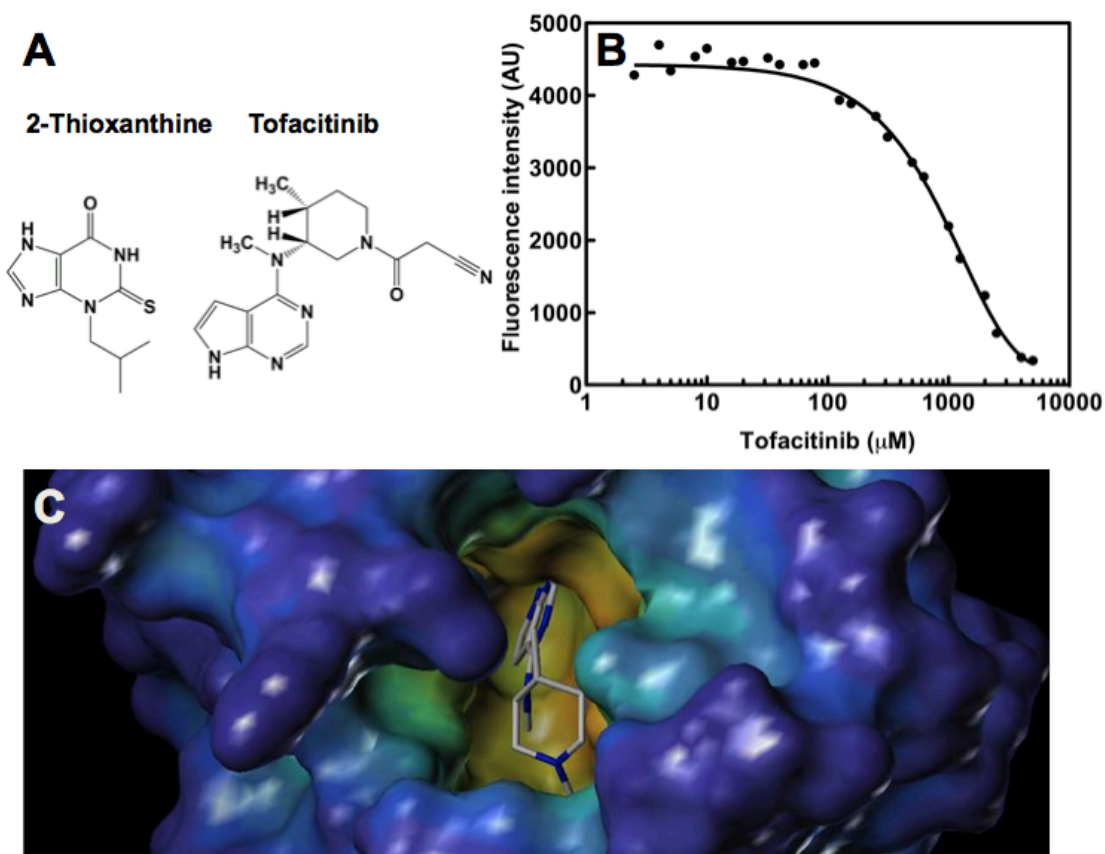


**Figure 4.1 Inhibition of MPO by tofacitinib.**

A, Structural comparison of tofacitinib and thioxanthines. B, Reactions of 20  $\mu\text{M}$  ADHP were incubated with MPO (1.12 nM) in assay buffer in the absence or presence of varied final concentration of tofacitinib (1.6  $\mu\text{M}$ , 3.125  $\mu\text{M}$ , 6.25  $\mu\text{M}$ , 12.5  $\mu\text{M}$ , 25  $\mu\text{M}$ , 50  $\mu\text{M}$ , 100  $\mu\text{M}$ ). The reaction was incubated for 5 min after initiating the reaction via addition of 5  $\mu\text{M}$   $\text{H}_2\text{O}_2$ . The fluorescence intensity endpoint reading was performed.  $K_d$  of tofacitinib on MPO was calculated based on the percentage of inhibition of MPO activity. C, Tofacitinib was docked in the pocket of MPO active site as surface representation of the MPO protein using SYBYL-X 1.3 software (hydrogens are not included in surface).

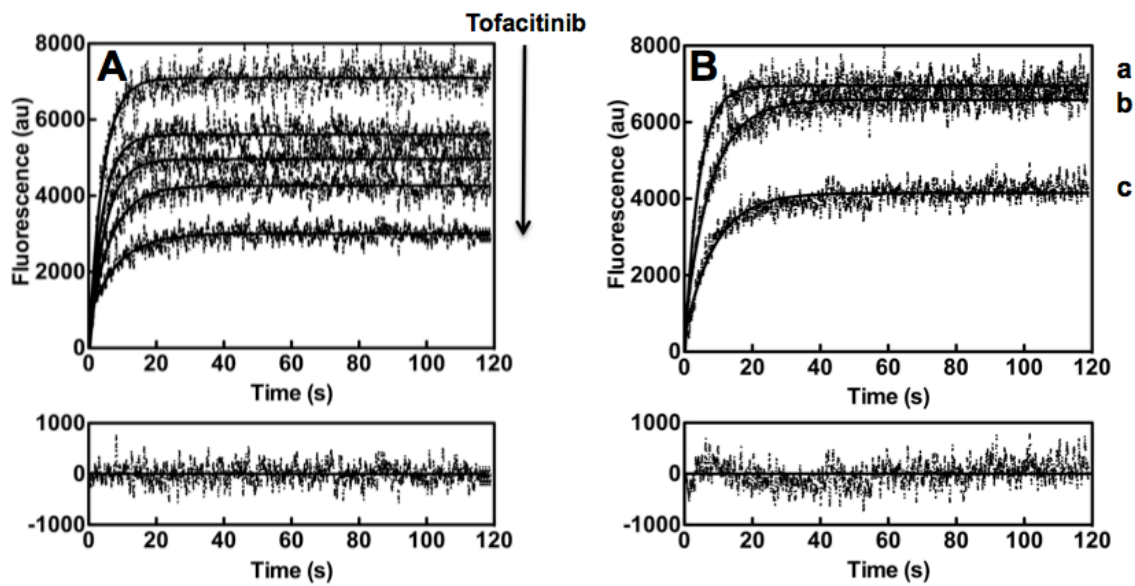


**Figure 4.2 Kinetic study of MPO inhibition by tofacitinib.**

A, Progress curves of relative fluorescence units (RFU) for reactions of MPO (23 nM) with various concentration of tofacitinib (0, 0.5 mM, 1 mM, 2 mM, 4 mM) were globally fit to binding models. Representative goodness-of-fit for the reaction of MPO with 4 mM tofacitinib is shown as a residual plot. B, Reversibility study of tofacitinib on MPO inhibition was shown. Stopped flow analysis of MPO (23 nM) and in the absence of or in the presence of 2 mM tofacitinib (curve a and curve c) were mixed and incubated in assay buffer for 1 hr prior to triggering  $\text{H}_2\text{O}_2$  addition. The overnight exhaustive dialysis of identical mixtures into assay buffer followed addition with  $\text{H}_2\text{O}_2$  was shown as curve b. Representative goodness-of-fit for the reaction of MPO with tofacitinib after overnight dialysis is shown as a residual plot. Titrations were performed as described in greater detail under “Experimental Procedures.”



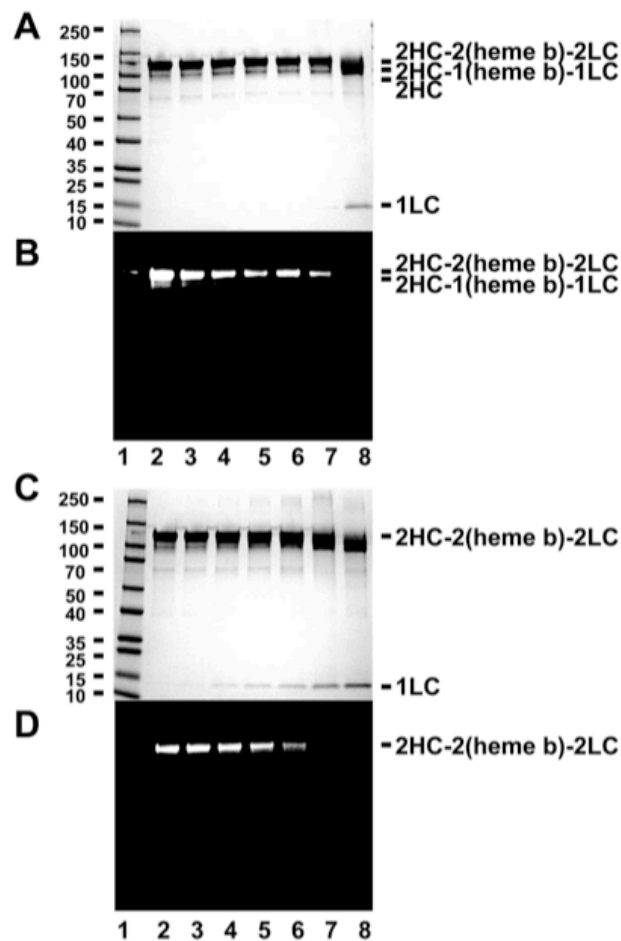


**Figure 4.3 Effect of tofacitinib on MPO compared to the heme destruction generated by high dose H<sub>2</sub>O<sub>2</sub> treatment.**

A-B, the protein-stained gel images (A) and in-gel luminescence images (B) were shown for the reactions of MPO (1.2 μM) with tofacitinib (2.5 mM, lane 2) in the presence of increasing concentrations of H<sub>2</sub>O<sub>2</sub>, namely 8 μM (lane 3), 40 μM (lane 4), 80 μM (lane 5), 160 μM (lane 6), 800 μM (lane 7) and 8 mM (lane 8) for 10 min (Figure 4.3A and Figure 4.3B). C-D, Similar reactions were set up without tofacitinib for 10 min prior to loading the sample. Experiments conducted as described under “Experimental Procedures.”

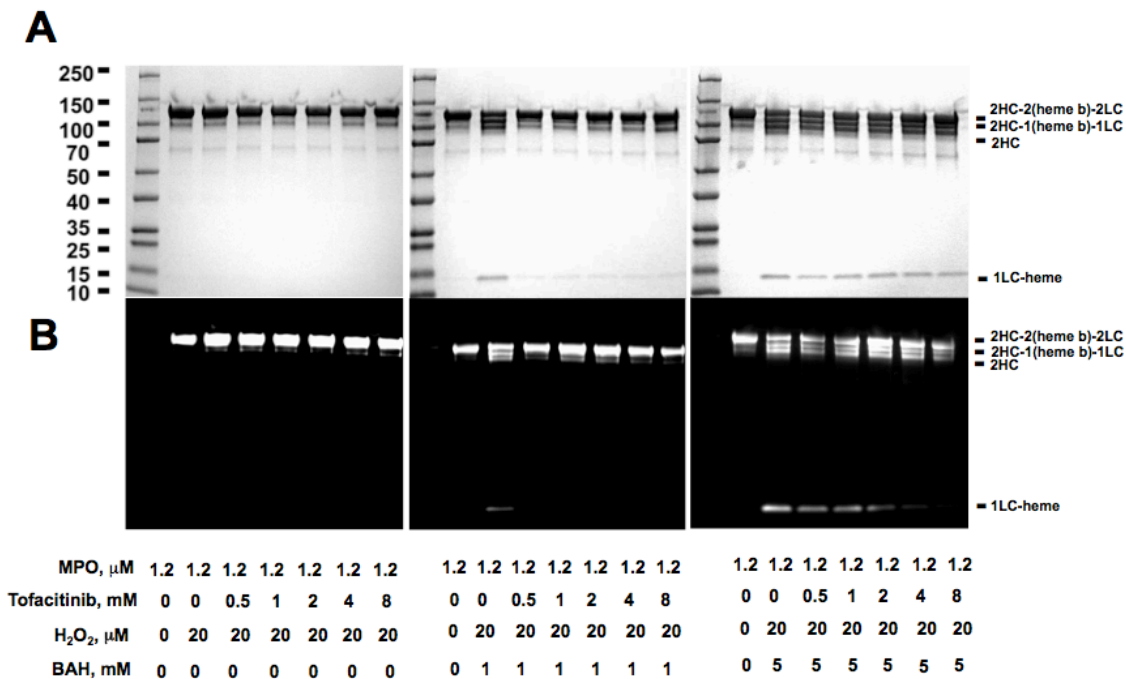


**Figure 4.4 Tofacitinib prevents the cleavage of MPO by BAH in the presence of H<sub>2</sub>O<sub>2</sub>.**

A-B, the protein-stained gel images (A) and in-gel luminescence images (B) were shown for the reactions of MPO (1.2  $\mu\text{M}$ ) with 20  $\mu\text{M}$  H<sub>2</sub>O<sub>2</sub> in the presence of increased concentrations of tofacitinib, namely 0 mM (lane 3), 0.5 mM (lane 4), 1 mM (lane 5), 2 mM (lane 6), 4mM (lane 7), and 8 mM (lane 8) for 10 min (Figure 4.1A and Figure 4.1B). The middle panel shown in A and B were similar reactions set up with addition of BAH (1 mM) for 10 min prior to loading the sample. The right panel shown in A and B were similar reactions set up with addition of BAH (5 mM) for 10 min prior to loading the sample. Experiments conducted as described under “Experimental Procedures.”

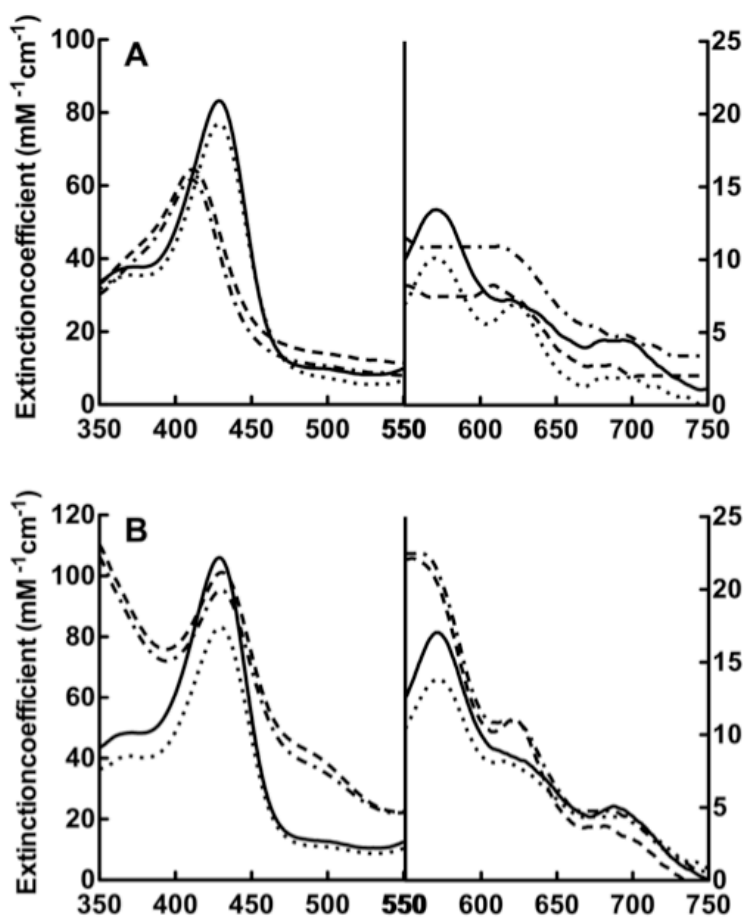


**Figure 4.5 The interference of tofacitinib on MPO cleavage by BAH using spectroscopic analysis of MPO heme signature.**

A, Curves represent 1.2 μM MPO (black line), MPO with 1 mM BAH (dotted), MPO with 1mM BAH post 40 μM H<sub>2</sub>O<sub>2</sub> addition after 10 min (dashed) and again after 1hr (dot-dashed). B, Curves represent MPO (black line), MPO with 2 mM tofacitinib (dotted), MPO with tofacitinib post 40 μM H<sub>2</sub>O<sub>2</sub> addition after 10 min (dashed) and 1 mM BAH added in the reaction of MPO with tofacitinib in the presence of H<sub>2</sub>O<sub>2</sub> after 10 mins (dot-dashed).

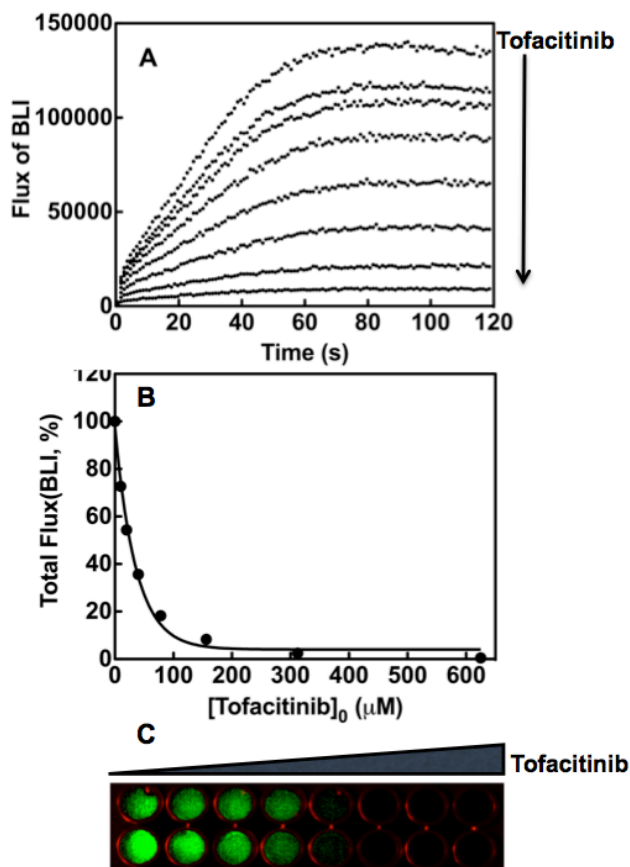


**Figure 4.6 Inhibition of MPO by tofacitinib using luminescence assay.**

A, Reactions of luminol (400  $\mu\text{M}$ ) were incubated with 9 nM MPO in MEBSS buffer in the absence or presence of varied final concentration of tofacitinib (1.6  $\mu\text{M}$ , 3.125  $\mu\text{M}$ , 15.6  $\mu\text{M}$ , 31.25  $\mu\text{M}$ , 62.5  $\mu\text{M}$ , 125  $\mu\text{M}$ , 250  $\mu\text{M}$ ). The auto-injector function of the Varioskan plate reader were used to initiate the reaction via addition of 20  $\mu\text{M}$   $\text{H}_2\text{O}_2$ . B, The endpoint reading of luminescence for reactions of MPO with various concentration of tofacitinib (9.87  $\mu\text{M}$ , 18.75  $\mu\text{M}$ , 37.5  $\mu\text{M}$ , 75  $\mu\text{M}$ , 150  $\mu\text{M}$ , 300  $\mu\text{M}$ , 600  $\mu\text{M}$ ) was performed using luminescence assay in plate reader. The luminescence imaging of wells containing the samples in 96-wells plate were shown. Apparent  $\text{IC}_{50}$  of tofacitinib on MPO was calculated based on the percentage of inhibition of MPO activity. Titrations were performed as described in greater detail under “Experimental Procedures.”

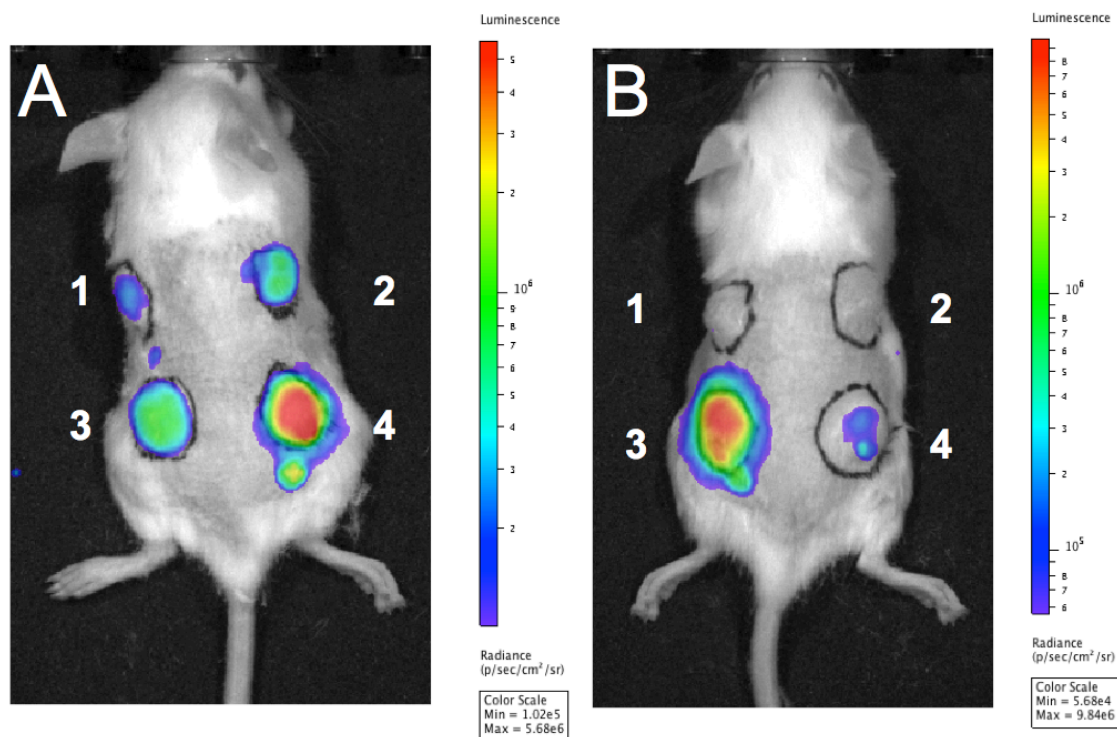
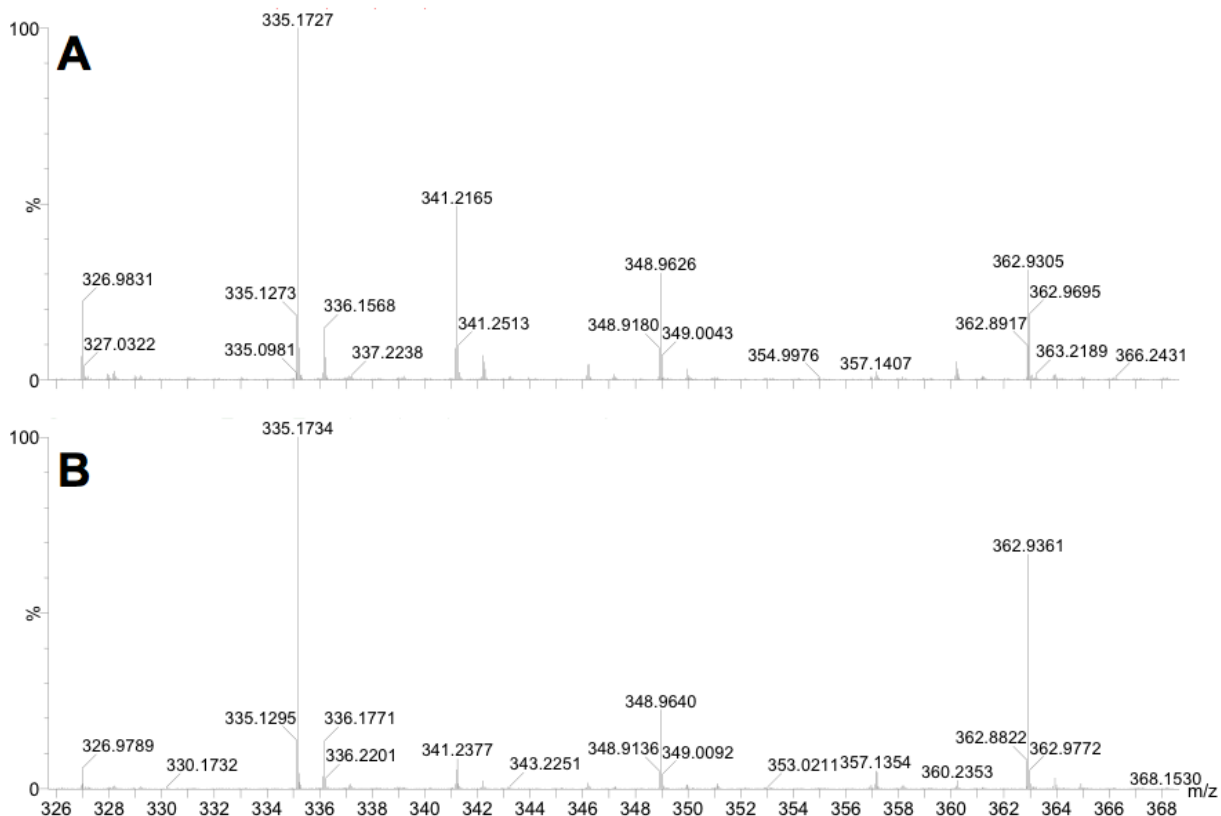


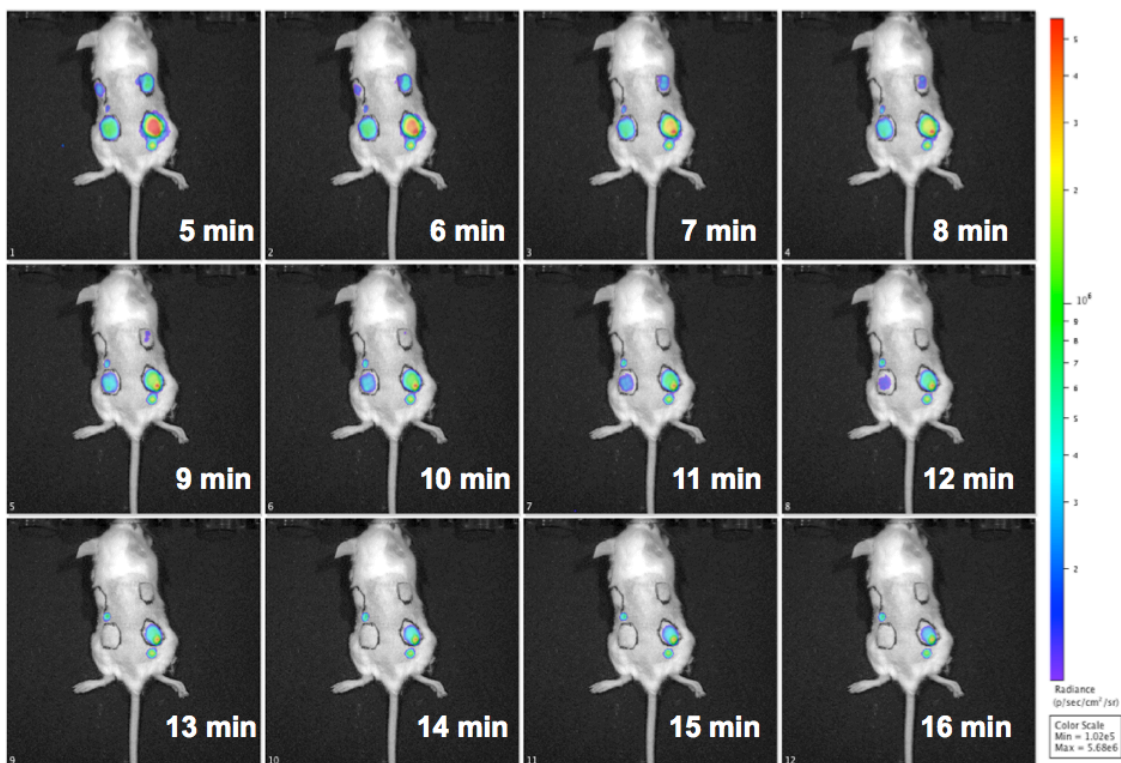
**Figure 4.7 Luminol-BLI of MPO implants *in vivo*.**

A, 180 nM MPO with 400  $\mu\text{M}$   $\text{H}_2\text{O}_2$  in the presence of 100  $\mu\text{M}$  luminol (site 1), 180 nM MPO with 2 mM  $\text{H}_2\text{O}_2$  in the presence of 100  $\mu\text{M}$  luminol (site 2), 180 nM MPO with 4 mM  $\text{H}_2\text{O}_2$  in the presence of 100  $\mu\text{M}$  luminol (site 3), 180 nM MPO with 40 mM  $\text{H}_2\text{O}_2$  in the presence of 100  $\mu\text{M}$  luminol (site 4) were added in Matrigel prior to implanting the samples into the back of the mice. Shown is a bioluminescence imaging of MPO activity taken at 5 min. B, the mixture of 180 nM MPO and 100  $\mu\text{M}$  luminol in Matrigel (site 1), the mixture of 180 nM MPO, 100  $\mu\text{M}$  luminol and 1mM tofacitinib in Matrigel (site 2), the mixture of 180 nM MPO, 100  $\mu\text{M}$  luminol and 40 mM  $\text{H}_2\text{O}_2$  in Matrigel (site 3), and the mixture of 180 nM MPO, 100  $\mu\text{M}$  luminol, 40 mM  $\text{H}_2\text{O}_2$  in the presence of 1 mM tofacitinib in Matrigel (site 4) were implanted into the back of the mice (n=3). Shown is a bioluminescence imaging of MPO activity taken at 5 min. Experiments were conducted as described under “Experimental Procedures.”



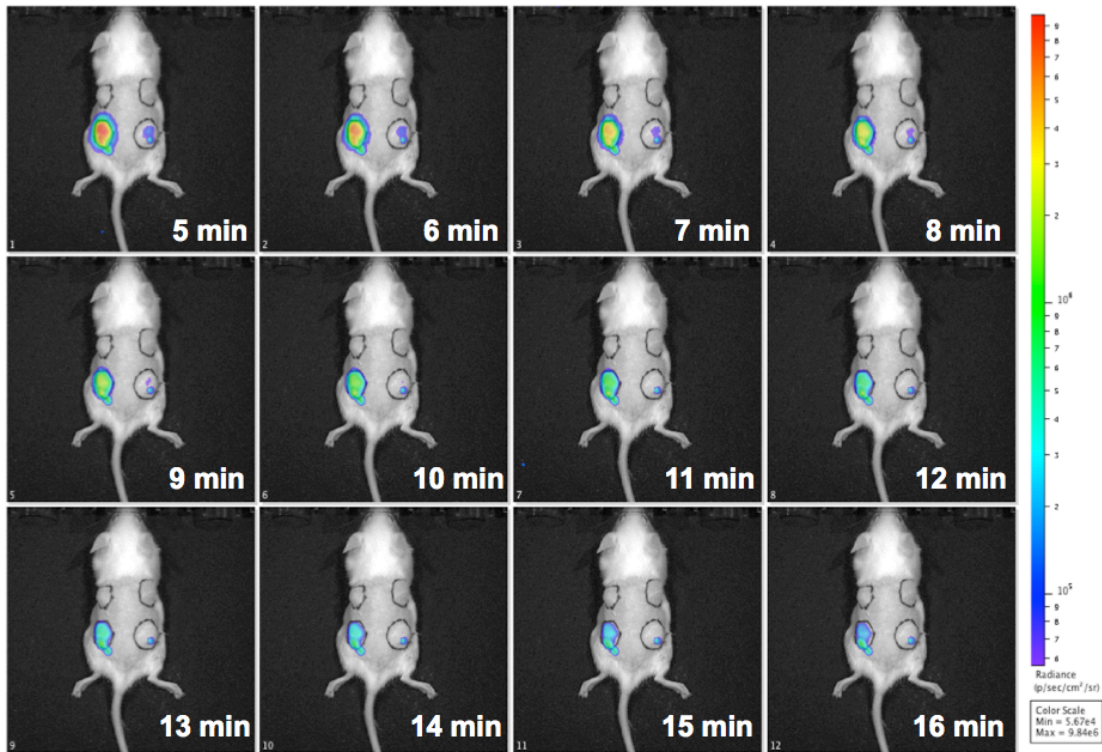
**Supplementary Figure 4.1 Comparison analysis of MPO reaction with tofacitinib in the presence or absence of H<sub>2</sub>O<sub>2</sub> using LC-MS method.**

A, The sample of 1.2 μM MPO with 2 mM tofacitinib in the acetate buffer was injected in LC-MS. B, LC-MS was performed after reactions of 1.2 μM MPO were incubated with 2 mM tofacitinib in the presence of 400 μM H<sub>2</sub>O<sub>2</sub> in the acetate buffer for 1 h.



**Supplementary Figure 4.2 Optimization of H<sub>2</sub>O<sub>2</sub> concentration for imaging of MPO activity in implant Matrigel.**

180 nM MPO with 400  $\mu$ M H<sub>2</sub>O<sub>2</sub> (site 1), 180 nM MPO with 2 mM H<sub>2</sub>O<sub>2</sub> (site 2), 180 nM MPO with 4 mM H<sub>2</sub>O<sub>2</sub> (site 3), 180 nM MPO with 40 mM H<sub>2</sub>O<sub>2</sub> (site 4) in the presence of 100  $\mu$ M luminol in Matrigel were implanted on the back of the mice. Five minutes later, the mice were imaged using the IVIS Lumina XRMS Imager (PerkinElmer, Waltham, MA). The bioluminescence imaging of MPO activity was taken from 5 min to 16 min at 1-min interval.



**Supplementary Figure 4.3 Time course BLI imaging of MPO implants *in vivo*.**

To study inhibition of MPO by tofacitinib in implant Matrigel, 180 nM MPO with 100  $\mu$ M luminol in Matrigel (site 1), 180 nM MPO and 1mM tofacitinib in the presence of 100  $\mu$ M luminol in Matrigel (site 2), 180 nM MPO with 40 mM H<sub>2</sub>O<sub>2</sub> in the presence of 100  $\mu$ M luminol in Matrigel (site 3), and 180 nM MPO with 40 mM H<sub>2</sub>O<sub>2</sub> in the presence of 100  $\mu$ M luminol and 1 mM tofacitinib in Matrigel (site 4) were implanted into the back of the mice. Five minutes later, the mice were imaged using the IVIS Lumina XRMS Imager (PerkinElmer, Waltham, MA) with a binning of four and default aperture settings. The bioluminescence imaging of MPO activity was taken from 5 min to 16 min at 1-min interval.



## Conclusions

MPO, a heme-containing enzyme secreted from myeloid cells, is critical for killing the bacteria in innate immune response. It is also involved in the formation of MPO-derived oxidants in chronic inflammation in diseases such as atherosclerosis, COPD, and RA. The compelling evidence that MPO contributes to oxidative stress during inflammation has focused attention on it as a pharmacological target of these chronic inflammatory diseases. Currently, there are several small molecule inhibitors that have been identified as potential therapeutic approach for inflammatory diseases.

MPO peroxidase activity can be inhibited by small molecules certain reactive nitrogen containing compounds such as salicylhydroxamic acid [103], sodium azide [161], isoniazid (isonicotinylhydrazine) [104], 4-ABAH [162], melatonin (N-acetyl-5-methoxytryptamine) [105], tempol (4-hydroxy-2,2,6,6-tetra-methyl-1-piperidinyloxy [106, 163]. There also is sulfur containing MPO inhibitors that have also been identified, such as dapsone (diamino-diphenyl sulfone) [164], and propylthiouracil [165]. In addition, PF-1355 was also demonstrated to ameliorate immune complex vasculitis and anti-glomerular basement membrane glomerulonephritis in mice [166]. INV315 was shown to inhibit superoxide production, reduce atherosclerotic plaque, and improve the endothelial function in a mouse atherosclerosis model [167].

Recently, thioxanthines were found to be mechanism-based inactivators of MPO by covalently attaching to the heme [19]. It is proposed that thioxanthines can be oxidized and then the initially produced free radicals react with the heme of the enzyme and covalently attach to the heme prosthetic group of the enzyme. In preclinical study, thioxanthine-2, MPO irreversible inhibitor can stop progression of experimental COPD [11]. Follow up study synthesized alkyne analogue of 2-thioxanthine, in combination with click chemistry-activity based protein profiling, providing a novel method to enrich and identify proteins that are labeled by mechanism-based inhibitors [91]. This clickable activity-based protein probe might be suitable for evaluating MPO activity in pharmacological studies and proteomics [91].

MPO anti-neutrophil cytoplasmic antibody (MPO-ANCA) mainly targets the carboxy-terminus of the MPO heavy chain [168]. Another endogenous inhibitor of MPO is ceruloplasmin, a known MPO binding partner and copper containing protein [20]. N-acetyl lysyltyrosylcysteine amide (KYC) was reported to be one of the effective inhibitors of MPO activity [169]. It not only can dampen the MPO derived oxidants during inflammation, but also decrease MPO-mediated HOCl formation and oxidation of LDL *in vitro* [169]. It was demonstrated that KYC could react with both Compounds I and Compound II by binding to the active site pocket of MPO using ultraviolet-visible spectral studies [169]. Docking studies further indicated that the tyrosine of KYC inhibitor were just above the active site heme of MPO [169]. This tripeptide KYC inhibitor can be applied for treatment of MPO-mediated vascular diseases [170], which provides the evidence of MPO peptide inhibitors as a possible approach for treatment of inflammatory diseases and guides the development of next generation of MPO inhibitors.

In this study, we developed a rapid fluorescence assay to measure MPO activity using its fluorescent substrate ADHP. We characterized a number of known MPO inhibitors, such as 4-ABAH, isoniazid and  $\text{NaN}_3$  before expanding to isomers of 4-ABAH and BAH analogs using stopped-flow fluorescence assay. We showed that MPO inhibition by 4-ABAH and its isomer 2-ABAH required at least two steps, whereas MPO inhibition by  $\text{NaN}_3$  and isoniazid followed one-step mechanism using Dynafit3 software. In-gel luminescence analysis and spectral analysis of the reaction of MPO with BAH in the presence of  $\text{H}_2\text{O}_2$  revealed that MPO inhibition by BAH was presumably caused by hydrolysis of the ester bond between the heme pyrrole A ring and MPO heavy chain Glu<sup>242</sup> residue, which further results in releasing the complex of heme b and LC fragment from the MPO HC.

In addition, to gain insight into the constraints imposed by the MPO active site and channel leading to the buried protoporphyrin IX ring, the structure and function relationship behind this ester bond cleavage was studied for a panel of BAH analogs. We found the cleavage efficiency of BAH analogs were greatest when the Hammett constant is close to neutral. Furthermore, a fluorescence analog of BAH Cy5-hydrazide was used to track the cleavage of MPO, we showed the evidence that Cy5-hydrazide labeled the MPO HC by cleavage mechanism, which can be further applied to *in vivo* imaging of MPO activity in mice model.

We also demonstrated that an oral JAK inhibitor tofacitinib was a MPO reversible inhibitor and was docked into the active site moiety of MPO. MPO fluorescence endpoint assay and stopped-flow rapid kinetic analysis determined  $K_d$  and  $K_i$  values of tofacitinib on MPO inhibition. SDS-PAGE and in-gel luminescence imaging analysis of tofacitinib/BAH-treated

MPO revealed that tofacitinib prevented the cleavage of MPO by BAH in the presence of H<sub>2</sub>O<sub>2</sub>, which indicates that it may compete for the active site of MPO with BAH. Spectral analysis of reactions of MPO with tofacitinib/BAH demonstrated that tofacitinib could prevent the Soret peak blue shift of MPO caused by BAH in the presence of H<sub>2</sub>O<sub>2</sub>. The assignment of new function of JAK inhibitor tofacitinib to be a MPO inhibitor provides the insights into the drug development for chronic inflammatory diseases, such as rheumatoid arthritis, atherosclerosis and so on. It might be more effective for treatment of RA if we can identify an inhibitor that inhibits both JAK1/3 and MPO because some of cytokines that contribute to the pathogenesis of RA are JAK independent. This study provides proof of concepts for identification of inhibitors targeting JAK1/3 and MPO to treat RA.

## References

1. Auffray, C., et al., *Monitoring of blood vessels and tissues by a population of monocytes with patrolling behavior*. Science, 2007. **317**(5838): p. 666-70.
2. Theoharides, T.C., et al., *Mast cells and inflammation*. Biochim Biophys Acta, 2012. **1822**(1): p. 21-33.
3. Palucka, K. and J. Banchereau, *Cancer immunotherapy via dendritic cells*. Nat Rev Cancer, 2012. **12**(4): p. 265-77.
4. Theilgaard-Monch, K., B.T. Porse, and N. Borregaard, *Systems biology of neutrophil differentiation and immune response*. Curr Opin Immunol, 2006. **18**(1): p. 54-60.
5. Diacovo, T.G., et al., *Neutrophil rolling, arrest, and transmigration across activated, surface-adherent platelets via sequential action of P-selectin and the beta 2-integrin CD11b/CD18*. Blood, 1996. **88**(1): p. 146-57.
6. Brinkmann, V., et al., *Neutrophil extracellular traps kill bacteria*. Science, 2004. **303**(5663): p. 1532-5.
7. Branzk, N., et al., *Neutrophils sense microbe size and selectively release neutrophil extracellular traps in response to large pathogens*. Nat Immunol, 2014. **15**(11): p. 1017-25.
8. Parker, H., et al., *Myeloperoxidase associated with neutrophil extracellular traps is active and mediates bacterial killing in the presence of hydrogen peroxide*. J Leukoc Biol, 2012. **91**(3): p. 369-76.

9. Nathan, C., *Neutrophils and immunity: challenges and opportunities*. Nat Rev Immunol, 2006. **6**(3): p. 173-82.
10. Klebanoff, S.J., *Myeloperoxidase: friend and foe*. J Leukoc Biol, 2005. **77**(5): p. 598-625.
11. Churg, A., et al., *Late intervention with a myeloperoxidase inhibitor stops progression of experimental chronic obstructive pulmonary disease*. Am J Respir Crit Care Med, 2012. **185**(1): p. 34-43.
12. Stamp, L.K., et al., *Myeloperoxidase and oxidative stress in rheumatoid arthritis*. Rheumatology (Oxford), 2012. **51**(10): p. 1796-803.
13. Heinecke, J.W., *Oxidative stress: new approaches to diagnosis and prognosis in atherosclerosis*. Am J Cardiol, 2003. **91**(3A): p. 12A-16A.
14. Nicholls, S.J. and S.L. Hazen, *Myeloperoxidase and cardiovascular disease*. Arterioscler Thromb Vasc Biol, 2005. **25**(6): p. 1102-11.
15. Nicholls, S.J. and S.L. Hazen, *Myeloperoxidase, modified lipoproteins, and atherogenesis*. J Lipid Res, 2009. **50** Suppl: p. S346-51.
16. Ambrosone, C.B., et al., *Myeloperoxidase genotypes and enhanced efficacy of chemotherapy for early-stage breast cancer in SWOG-8897*. J Clin Oncol, 2009. **27**(30): p. 4973-9.
17. Ramsey, M.R. and N.E. Sharpless, *ROS as a tumour suppressor?* Nat Cell Biol, 2006. **8**(11): p. 1213-5.
18. Fiedler, T.J., C.A. Davey, and R.E. Fenna, *X-ray crystal structure and characterization of halide-binding sites of human myeloperoxidase at 1.8 Å resolution*. J Biol Chem, 2000. **275**(16): p. 11964-71.

19. Tiden, A.K., et al., *2-thioxanthines are mechanism-based inactivators of myeloperoxidase that block oxidative stress during inflammation*. J Biol Chem, 2011. **286**(43): p. 37578-89.
20. Chapman, A.L., et al., *Ceruloplasmin is an endogenous inhibitor of myeloperoxidase*. J Biol Chem, 2013. **288**(9): p. 6465-77.
21. Carpena, X., et al., *Essential role of proximal histidine-asparagine interaction in mammalian peroxidases*. J Biol Chem, 2009. **284**(38): p. 25929-37.
22. Blair-Johnson, M., T. Fiedler, and R. Fenna, *Human myeloperoxidase: structure of a cyanide complex and its interaction with bromide and thiocyanate substrates at 1.9 Å resolution*. Biochemistry, 2001. **40**(46): p. 13990-7.
23. Fenna, R., J. Zeng, and C. Davey, *Structure of the green heme in myeloperoxidase*. Arch Biochem Biophys, 1995. **316**(1): p. 653-6.
24. Forbes, L.V., et al., *Potent Reversible Inhibition of Myeloperoxidase by Aromatic Hydroxamates*. J Biol Chem, 2013.
25. Furtmuller, P.G., et al., *Active site structure and catalytic mechanisms of human peroxidases*. Arch Biochem Biophys, 2006. **445**(2): p. 199-213.
26. Kooter, I.M., et al., *Site-directed mutagenesis of Met243, a residue of myeloperoxidase involved in binding of the prosthetic group*. Journal of Biological Inorganic Chemistry, 1997. **2**(2): p. 191-197.
27. Wever, R. and H. Plat, *Spectral properties of myeloperoxidase and its ligand complexes*. Biochim Biophys Acta, 1981. **661**(2): p. 235-9.

28. Huang, J., F. Smith, and P. Panizzi, *Ordered cleavage of myeloperoxidase ester bonds releases active site heme leading to inactivation of myeloperoxidase by benzoic acid hydrazide analogs*. Arch Biochem Biophys, 2014. **548**: p. 74-85.
29. Huang, L., G. Wojciechowski, and P.R.O. de Montellano, *Role of Heme-Protein Covalent Bonds in Mammalian Peroxidases: PROTECTION OF THE HEME BY A SINGLE ENGINEERED HEME-PROTEIN LINK IN HORSERADISH PEROXIDASE*. Journal of Biological Chemistry, 2006. **281**(28): p. 18983-18988.
30. Nordberg, J. and E.S. Arner, *Reactive oxygen species, antioxidants, and the mammalian thioredoxin system*. Free Radic Biol Med, 2001. **31**(11): p. 1287-312.
31. Bedard, K. and K.H. Krause, *The NOX family of ROS-generating NADPH oxidases: physiology and pathophysiology*. Physiol Rev, 2007. **87**(1): p. 245-313.
32. Hampton, M.B., A.J. Kettle, and C.C. Winterbourn, *Inside the neutrophil phagosome: oxidants, myeloperoxidase, and bacterial killing*. Blood, 1998. **92**(9): p. 3007-17.
33. Cai, H., et al., *Detection of reactive oxygen species and nitric oxide in vascular cells and tissues: comparison of sensitivity and specificity*. Methods Mol Med, 2007. **139**: p. 293-311.
34. Dikalov, S., M. Skatchkov, and E. Bassenge, *Spin trapping of superoxide radicals and peroxynitrite by 1-hydroxy-3-carboxy-pyrrolidine and 1-hydroxy-2,2,6,6-tetramethyl-4-oxo-piperidine and the stability of corresponding nitroxyl radicals towards biological reductants*. Biochem Biophys Res Commun, 1997. **231**(3): p. 701-4.
35. Britigan, B.E. and D.R. Hamill, *The interaction of 5,5-dimethyl-1-pyrroline-N-oxide with human myeloperoxidase and its potential impact on spin trapping of neutrophil-derived free radicals*. Arch Biochem Biophys, 1989. **275**(1): p. 72-81.



36. Dikalov, S.I., et al., *EPR Detection of Cellular and Mitochondrial Superoxide Using Cyclic Hydroxylamines*. Free radical research, 2011. **45**(4): p. 417-430.
37. Ichimori, K., C.M. Arroyo, and H. Nakazawa, *Electron spin resonance for spin trapping of 3,5-dibromo-4-nitrosobenzene sulfonate*. Methods Enzymol, 1996. **268**: p. 203-11.
38. Hempel, S.L., et al., *Dihydrofluorescein diacetate is superior for detecting intracellular oxidants: comparison with 2',7'-dichlorodihydrofluorescein diacetate, 5(and 6)-carboxy-2',7'-dichlorodihydrofluorescein diacetate, and dihydrorhodamine 123*. Free Radic Biol Med, 1999. **27**(1-2): p. 146-59.
39. Bass, D.A., et al., *Flow cytometric studies of oxidative product formation by neutrophils: a graded response to membrane stimulation*. J Immunol, 1983. **130**(4): p. 1910-7.
40. Wang, X., et al., *Imaging ROS signaling in cells and animals*. J Mol Med (Berl), 2013. **91**(8): p. 917-27.
41. Kojima, H., et al., *Detection and imaging of nitric oxide with novel fluorescent indicators: diaminofluoresceins*. Anal Chem, 1998. **70**(13): p. 2446-53.
42. Chan, J., S.C. Dodani, and C.J. Chang, *Reaction-based small-molecule fluorescent probes for chemoselective bioimaging*. Nat Chem, 2012. **4**(12): p. 973-84.
43. Robinson, K.M., et al., *Selective fluorescent imaging of superoxide in vivo using ethidium-based probes*. Proc Natl Acad Sci U S A, 2006. **103**(41): p. 15038-43.
44. Setsukinai, K., et al., *Development of novel fluorescence probes that can reliably detect reactive oxygen species and distinguish specific species*. J Biol Chem, 2003. **278**(5): p. 3170-5.

45. Flemmig, J., et al., *The fluorescein-derived dye aminophenyl fluorescein is a suitable tool to detect hypobromous acid (HOBr)-producing activity in eosinophils*. J Biol Chem, 2012. **287**(33): p. 27913-23.
46. Peng, T. and D. Yang, *HKGreen-3: a rhodol-based fluorescent probe for peroxynitrite*. Org Lett, 2010. **12**(21): p. 4932-5.
47. Sun, Z.N., et al., *A highly specific BODIPY-based fluorescent probe for the detection of hypochlorous acid*. Org Lett, 2008. **10**(11): p. 2171-4.
48. Huang, J., et al., *Inactivation of myeloperoxidase by benzoic acid hydrazide*. Arch Biochem Biophys, 2015. **570**: p. 14-22.
49. Pulli, B., et al., *Measuring myeloperoxidase activity in biological samples*. PLoS One, 2013. **8**(7): p. e67976.
50. Renshaw, S.A., et al., *A transgenic zebrafish model of neutrophilic inflammation*. Blood, 2006. **108**(13): p. 3976-8.
51. Niethammer, P., et al., *A tissue-scale gradient of hydrogen peroxide mediates rapid wound detection in zebrafish*. Nature, 2009. **459**(7249): p. 996-9.
52. Colucci-Guyon, E., et al., *Strategies of professional phagocytes in vivo: unlike macrophages, neutrophils engulf only surface-associated microbes*. J Cell Sci, 2011. **124**(Pt 18): p. 3053-9.
53. Fang, L., et al., *In vivo visualization and attenuation of oxidized lipid accumulation in hypercholesterolemic zebrafish*. J Clin Invest, 2011. **121**(12): p. 4861-9.
54. Crowhurst, M.O., J.E. Layton, and G.J. Lieschke, *Developmental biology of zebrafish myeloid cells*. Int J Dev Biol, 2002. **46**(4): p. 483-92.

55. Kaplow, L.S., *Simplified Myeloperoxidase Stain Using Benzidine Dihydrochloride*. Blood, 1965. **26**: p. 215-9.
56. Mathias, J.R., et al., *Resolution of inflammation by retrograde chemotaxis of neutrophils in transgenic zebrafish*. J Leukoc Biol, 2006. **80**(6): p. 1281-8.
57. Gray, C., et al., *Simultaneous intravital imaging of macrophage and neutrophil behaviour during inflammation using a novel transgenic zebrafish*. Thromb Haemost, 2011. **105**(5): p. 811-9.
58. Petrie, T.A., et al., *Macrophages modulate adult zebrafish tail fin regeneration*. Development, 2014. **141**(13): p. 2581-91.
59. Henry, K.M., et al., *Zebrafish as a model for the study of neutrophil biology*. J Leukoc Biol, 2013. **94**(4): p. 633-42.
60. Robertson, A.L., et al., *A zebrafish compound screen reveals modulation of neutrophil reverse migration as an anti-inflammatory mechanism*. Sci Transl Med, 2014. **6**(225): p. 225ra29.
61. Yang, L.L., et al., *Endotoxin molecule lipopolysaccharide-induced zebrafish inflammation model: a novel screening method for anti-inflammatory drugs*. Molecules, 2014. **19**(2): p. 2390-409.
62. Doyle, A.D., et al., *Expression of the secondary granule proteins major basic protein 1 (MBP-1) and eosinophil peroxidase (EPX) is required for eosinophilopoiesis in mice*. Blood, 2013. **122**(5): p. 781-90.
63. Odobasic, D., et al., *Endogenous myeloperoxidase is a mediator of joint inflammation and damage in experimental arthritis*. Arthritis Rheumatol, 2014. **66**(4): p. 907-17.

64. Maeda, H., *The enhanced permeability and retention (EPR) effect in tumor vasculature: the key role of tumor-selective macromolecular drug targeting*. Adv Enzyme Regul, 2001. **41**: p. 189-207.
65. Chen, J.W., et al., *Imaging of myeloperoxidase in mice by using novel amplifiable paramagnetic substrates*. Radiology, 2006. **240**(2): p. 473-81.
66. Panizzi, P., et al., *Oxazine conjugated nanoparticle detects in vivo hypochlorous acid and peroxynitrite generation*. J Am Chem Soc, 2009. **131**(43): p. 15739-44.
67. Gross, S., et al., *Bioluminescence imaging of myeloperoxidase activity in vivo*. Nat Med, 2009. **15**(4): p. 455-61.
68. Zhang, N., et al., *Enhanced detection of myeloperoxidase activity in deep tissues through luminescent excitation of near-infrared nanoparticles*. Nat Med, 2013. **19**(4): p. 500-5.
69. Stamatas, G.N., M. Southall, and N. Kollias, *In vivo monitoring of cutaneous edema using spectral imaging in the visible and near infrared*. J Invest Dermatol, 2006. **126**(8): p. 1753-60.
70. Sanders, J.M., et al., *Metabolism and disposition of luminol in the rat*. Xenobiotica, 2000. **30**(3): p. 263-72.
71. Eggleston, H. and P. Panizzi, *Molecular Imaging of Bacterial Infections in vivo: The Discrimination between Infection and Inflammation*. Informatics, 2014. **1**: p. 72-99.
72. Nahrendorf, M., et al., *Activatable magnetic resonance imaging agent reports myeloperoxidase activity in healing infarcts and noninvasively detects the antiinflammatory effects of atorvastatin on ischemia-reperfusion injury*. Circulation, 2008. **117**(9): p. 1153-60.

73. Magalotti, S., et al., *Evaluation of inflammatory response to acute ischemia using near-infrared fluorescent reactive oxygen sensors*. Mol Imaging Biol, 2013. **15**(4): p. 423-30.
74. Pu, K., et al., *Semiconducting polymer nanoparticles as photoacoustic molecular imaging probes in living mice*. Nat Nanotechnol, 2014. **9**(3): p. 233-9.
75. Chen, J.W., et al., *Human myeloperoxidase: a potential target for molecular MR imaging in atherosclerosis*. Magn Reson Med, 2004. **52**(5): p. 1021-8.
76. Rodriguez, E., et al., *Activatable magnetic resonance imaging agents for myeloperoxidase sensing: mechanism of activation, stability, and toxicity*. J Am Chem Soc, 2010. **132**(1): p. 168-77.
77. Pulli, B., et al., *Multiple Sclerosis: Myeloperoxidase Immunoradiology Improves Detection of Acute and Chronic Disease in Experimental Model*. Radiology, 2014: p. 141495.
78. Gounis, M.J., et al., *MR Imaging of Myeloperoxidase Activity in a Model of the Inflamed Aneurysm Wall*. AJNR Am J Neuroradiol, 2015. **36**(1): p. 146-52.
79. Kidd, D., Y. Liu, and B.F. Cravatt, *Profiling serine hydrolase activities in complex proteomes*. Biochemistry, 2001. **40**(13): p. 4005-15.
80. Fonovic, M. and M. Bogoy, *Activity based probes for proteases: applications to biomarker discovery, molecular imaging and drug screening*. Curr Pharm Des, 2007. **13**(3): p. 253-61.
81. Nakai, R., et al., *Ranking the selectivity of PubChem screening hits by activity-based protein profiling: MMP13 as a case study*. Bioorg Med Chem, 2009. **17**(3): p. 1101-8.
82. Patricelli, M.P., et al., *Functional interrogation of the kinome using nucleotide acyl phosphates*. Biochemistry, 2007. **46**(2): p. 350-8.

83. Salisbury, C.M. and B.F. Cravatt, *Activity-based probes for proteomic profiling of histone deacetylase complexes*. Proc Natl Acad Sci U S A, 2007. **104**(4): p. 1171-6.
84. Salisbury, C.M. and B.F. Cravatt, *Optimization of activity-based probes for proteomic profiling of histone deacetylase complexes*. J Am Chem Soc, 2008. **130**(7): p. 2184-94.
85. Adam, G.C., E.J. Sorensen, and B.F. Cravatt, *Proteomic profiling of mechanistically distinct enzyme classes using a common chemotype*. Nat Biotechnol, 2002. **20**(8): p. 805-9.
86. Niphakis, M.J. and B.F. Cravatt, *Enzyme inhibitor discovery by activity-based protein profiling*. Annu Rev Biochem, 2014. **83**: p. 341-77.
87. Cravatt, B.F., A.T. Wright, and J.W. Kozarich, *Activity-based protein profiling: from enzyme chemistry to proteomic chemistry*. Annu Rev Biochem, 2008. **77**: p. 383-414.
88. Jessani, N., et al., *Enzyme activity profiles of the secreted and membrane proteome that depict cancer cell invasiveness*. Proc Natl Acad Sci U S A, 2002. **99**(16): p. 10335-40.
89. Chiang, K.P., et al., *An enzyme that regulates ether lipid signaling pathways in cancer annotated by multidimensional profiling*. Chem Biol, 2006. **13**(10): p. 1041-50.
90. Chang, J.W., D.K. Nomura, and B.F. Cravatt, *A potent and selective inhibitor of KIAA1363/AADACL1 that impairs prostate cancer pathogenesis*. Chem Biol, 2011. **18**(4): p. 476-84.
91. Ward, J., et al., *Mechanistic characterization of a 2-thioxanthine myeloperoxidase inhibitor and selectivity assessment utilizing click chemistry--activity-based protein profiling*. Biochemistry, 2013. **52**(51): p. 9187-201.
92. Andrews, P.C. and N.I. Krinsky, *Quantitative determination of myeloperoxidase using tetramethylbenzidine as substrate*. Anal Biochem, 1982. **127**(2): p. 346-50.

93. Andrews, P.C. and N.I. Krinsky, *A kinetic analysis of the interaction of human myeloperoxidase with hydrogen peroxide, chloride ions, and protons*. J Biol Chem, 1982. **257**(22): p. 13240-5.
94. Harrison, J.E., et al., *Compound I of myeloperoxidase*. Biochem Biophys Res Commun, 1980. **94**(1): p. 34-40.
95. Everse, J., *The structure of heme proteins Compounds I and II: some misconceptions*. Free Radic Biol Med, 1998. **24**(7-8): p. 1338-46.
96. Kettle, A.J., C.A. Gedye, and C.C. Winterbourn, *Mechanism of inactivation of myeloperoxidase by 4-aminobenzoic acid hydrazide*. Biochem J, 1997. **321 ( Pt 2)**: p. 503-8.
97. Fliss, H., *Oxidation of proteins in rat heart and lungs by polymorphonuclear leukocyte oxidants*. Mol Cell Biochem, 1988. **84**(2): p. 177-88.
98. Kooter, I.M., et al., *The Met243 sulfonium ion linkage is responsible for the anomalous magnetic circular dichroism and optical spectral properties of myeloperoxidase*. J Biol Inorg Chem, 1999. **4**(6): p. 684-91.
99. Kooter, I.M., et al., *Characterization of the Asp94 and Glu242 mutants in myeloperoxidase, the residues linking the heme group via ester bonds*. Eur J Biochem, 1999. **264**(1): p. 211-7.
100. Andrews, P.C. and N.I. Krinsky, *The reductive cleavage of myeloperoxidase in half, producing enzymically active hemi-myeloperoxidase*. J Biol Chem, 1981. **256**(9): p. 4211-8.

101. Vissers, M.C. and C.C. Winterbourn, *Myeloperoxidase-dependent oxidative inactivation of neutrophil neutral proteinases and microbicidal enzymes*. *Biochem J*, 1987. **245**(1): p. 277-80.
102. Hampton, M.B., A.J. Kettle, and C.C. Winterbourn, *Involvement of superoxide and myeloperoxidase in oxygen-dependent killing of Staphylococcus aureus by neutrophils*. *Infect Immun*, 1996. **64**(9): p. 3512-7.
103. Ikeda-Saito, M., et al., *Salicylhydroxamic acid inhibits myeloperoxidase activity*. *J Biol Chem*, 1991. **266**(6): p. 3611-6.
104. Forbes, L.V., et al., *Isoniazid as a substrate and inhibitor of myeloperoxidase: identification of amine adducts and the influence of superoxide dismutase on their formation*. *Biochem Pharmacol*, 2012. **84**(7): p. 949-60.
105. Galijasevic, S., I. Abdulhamid, and H.M. Abu-Soud, *Melatonin is a potent inhibitor for myeloperoxidase*. *Biochemistry*, 2008. **47**(8): p. 2668-77.
106. Vaz, S.M. and O. Augusto, *Inhibition of myeloperoxidase-mediated protein nitration by tempol: Kinetics, mechanism, and implications*. *Proc Natl Acad Sci U S A*, 2008. **105**(24): p. 8191-6.
107. Bozeman, P.M., D.B. Learn, and E.L. Thomas, *Inhibition of the human leukocyte enzymes myeloperoxidase and eosinophil peroxidase by dapsone*. *Biochem Pharmacol*, 1992. **44**(3): p. 553-63.
108. Malle, E., et al., *Myeloperoxidase: a target for new drug development?* *Br J Pharmacol*, 2007. **152**(6): p. 838-54.
109. Gorris, H.H. and D.R. Walt, *Mechanistic aspects of horseradish peroxidase elucidated through single-molecule studies*. *J Am Chem Soc*, 2009. **131**(17): p. 6277-82.



110. Nelson, D.P. and L.A. Kiesow, *Enthalpy of decomposition of hydrogen peroxide by catalase at 25 degrees C (with molar extinction coefficients of H<sub>2</sub>O<sub>2</sub> solutions in the UV)*. Anal Biochem, 1972. **49**(2): p. 474-8.
111. Kuzmic, P., *Program DYNAFIT for the analysis of enzyme kinetic data: application to HIV proteinase*. Anal Biochem, 1996. **237**(2): p. 260-73.
112. Taylor, K.L., J. Pohl, and J.M. Kinkade, Jr., *Unique autolytic cleavage of human myeloperoxidase. Implications for the involvement of active site MET409*. J Biol Chem, 1992. **267**(35): p. 25282-8.
113. Taylor, K.L., et al., *Isolation and identification of a protoheme IX derivative released during autolytic cleavage of human myeloperoxidase*. Arch Biochem Biophys, 1995. **316**(1): p. 635-42.
114. Swirski, F.K., et al., *Myeloperoxidase-rich Ly-6C<sup>+</sup> myeloid cells infiltrate allografts and contribute to an imaging signature of organ rejection in mice*. J Clin Invest, 2010. **120**(7): p. 2627-34.
115. Su, H.S., et al., *Vasculitis: molecular imaging by targeting the inflammatory enzyme myeloperoxidase*. Radiology, 2012. **262**(1): p. 181-90.
116. Cortez-Retamozo, V., et al., *Angiotensin II drives the production of tumor-promoting macrophages*. Immunity, 2013. **38**(2): p. 296-308.
117. Paumann-Page, M., et al., *Inactivation of human myeloperoxidase by hydrogen peroxide*. Arch Biochem Biophys, 2013. **539**(1): p. 51-62.
118. Marquez, L.A. and H.B. Dunford, *Kinetics of oxidation of tyrosine and dityrosine by myeloperoxidase compounds I and II - Implications for lipoprotein peroxidation studies*. The Journal of biological chemistry, 1995. **270**(51): p. 30434-30440.

119. Wagenmakers, E.J. and S. Farrell, *AIC model selection using Akaike weights*. *Psychon Bull Rev*, 2004. **11**(1): p. 192-6.
120. Burnham, K.P., Anderson, D. R., *Model selection and Multimodel inference: a practical information-theoretic approach, second edition*. 2002: Springer.
121. Winterbourn, C.C. and A.J. Kettle, *Reactions of superoxide with myeloperoxidase and its products*. *Jpn J Infect Dis*, 2004. **57**(5): p. S31-3.
122. Winterbourn, C.C., et al., *Modeling the reactions of superoxide and myeloperoxidase in the neutrophil phagosome: implications for microbial killing*. *J Biol Chem*, 2006. **281**(52): p. 39860-9.
123. Meng, Y., et al., *Enhanced sensitivity and precision in an enzyme-linked immunosorbent assay with fluorogenic substrates compared with commonly used chromogenic substrates*. *Anal Biochem*, 2005. **345**(2): p. 227-36.
124. Wilks, A., et al., *Expression and characterization of truncated human heme oxygenase (hHO-1) and a fusion protein of hHO-1 with human cytochrome P450 reductase*. *Biochemistry*, 1995. **34**(13): p. 4421-7.
125. Sharma, S., et al., *Lactoperoxidase: structural insights into the function, ligand binding and inhibition*. *Int J Biochem Mol Biol*, 2013. **4**(3): p. 108-128.
126. Ator, M.A., S.K. David, and P.R. Ortiz de Montellano, *Structure and catalytic mechanism of horseradish peroxidase. Regiospecific meso alkylation of the prosthetic heme group by alkylhydrazines*. *J Biol Chem*, 1987. **262**(31): p. 14954-60.
127. Ator, M.A. and P.R. Ortiz de Montellano, *Protein control of prosthetic heme reactivity. Reaction of substrates with the heme edge of horseradish peroxidase*. *J Biol Chem*, 1987. **262**(4): p. 1542-51.

128. Arvadia, P., et al., *4-Aminobenzoic acid hydrazide inhibition of microperoxidase-11: catalytic inhibition by reactive metabolites*. Arch Biochem Biophys, 2011. **515**(1-2): p. 120-6.
129. Smith, M.B., March, J, *March Advanced Organic Chemistry: Reaction, Mechanisms, and Structure, Sixth edition*. 2006: John Wiley & Sons, Inc. 395-416.
130. Lange, M. and D. Mansuy, *N-Substituted Porphyrins Formation from Carbene Iron-Porphyrin Complexes - a Possible Pathway for Cytochrome-P450 Heme Destruction*. Tetrahedron Letters, 1981. **22**(27): p. 2561-2564.
131. Kettle, A.J., C.J. van Dalen, and C.C. Winterbourn, *Peroxynitrite and myeloperoxidase leave the same footprint in protein nitration*. Redox Rep, 1997. **3**(5-6): p. 257-8.
132. Wojciechowski, G., L. Huang, and P.R. Ortiz de Montellano, *Autocatalytic Modification of the Prosthetic Heme of Horseradish but Not Lactoperoxidase by Thiocyanate Oxidation Products. A Role for Heme-Protein Covalent Cross-Linking*. Journal of the American Chemical Society, 2005. **127**(45): p. 15871-15879.
133. Colas, C., J.M. Kuo, and P.R. Ortiz de Montellano, *Asp-225 and glu-375 in autocatalytic attachment of the prosthetic heme group of lactoperoxidase*. J Biol Chem, 2002. **277**(9): p. 7191-200.
134. Poulos, T.L., et al., *Crystallographic refinement of lignin peroxidase at 2 Å*. J Biol Chem, 1993. **268**(6): p. 4429-40.
135. Yamada, Y., et al., *The 2.0 Å crystal structure of catalase-peroxidase from Haloarcula marismortui*. Nat Struct Biol, 2002. **9**(9): p. 691-5.

136. Baker, R.D., C.O. Cook, and D.C. Goodwin, *Catalase-peroxidase active site restructuring by a distant and "inactive" domain*. *Biochemistry*, 2006. **45**(23): p. 7113-21.
137. Patterson, W.R. and T.L. Poulos, *Crystal structure of recombinant pea cytosolic ascorbate peroxidase*. *Biochemistry*, 1995. **34**(13): p. 4331-41.
138. Colas, C. and P.R.O. de Montellano, *Horseradish Peroxidase Mutants That Autocatalytically Modify Their Prosthetic Heme Group: INSIGHTS INTO MAMMALIAN PEROXIDASE HEME-PROTEIN COVALENT BONDS*. *Journal of Biological Chemistry*, 2004. **279**(23): p. 24131-24140.
139. Colas, C. and P.R. Ortiz de Montellano, *Autocatalytic radical reactions in physiological prosthetic heme modification*. *Chem Rev*, 2003. **103**(6): p. 2305-32.
140. Forman, H.J., et al., *Even free radicals should follow some rules: A Guide to free radical research terminology and methodology*. *Free Radic Biol Med*, 2015. **78**: p. 233-5.
141. Beers, R.F., Jr. and I.W. Sizer, *A spectrophotometric method for measuring the breakdown of hydrogen peroxide by catalase*. *J Biol Chem*, 1952. **195**(1): p. 133-40.
142. Wisniewski, J.R., et al., *Universal sample preparation method for proteome analysis*. *Nat Methods*, 2009. **6**(5): p. 359-62.
143. McInnes, I.B. and F.Y. Liew, *Cytokine networks--towards new therapies for rheumatoid arthritis*. *Nat Clin Pract Rheumatol*, 2005. **1**(1): p. 31-9.
144. Allaire, S., et al., *Contemporary prevalence and incidence of work disability associated with rheumatoid arthritis in the US*. *Arthritis Rheum*, 2008. **59**(4): p. 474-80.
145. Lee, D.M. and M.E. Weinblatt, *Rheumatoid arthritis*. *Lancet*, 2001. **358**(9285): p. 903-11.

146. Smitten, A.L., et al., *A meta-analysis of the incidence of malignancy in adult patients with rheumatoid arthritis*. *Arthritis Res Ther*, 2008. **10**(2): p. R45.
147. Doran, M.F., et al., *Frequency of infection in patients with rheumatoid arthritis compared with controls: a population-based study*. *Arthritis Rheum*, 2002. **46**(9): p. 2287-93.
148. Naranjo, A., et al., *Cardiovascular disease in patients with rheumatoid arthritis: results from the QUEST-RA study*. *Arthritis Res Ther*, 2008. **10**(2): p. R30.
149. McInnes, I.B. and G. Schett, *Cytokines in the pathogenesis of rheumatoid arthritis*. *Nat Rev Immunol*, 2007. **7**(6): p. 429-42.
150. McInnes, I.B. and G. Schett, *The pathogenesis of rheumatoid arthritis*. *N Engl J Med*, 2011. **365**(23): p. 2205-19.
151. Smolen, J.S., D. Aletaha, and K. Redlich, *The pathogenesis of rheumatoid arthritis: new insights from old clinical data?* *Nat Rev Rheumatol*, 2012. **8**(4): p. 235-43.
152. O'Shea, J.J. and R. Plenge, *JAK and STAT signaling molecules in immunoregulation and immune-mediated disease*. *Immunity*, 2012. **36**(4): p. 542-50.
153. O'Sullivan, L.A., et al., *Cytokine receptor signaling through the Jak-Stat-Socs pathway in disease*. *Mol Immunol*, 2007. **44**(10): p. 2497-506.
154. Shuai, K. and B. Liu, *Regulation of JAK-STAT signalling in the immune system*. *Nat Rev Immunol*, 2003. **3**(11): p. 900-11.
155. Fleischmann, R., et al., *Placebo-controlled trial of tofacitinib monotherapy in rheumatoid arthritis*. *N Engl J Med*, 2012. **367**(6): p. 495-507.
156. Lee, E.B., et al., *Tofacitinib versus methotrexate in rheumatoid arthritis*. *N Engl J Med*, 2014. **370**(25): p. 2377-86.

157. Menter, A., et al., *Efficacy of tofacitinib, an oral janus kinase inhibitor, on clinical signs of moderate-to-severe plaque psoriasis in different body regions*. J Drugs Dermatol, 2014. **13**(3): p. 252-6.
158. Wang, W., et al., *Increased levels of serum myeloperoxidase in patients with active rheumatoid arthritis*. Life Sci, 2014. **117**(1): p. 19-23.
159. Fernandes, R.M., N.P. da Silva, and E.I. Sato, *Increased myeloperoxidase plasma levels in rheumatoid arthritis*. Rheumatol Int, 2012. **32**(6): p. 1605-9.
160. Goiffon, R.J., S.C. Martinez, and D. Piwnica-Worms, *A rapid bioluminescence assay for measuring myeloperoxidase activity in human plasma*. Nat Commun, 2015. **6**: p. 6271.
161. Nauseef, W.M., J.A. Metcalf, and R.K. Root, *Role of myeloperoxidase in the respiratory burst of human neutrophils*. Blood, 1983. **61**(3): p. 483-92.
162. Kettle, A.J., et al., *Inhibition of myeloperoxidase by benzoic acid hydrazides*. Biochem J, 1995. **308** ( Pt 2): p. 559-63.
163. Queiroz, R.F., S.M. Vaz, and O. Augusto, *Inhibition of the chlorinating activity of myeloperoxidase by tempol: revisiting the kinetics and mechanisms*. Biochem J, 2011. **439**(3): p. 423-31.
164. van Zyl, J.M., et al., *Mechanisms by which clofazimine and dapsone inhibit the myeloperoxidase system. A possible correlation with their anti-inflammatory properties*. Biochem Pharmacol, 1991. **42**(3): p. 599-608.
165. Zhang, A.H., et al., *Inhibition of oxidation activity of myeloperoxidase (MPO) by propylthiouracil (PTU) and anti-MPO antibodies from patients with PTU-induced vasculitis*. Clin Immunol, 2007. **122**(2): p. 187-93.

166. Zheng, W., et al., *PF-1355, a mechanism-based myeloperoxidase inhibitor, prevents immune complex vasculitis and anti-glomerular basement membrane glomerulonephritis.* J Pharmacol Exp Ther, 2015. **353**(2): p. 288-98.
167. Liu, C., et al., *Effects of a novel pharmacologic inhibitor of myeloperoxidase in a mouse atherosclerosis model.* PLoS One, 2012. **7**(12): p. e50767.
168. Erdbrugger, U., et al., *Mapping of myeloperoxidase epitopes recognized by MPO-ANCA using human-mouse MPO chimers.* Kidney Int, 2006. **69**(10): p. 1799-805.
169. Zhang, H., et al., *N-acetyl lysyltyrosylcysteine amide inhibits myeloperoxidase, a novel tripeptide inhibitor.* J Lipid Res, 2013. **54**(11): p. 3016-29.
170. Zhang, H., et al., *Inhibition of myeloperoxidase decreases vascular oxidative stress and increases vasodilatation in sickle cell disease mice.* J Lipid Res, 2013. **54**(11): p. 3009-15.